

Université du Québec  
Institut National de la Recherche Scientifique  
Centre Énergie Matériaux Télécommunications

## **INKJET-PRINTED FLEXIBLE RESISTIVE SWITCHING MEMORY**

Par  
Bernhard MITTERMEIER  
né HUBER

Thèse présentée pour l'obtention du grade de  
Philosophiae doctor (Ph.D.)  
en sciences de l'énergie et des matériaux

### **Jury d'évaluation**

Président du jury et examinateur interne	Professeur Shuhui SUN Institut National de la Recherche Scientifique Centre Énergie Matériaux Télécommunications
Examinateur externe	Professeur Matthew DAWBER Stony Brook University, USA Dept. of Physics and Astronomy
Examinateur externe	Professeur Alfred KERSCH Munich University of Applied Sciences Model and Simulation Lab
Co-directrice de recherche	Professeur Christina SCHINDLER Munich University of Applied Sciences Laboratory for Microsystems Technology
Directeur de recherche	Professeur Andreas RUEDIGER Institut National de la Recherche Scientifique Centre Énergie Matériaux Télécommunications



# Résumé

L'implémentation de l'"Internet des Objets" va nécessiter un nombre élevé de systèmes intégrés à faible coût afin de suivre, stocker, et transmettre différentes sortes de données. Par conséquent, ces systèmes intégrés doivent inclure des capteurs, des circuits électroniques, de la mémoire de données, et des transmetteurs. Pour la fabrication de ces systèmes, l'impression jet d'encre peut garantir un faible coût de production tout en offrant des dispositifs flexibles. Bien que des capteurs, circuits, et transmetteurs imprimés existent déjà, personne n'a encore rapporté une mémoire imprimée par jet d'encre satisfaisante.

Le but de cette thèse est d'adresser les exigences restantes en ce qui concerne les dispositifs mémoire imprimés afin de complémenter un système imprimé à faible-coût qui facilitera l'"Internet des Objets".

À cet égard, la mémoire résistive est particulièrement intéressante pour le procédé d'impression de par sa simple structure triple-couches. Nos cellules mémoire consistent en une électrode inférieure d'Ag électrochimiquement active, une couche isolante de  $\text{SiO}_2$  ou  $\text{WO}_3$ , et une électrode supérieure constituée d'un polymère inerte conducteur. L'état logique ("0" ou "1") de la cellule mémoire est défini par sa résistance, mesurée entre les deux électrodes. Alors que l'état initial isolant démontre une haute résistance, la cellule peut être commutée de façon réversible vers un état de faible résistance. Pour ce faire, un filament d'Ag connectant les électrodes peut être formé en appliquant les tensions appropriées et ainsi réduire la résistance de la cellule.

Nous présentons des cellules mémoire complètement imprimées avec une endurance élevée, une longue rétention, et un degré de flexibilité élevé. Dans le but de développer une cellule mémoire trouvant différentes applications, nous proposons des cellules avec différentes structures capables de répondre aux exigences spécifiques des applications possibles. Ainsi, les structures spécifiques des cellules sont optimisées pour offrir soit une transparence élevée, soit une flexibilité accrue, soit une fabrication sans frittage.

L'excellente flexibilité de nos cellules mémoire est testée à l'aide d'un système pivoter-et-plier fait-maison : les cellules restent totalement opérationnelles après 500,000 cycles de flexions avec un rayon de 3 mm. La microscopie à force atomique en mode de conduction ainsi que la microscopie électronique à balayage à sonde ionique focalisée confirment la nature filamentaire du mécanisme de commutation. Un modèle basé sur les dimensions du filament et la théorie de diffusion de Fick est développé afin de quantifier la rétention de l'état de faible résistance, qui est limitée par la diffusion spontanée du filament d'Ag. Pour finir, l'aptitude des cellules mémoire à agir comme des synapses artificielles dans le cadre de l'informatique neuromorphique est

étudiée. Les facteurs influençant la réponse d'apprentissage des cellules sont quantifiés, et ainsi leur processus d'apprentissage est optimisé.

# Abstract

The full implementation of the "Internet of Things" will require a large number of low-cost embedded systems to track, store, and transmit various types of data. Therefore, these embedded systems have to include sensors, electronic circuits, data memory, and transmitters. For the fabrication of these systems, inkjet printing can guarantee low-cost production while enabling flexible devices. Although printed sensors, circuits, and transmitters already exist, satisfactory inkjet-printed memory has not been reported.

The goal of this thesis is to address the unresolved need for printed memory devices to complement low-cost printed system which will facilitate the "Internet of Things".

In this regard, resistive memory is particularly attractive for the printing process due to its simple three-layered structure. The memory cells consist of an electrochemically active bottom electrode of Ag, an insulating layer of  $\text{SiO}_2$  or  $\text{WO}_3$ , and a top electrode of an inert conducting polymer. The logical state ("0" or "1") of the memory cell is defined by its resistance measured between the two electrodes. While the initial, insulating state shows a high resistance, the cell can be switched reversibly to a low resistance state. To that end, by applying appropriate voltages, an Ag filament can be formed as a connection between the electrodes and thus lowers the resistance of the cell.

Fully inkjet-printed memory cells with a high endurance, long retention, optical transparency, and a high degree of flexibility are fabricated. Driven by the motivation to establish memory cells for different application scenarios, different cell structures are developed to fit specific demands for possible applications. Thus, specific cell structures are optimized for either high optical transparency, enhanced flexibility, or the potential to be sinter-free.

The memory cells' excellent flexibility is tested in the in-house built rotate-to-bend device: the cells are still fully functioning after 500,000 bending cycles at a radius of 3 mm. Conductive Atomic Force Microscopy and Focused Ion Beam Scanning Electron Microscopy confirm the filamentary nature of the switching mechanism. Based on the filament dimensions and Fick's theory of diffusion, a model is developed to quantify the retention of the low resistance state, which is limited by spontaneous diffusion of Ag atoms at the Ag filament. Finally, the memory cells' suitability to act as artificial synapses in the framework of neuromorphic computing is investigated. Factors influencing the cells' learning response are quantified and thus, their learning behavior in artificial neural networks could be optimized.



# Sommaire récapitulatif

## Introduction

L'électronique imprimée représente une part du marché en plein essor. De 2010 à 2016, ce secteur est passé d'une valeur de 5,6 milliards à 26,9 milliards de dollars américains sur le marché [121]. Cette croissance extrêmement rapide est due aux nombreux avantages de l'électronique imprimable, comparés à la technologie standard à base de semi-conducteurs [22]:

- Un faible coût de production : les procédés de fabrication de semi-conducteurs nécessitent l'investissement de milliards de dollars américains, tandis que l'électronique imprimable peut être fabriqué à l'aide d'une simple imprimante de bureau à jet d'encre [4]
- Le procédé d'impression additive n'est pas limité par les gaufres de substrats, mais peut au contraire exploiter toutes sortes de feuilles et même du papier en guise de substrat
- L'impression sur demande offre une production extrêmement versatile et personnalisable
- L'utilisation d'un substrat flexible offre une flexibilité mécanique au dispositif <sup>1</sup>

Grâce à tous ces avantages, l'électronique imprimable est devenue une des technologies apportant une contribution majeure dans l'"Internet des objets", dans le cadre de la "4<sup>me</sup> révolution industrielle" [22]. Un activateur clé de l'Internet des objets sera le faible coût des systèmes intégrés, qui permettront de monitorer et contrôler la production en chaîne, ou le suivi de paramètres environnementaux par des systèmes intelligents [74]. Ces systèmes doivent suivre, stocker et idéalement traiter toutes sortes de données à l'aide de capteurs, circuits électroniques et transmetteurs.

L'électronique imprimable possède la maturité technologique nécessaire à la manufacture de la plupart des composants requis avec les techniques d'impression. L'impression de capteurs de pression, contrainte, température ou humidité parmi tant d'autres a déjà été réalisée [64]. Des transmetteurs de données sans contact ont été imprimés dans des étiquettes d'identification par radio fréquence [60] et des batteries imprimées peuvent faire lieu de sources de courant pour les systèmes intégrés [40]. D'autres composants électroniques tels que des résistances, des capteurs, et des inducteurs peuvent être imprimés pour la mise au point de circuits électroniques

---

<sup>1</sup>Une puce de silicium dénote un certain degré de flexibilité quand son épaisseur est réduite de plusieurs  $\mu\text{m}$  et peut ainsi être intégrés dans l'électronique flexible. Cependant, les autres avantages mentionnés ci-dessous concernant l'électronique imprimable n'entrent pas en jeu car les connexions entre la puce de silicium et la feuille de substrat peuvent être néfastes.

complètement imprimés [61]. Les transistors imprimés ont déjà été démontrés en 1994 [41], et de nos jours, des diodes complètement imprimées avec des fréquences d'opération de 1.6 GHz sont disponibles [115]. Cependant, afin de fabriquer des circuits imprimés complets, chaque élément du circuit doit être imprimable, incluant l'unité de mémoire. L'impression de dispositifs mémoires n'a pas encore atteint la maturité technologique requise. Dans ce cadre, les mémoires résistives à accès aléatoires (ReRAM - Resistive Random Access Memory) sont de bonnes candidates pour l'impression car elles possèdent une simple structure constituée de trois couches, avec une cellule unitaire minimum de  $4 F^2$ , où  $F$  est la taille de la plus petite caractéristique donnée par le procédé de manufacture. Les faibles dimensions de la cellule unitaire peuvent partiellement contrebalancer les grandes dimensions des éléments du processus d'impression, en comparaison à la lithographie.

Les travaux antérieurs sur des dispositifs ReRAM tout imprimés utilisent principalement l'impression électrohydrodynamique [5][111], qui permet d'atteindre une résolution d'impression plus élevée [66]. Néanmoins, cette méthode est plus complexe que l'impression à jet d'encre standard, ce qui empêche son implémentation industrielle. En 2015, Nau et al. ont présenté la première mémoire unipolaire totalement imprimée par jet d'encre, avec un rendement inférieur à 20 % [100]. Actuellement, tous les autres dispositifs fabriqués par impression à jet d'encre standard nécessitent des étapes de traitement additionnelles telles que la structuration par lithographie ou l'électroplaquage [134][142].[51] <sup>2</sup>

Le but de cette thèse est de combler les besoins encore non satisfaits des dispositifs mémoires imprimés pour compléter un système imprimé à faible coût qui sera utile à l'"Internet des objets".

## La commutation de résistance

Le but principal de cette thèse est de fabriquer des cellules mémoires résistives complètes par impression jet d'encre. Ainsi, cette section vise à donner au lecteur l'information et les principes théoriques fondamentaux nécessaires à la compréhension et à l'interprétation des résultats expérimentaux.

Pour chaque nouvelle technologie mémoire, l'unité de base de mémoire, aussi appelée cellule mémoire, doit pouvoir être variée entre les deux états logiques "0" et "1" pour permettre la logique binaire. "RAM Résistive" est un terme descriptif étant donné que les états logiques sont définis par la résistance de la cellule mémoire : un état de haute résistance (HRS) correspond au "0", et un état de basse résistance (LRS), au "1". Nous utilisons les cellules métallisées électrochimiques (ECM-*Electrochemical Metallization Memory*), une sous-classe de ReRAM.

Grâce à leur variabilité à plusieurs niveaux, les cellules ECM sont particulièrement intéressantes dans le domaine en plein essor de l'informatique neurmorphique. De ce fait, nous motivons les applications neuromorphiques et décrivons comment les ECM peuvent être exploitées de façon avantageuse dans ce contexte.

---

<sup>2</sup>Premiers résultats sur les mémoires flash imprimées ont été rapportées. Elles requièrent également des étapes de photolithographie et de revêtement [9].

## Mécanismes de commutation de résistance dans les mémoires métallisées électrochimiques

Une cellule ECM est composée d'une couche isolante séparant deux conducteurs d'électrons (généralement différents) en guise d'électrodes. La résistance entre les deux électrodes définit l'état logique de la cellule ECM et peut être variée entre au moins deux états résistifs différents (HRS et LRS) en appliquant des tensions appropriées aux électrodes. Ceci peut arriver à travers deux différents mécanismes : la commutation bipolaire, et la commutation unipolaire. La commutation unipolaire est indépendante de la polarité de la tension et n'est pas le sujet de l'étude présentée ici. La commutation bipolaire quant à elle apparaît dans les structures asymétriques et dépend de la polarité de la tension. La commutation de HRS à LRS (processus de SET) puis de LRS à HRS (processus de RESET) n'a lieu que pour différentes polarités de la tension appliquée.

Dans le cas d'une commutation bipolaire dans l'ECM, une des électrodes est composée d'un métal oxydable, tel que l'Ag ou le Cu, tandis que l'autre électrode consiste en un matériau électrochimiquement inerte (ex : Pt ou polymères inertes). Bien que les mémoires soient variées et lues par des dispositifs pulsés, une commutation avec balayage triangulaire, "quasi-statique", en tension révèle des informations supplémentaires sur le mécanisme de commutation (voir Fig. 1). Quand une tension est appliquée entre les deux électrodes, où une électrode positive active est définie comme la tension négative, le diagramme courant-tension démontre un très faible courant dans les faibles tensions positives. Ceci représente le HRS initial, qui est dominé par l'émission thermoionique, ou flux de courant limité par les charges d'espace à travers la couche isolante (encadré A) [25]. Quand une tension suffisamment élevée est atteinte, les atomes de l'électrode active (ici Ag) sont oxydés et les ions Ag positifs migrent vers l'électrode inerte négativement polarisée. Là, ils sont réduits et forment un électro-dépôt d'argent élémentaire (encadré B). Puisque le champ électrique est plus élevé dans le premier électro-dépôt, un électro-dépôt subséquent se poursuit au même endroit, résultant ainsi en la croissance d'un filament allant de l'électrode inerte à l'électrode active. Quand le filament atteint l'électrode active, la cellule change vers le LRS (encadré C). Pendant et après ce processus de SET, un courant de contrôle externe limite le flux de courant afin d'éviter que les courants en excès n'endommagent la cellule.

Pour le processus de RESET, du HRS au LRS, la tension doit être inversée, c'est-à-dire que l'électrode active doit être chargée négativement. La dissolution du filament au cours du RESET est déterminée par la forte asymétrie morphologique entre le filament d'argent en forme d'aiguille et l'électrode active [46]. À l'interface entre le filament et l'isolant, la dissolution électrochimique à lieu et l'Ag va se redéposer. À l'endroit où le filament en contact avec l'électrode active est le plus mince, l'effet Joule amplifie fortement le processus, donnant lieu au mûrissement d'Ostwald et à rupture du filament [137, p.698]. Une fois le filament rompu, le processus électrochimique et la migration des ions dissolvent le filament de nouveau. Les atomes d'argent du filament sont à nouveau oxydés et les ions d'Ag migrent une fois encore vers l'électrode active polarisée négativement, où ils sont réduits (encadré D). Le RESET rétablit le HRS à travers une dissolution complète ou partielle du filament, en laissant des restes de filament déconnecté.

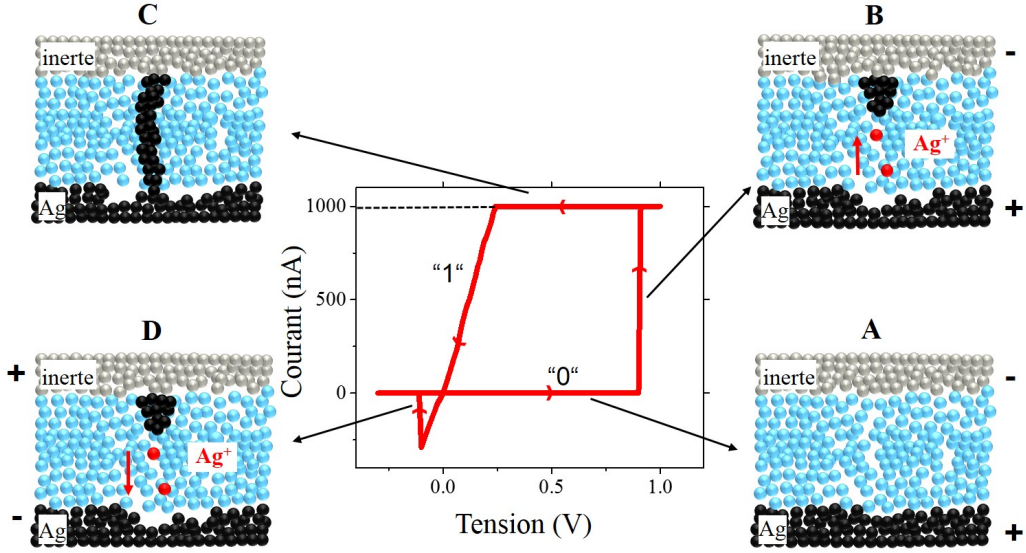


Figure 1: Variation bipolaire de mémoire ECM : (A) état OFF à haute résistance, (B) croissance de filament, (C) état ON à faible résistance, (D) dissolution du filament sous une tension inversée. L’encadré au centre démontre la caractéristique courant-tension correspondante, avec une tension SET d’environ 0.9 V et un courant de contrôle de  $1 \mu\text{A}$ . Adapté de [130]

La commutation unipolaire apparaît typiquement dans les cellules ayant une structure symétrique avec deux électrodes actives. Le processus SET équivaut à une commutation bipolaire où la commutation peut avoir lieu pour les deux polarités de la tension. Alors qu’un courant de contrôle est utilisé durant le SET, le RESET a lieu sans compliance et ainsi à un courant élevé dans la gamme des micro et milliampères et pour de faibles tensions comparées au SET. Par conséquent, la rupture du filament durant le RESET est due à une dégradation thermique causée par l’effet Joule. Après la rupture initiale, la dissolution du filament due à la tension appliquée est analogue au RESET bipolaire.

Pour les deux mécanismes de commutation, de nombreux matériaux sont des isolants adéquats, parmi lesquels figurent  $\text{Ag}_2\text{S}$ ,  $\text{ZnO}$ ,  $\text{SiO}_2$ ,  $\text{GeSe}$ , ainsi que certains polymères [59][68][116][140][97]. La plupart des matériaux requièrent un processus d’électroformage initial afin d’effectuer la première commutation dans la cellule vierge. Cet électroformage est une dégradation diélectrique douce limitée par le courant durant le premier SET. La formation du premier filament définit un modèle structural dans la matrice de l’isolant et assure une croissance préférentielle du filament durant les cycles de commutation subséquents [137, p.697]. Ainsi, pour la plupart des matériaux, la première opération SET nécessite une tension beaucoup plus élevée que les cycles subséquents. La limite de courant externe durant l’opération SET limite le courant ionique qui peut circuler durant la commutation. De ce fait, elle contrôle la quantité d’ions métalliques qui contribuent au diamètre du filament, et par conséquent, la résistance de celui-ci. Un faible courant de contrôle garanti un filament mince et une haute résistance dans le LRS, tandis qu’une valeur élevée conduit à un filament épais avec un LRS de faible résistance. Ceci permet d’augmenter la densité de

cellules mémoires du stockage de données multi-bits. Une cellule peut seulement stocker les deux états logiques HRS et LRS, mais le LRS peut être divisé en plusieurs états logiques à travers différents diamètres de filament et différentes résistances. La création de  $2^n$  états distinctifs sur une même cellule conduit à une quantité  $n$  de bits pouvant être stockés dans la cellule. 4 états différents, le HRS et 3 différents LRS, peuvent être attribués à 4 états logiques différents : "00", "01", "10", et "11", et ainsi représenter 2 bits en terme de stockage de données.

## La mémoire résistive pour l'informatique neuromorphique

Le cerveau humain surpassé de très loin les ordinateurs en ce qui concerne le traitement en temps réel de données non structurées telles que la reconnaissance de voix, d'images, ou vidéo. Ceci est dû à sa structure qui diffère radicalement de celle d'un ordinateur : elle est extrêmement parallèle avec une organisation tridimensionnelle et combine stockage et traitement [69]. Ceci engendre un rendement énergétique bien supérieur avec une consommation d'énergie de seulement environ 15 W pour un cerveau humain [3]. En revanche, les ordinateurs construits pour performer des tâches comparables à l'aide de la logique CMOS et l'architecture von-Neumann ont des consommations énergétiques dans la gamme des kW aux MW. IBM a simulé une architecture informatique avec  $5.3 \cdot 10^{11}$  neurones,  $1.37 \cdot 10^{14}$  synapses, qui représentent les valeurs réelles du cerveau humain. Le superordinateur requis pour cette opération utilisait une puissance de 7.9 MW et fonctionnait 1542 fois moins vite que le temps réel [56][138].

Par conséquent, une simple simulation de l'architecture à l'aide de la logique CMOS ne suffit pas à créer un réseau neuronal artificiel (ANN- Artificial Neuronal Network) capable d'imiter l'architecture du cerveau. Au contraire, la structure du cerveau doit être reproduite directement avec les dispositifs appropriés. Ici, une cellule ECM peut imiter la fonction d'une synapse et reproduire sa plasticité, un paramètre essentiel au processus d'apprentissage. Une synapse située entre deux neurones peut modifier graduellement sa résistance électrique et ainsi créer des connexions plus fortes ou plus faibles entre les neurones. La plasticité synaptique, c'est-à-dire la capacité des synapses de se renforcer ou s'affaiblir, peut être émulée en renforçant ou affaiblissant le filament métallique des cellules ECM. Pour ce faire, la cellule ECM doit pouvoir assurer un stockage de données multi-bits, où sa résistance varie à travers un changement du rayon du filament quand la cellule est stimulée avec différents courants de contrôle ou des pulses de tension adaptées (voir fig. 6).

Fig. 2 présente une cellule ECM constituée d'une synapse située entre deux neurones. La connexion synaptique est directionnelle, nous permettant ainsi de distinguer le neurone présynaptique, du neurone post-synaptique. Un neurone peut être représenté comme un dispositif intégrer-et-tirer, où les impulsions envoyées par les autres neurones sont intégrées, et, quand une limite est atteinte, le neurone "tire" une impulsion à son tour. Dans les domaines de la biologie et la neurobiologie, les impulsions sont fréquemment appelées potentiels d'action. Les impulsions de neurones pré- et post-synaptiques passent à travers une synapse. La plasticité du processus d'apprentissage, c'est-à-dire l'augmentation ou diminution de la résistance de la synapse, est liée à l'intervalle de temps  $\Delta t$  entre deux impulsions émises par les neurones pré- et post-

synaptiques. Une impulsion présynaptique suivie par une impulsion post-synaptique ( $\Delta t$  positif) indique un lien de causalité, dans lequel le neurone présynaptique déclenche un tir du neurone post-synaptique. Donc, la synapse réduit sa résistance pour amplifier ce type d'interaction par la suite. De la même manière, un  $\Delta t$  négatif (l'impulsion post-synaptique précède l'impulsion présynaptique) conduit à une augmentation de la résistance de la synapse, car une impulsion post-synaptique déclenchant un tir du neurone présynaptique irait à l'encontre de la direction de causalité entre deux neurones par la suite. Ce renforcement, ou affaiblissement, de la synapse en fonction de  $\Delta t$  est nommé la plasticité fonction du temps d'occurrence des impulsions (STDP-Spike-timing-dependant plasticity).[65]

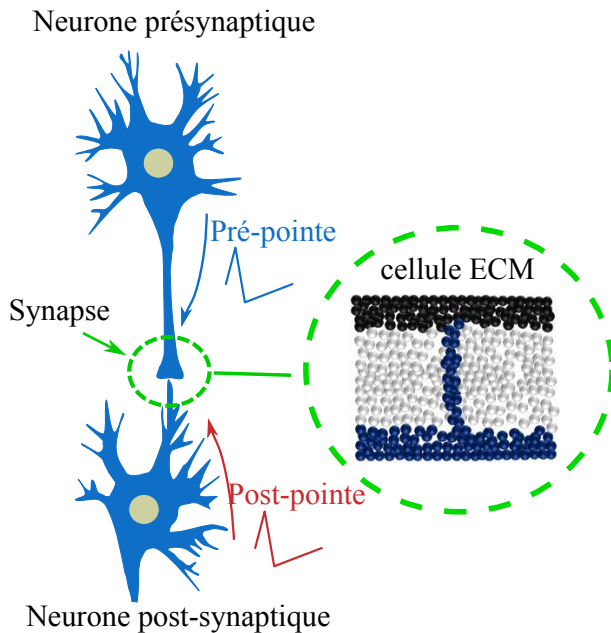


Figure 2: Une cellule ECM peut adopter le comportement d'une synapse. La plasticité synaptique, c'est à dire la variation graduelle de la résistance de la synapse, est due à une augmentation ou diminution du diamètre du filament métallique.

Un schéma du phénomène d'apprentissage synaptique STDP est dépeint dans la fig. 3. Pour la synapse, les impulsions arrivant des deux différents neurones ont des polarités différentes. Dans notre cas, les impulsions individuelles consistent en deux branches exponentielles de polarités opposées (voir encadrés de la fig. fig. 3). L'amplitude en tension des impulsions individuelles est ajustée afin que les amplitudes restent inférieures au seuil de tension de la cellule ECM. Ainsi, les impulsions individuelles n'affectent pas la résistance de la cellule, tandis que seule une superposition entre les impulsions pré- et post-synaptiques peut déclencher une modification du filament. Si l'impulsion présynaptique à lieu avant l'impulsion post-synaptique ( $\Delta t$  positif), la branche exponentielle positive de l'impulsion présynaptique se superpose à la branche post-synaptique positive inversée. Ceci résulte en une impulsion plus élevée qui déclenche la synapse et créer une potentiation (voir encadré de la fig. 3). La cellule ECM passe graduellement à l'état SET, menant ainsi à un filament métallique plus épais et une diminution de la résistance. Pour un

$\Delta t$  négatif, l'impulsion post-synaptique précède l'impulsion présynaptique et la haute tension négative qui en résulte induit une diminution de la synapse, c'est-à-dire un RESET gradué de la cellule ECM.

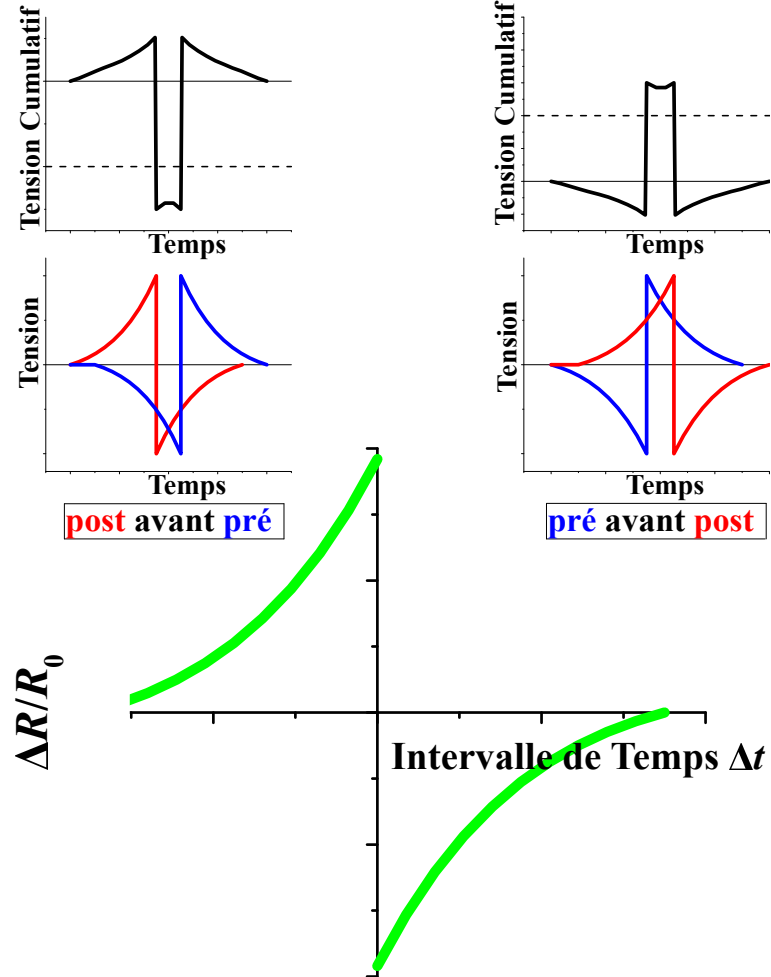


Figure 3: Schéma de la loi d'apprentissage par plasticité fonction du temps d'occurrence des impulsions (STDP) avec une pulse de tension exponentielle. Les encadrés présentent la façon dont les impulsions pré- et post-synaptiques se superposent à la tension cumulative. Pour un  $\Delta t$  approprié, cette tension cumulative peut excéder le seuil de tension (ligne en pointillés) nécessaire à un changement gradué de la résistance de la cellule.

Un système informatique efficace avec un ordinateur possédant une architecture artificielle inspirée par le cerveau demande une combinaison spécifique de cellules ReRAM formant un réseau. Un ANN est donné par des groupes de noeuds interconnectés, où chaque noeud représente un neurone et chaque connexion, une synapse. La conductance de la synapse est appelée son poids synaptique  $w_{ij}$ . Les valeurs d'entrée  $V_i$  sont connectées aux valeurs de sortie  $I_j$  de la couche de noeuds suivant à travers la somme des masses de toutes les connexions impliquées :  $I_j = \sum_i w_{ij} V_i$ . Durant l'apprentissage supervisé dans un algorithme d'apprentissage automatique, les poids de l'ANN sont ajustés par un jeu de données d'entraînement. Par exemple, pour un algorithme de

reconnaissance de visage par ANN, chaque noeud de la couche de saisie représente un pixel de l'image étudiée. Cette information est réduite à travers une ou plusieurs couches cachées et la couche de sortie contient uniquement l'information "visage de la personne A" ou "pas le visage de la personne A".

## Section expérimentale

Cette thèse vise à démontrer la faisabilité de cellules mémoires résistives totalement imprimées par jet d'encre. La structure nanoparticules d'Ag/SOG/PEDOT:PSS de la cellule assure une haute endurance, un degré de flexibilité élevé, et un grand potentiel de stockage de données multi bits, grâce à une grande différence entre HRS et LRS [51].

La commutation des cellules par microscopie à force atomique en mode conduction de courant (C-AFM- Conductive-Atomic Force Microscopy), suivie d'une mesure en vue de coupe par microscopie électronique à balayage à sonde ionique focalisée (MEB-FIB) met en valeur la nature filamentaire de la commutation. Des tests de flexion mécanique démontrent les excellentes performances du dispositif quand il est soumis à des déformations par flexion, tandis que des mesures STDP permettent d'investiguer la capacité qu'ont les cellules de servir dans l'informatique neuromorphique.

### Commutation de résistance dans les cellules imprimées nanoparticules d'Ag/verre déposé/polymère

$\text{SiO}_2$  déposé par pulvérisation ou par évaporation thermique est une couche isolante communément utilisée dans les cellules ECM [127][117].  $\text{SiO}_2$  est une excellant isolant électronique, mais il peut aussi agir comme une matrice pour la formation du filament grâce à une conductivité ionique suffisamment élevée [129]. SOG, qui condense pour former une couche  $\text{SiO}_x$ , a été développé pour reproduire les caractéristiques des couches  $\text{SiO}_2$  et peut donc être utilisé dans les cellules ECM [94].

La ligne de nanoparticules d'Ag imprimée ou déposée par frittage sert d'électrode d'active. Les nanoparticules étant bien connectées à travers le frittage, son comportement est comparable à celui d'une électrode évaporée ou même massive. Le PEDOT:PSS imprimé agit comme une électrode supérieure inerte.

Dans un dispositif fonctionnel, où la rapidité est importante, une cellule mémoire sera toujours commuté et lire par de courtes pulses de tension. Toutefois, un balayage en tension quasi-statique accroît graduellement la tension en une fonction escalier et révèle des paramètres de commutation critiques : la tension de commutation  $V_{\text{SET}}$  de HRS à LRS, la tension de commutation négative  $V_{\text{RESET}}$  de LRS à HRS, les valeurs des résistances HRS ( $R_{\text{OFF}}$ ) et LRS ( $R_{\text{ON}}$ ), et le courant de contrôle prédéfini  $I_{\text{cc}}$ . Fig. 4(a) présente une mesure typique courant-tension dans une cellule complètement imprimée d'Ag/SOG/PEDOT:PSS. Le balayage va de 0 V à 1 V, puis redescend

à -0.2 V, avant de remonter à 0 V avec un pas de 0.01 V. La cellule passe au LRS à une tension de 0.49 V, où elle atteint directement la limite de courant de  $1 \mu\text{A}$ . À une tension de -12 mV, la cellule repasse au HRS. La pente linéaire de la fig. 4(a) donne les valeurs de la résistance, qui peuvent être plus facilement extraites de la courbe résistance-tension de la fig. 4(b) :  $R_{\text{OFF}}$  est supérieur à  $1 \text{ G}\Omega$  et représente un courant de fuite extrêmement faible à travers la couche SOG. Cette valeur surpassé la limite de détection de système de mesure et est ainsi soumise au bruit de la mesure.  $R_{\text{ON}}$  est de  $220 \text{ k}\Omega$  pour le courant de contrôle utilisé ici.

L'endurance décrit le nombre maximum de cycles de commutation possible avant défaillance

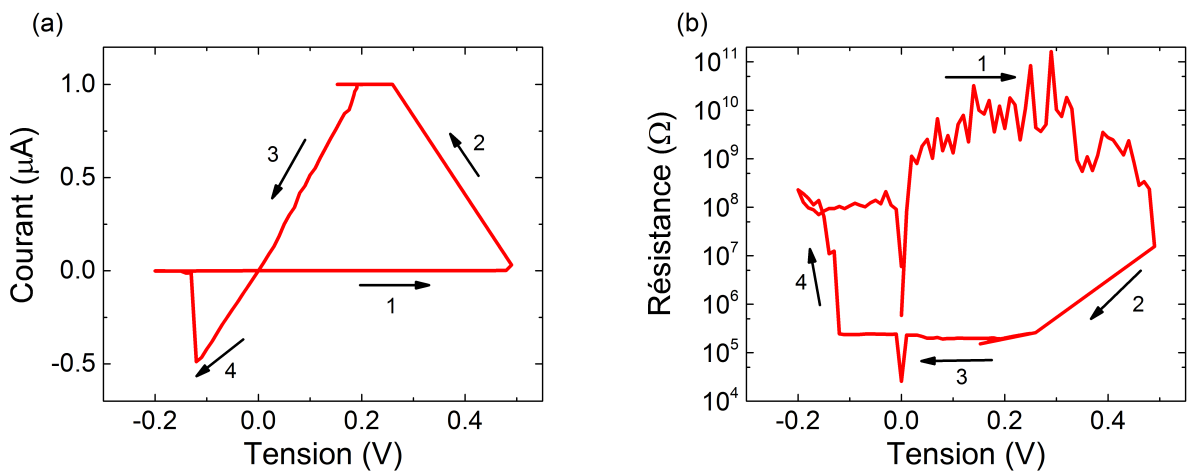


Figure 4: Courbes (a) courant-tension quasi-statiques et (b) résistance-tension mesurées sur une cellule Ag/SOG/PEDOT:PSS avec un courant de contrôle de  $1 \mu\text{A}$ .

du dispositif, et représente un paramètre très important pour un dispositif de stockage de données. De nos jours, ce paramètre varie entre  $10^3$  pour une mémoire flash, et  $10^{17}$  pour une RAM dynamique. Tandis que les dispositifs ReRAM démontrent déjà des endurances de  $10^{12}$ , des cellules basées sur le mécanisme ECM avec une endurance de  $10^6$  ont été rapportées mais présentent généralement des endurances beaucoup plus faibles dans la gamme de  $10^3$ - $10^4$  [72][19]. Le test d'endurance, dépeint dans la Fig. 5, démontre une commutation stable pour plus de 1000 cycles. Chaque cycle d'endurance consiste en un balayage en tension quasi-statique allant de 0 V à 3 V, puis à -0.2 V, avant de revenir à 0 V, avec un courant de contrôle de  $10 \mu\text{A}$ . La tension SET augmente avec le nombre de cycles jusqu'à ce que 3 V ne suffisent plus au procédé SET, autour de 1100 cycles. Après le test d'endurance, la cellule repasse au LRS à 5.5 V.[51]

Une analyse de défaillance du dispositif démontre que plus de 80 % d'un même lot cellules mémoires imprimées est fonctionnel. Les dysfonctionnements sont principalement causés par des courts circuits entre les électrodes inférieure et supérieure dû à un défaut dans l'impression. En ce qui concerne la densité de mémoire, l'électronique imprimée en général se trouve confrontée au problème de caractéristiques latérales extrêmement larges comparées à la photolithographie. Alors que la photolithographie offre des traits dans la gamme des nm, l'impression jet d'encre ne peut pas descendre au-dessous de dizaines de  $\mu\text{m}$  pour la majorité des matériaux. De ce

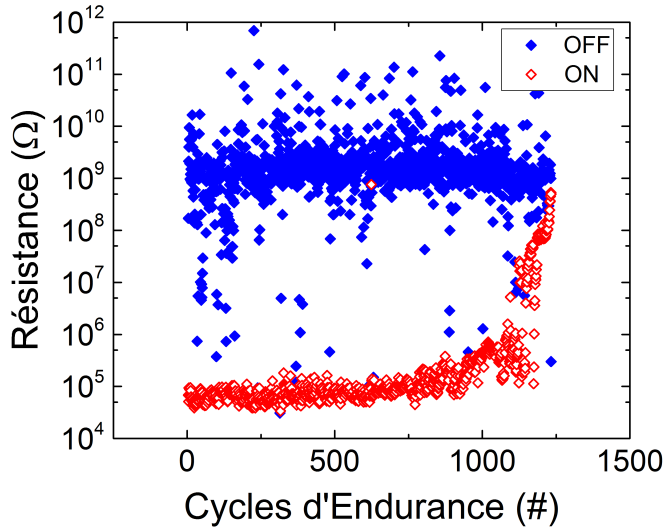


Figure 5: Endurance d'une cellule Ag/SOG/PEDOT:PSS mesurée à l'aide de balayages en tension quasi-statiques et un courant de contrôle de  $10 \mu\text{A}$  [51].

fait, l'option de stockage de données multi bits décrite dans la section peut être exploitée pour augmenter de façon avantageuse la densité de mémoire.

Fig. 6 présente les résultats des balayages en tension quasi-statiques avec un  $I_{cc}$  variant de plus de quatre ordres de grandeur, de  $10 \text{nA}$  à  $100 \mu\text{A}$ .  $R_{ON}$  couvre plus de trois ordres de grandeur, de  $40 \text{ M}\Omega$  à  $10 \text{nA}$ , à  $21 \text{k}\Omega$  à  $100 \mu\text{A}$ . Pour les valeurs d' $I_{cc}$  inférieures, le LRS résultant devient très instable. La quantité d'ions Ag qui forment le filament ne suffit très probablement plus à une connexion stable pour de si faibles courants. Pour  $I_{cc} > 100 \mu\text{A}$ , les cellules sont bloquées dans le LRS et ne peuvent pas commuter vers le HRS. Le filament devient trop épais pour être électrochimiquement réversible.

La structure triple-couches d'une cellule ECM avec un isolant situé entre deux électrodes interdit l'étude directe du filament métallique. Pour cette raison, nous utilisons le CAFM sur une structure bicouche consistant en une électrode inférieure d'Ag couverte par un film de SOG. Au lieu d'une couche de PEDOT :PSS, une pointe recouverte de Pt/Ir sert d'électrode supérieure inerte. Une tension négative appliquée sur la pointe crée un filament d'Ag local. Les changements dans la topographie et dans la conductivité locale causés par le filament peuvent être mesuré par des scans CAFM. Durant les scans AFM, les échantillons sur des substrats flexibles démontrentraient une détérioration de la topographie causée par une possible flexion. C'est pourquoi nous utilisons des morceaux de gaufres de Si rigides couverts de  $100 \text{ nm}$  de  $\text{SiO}_2$  isolant en guise de substrats pour les mesures AFM. Après avoir formé le filament par CAFM, nous étudions la section transversale à l'aide d'un système MEB-FIB.

Les changements topographiques et les variations de conductivité provenant de la commutation locale filamentaire peuvent être observés dans la fig. 7. La surface scannée de la fig. 7(a) est prise sur une ligne d'Ag imprimée et couverte de SOG, et dénote une surface lisse avec un écart type de  $2.23 \text{ nm}$ . Une tension de  $0.5 \text{ V}$  appliquée sur la pointe engendre l'image de courant de la

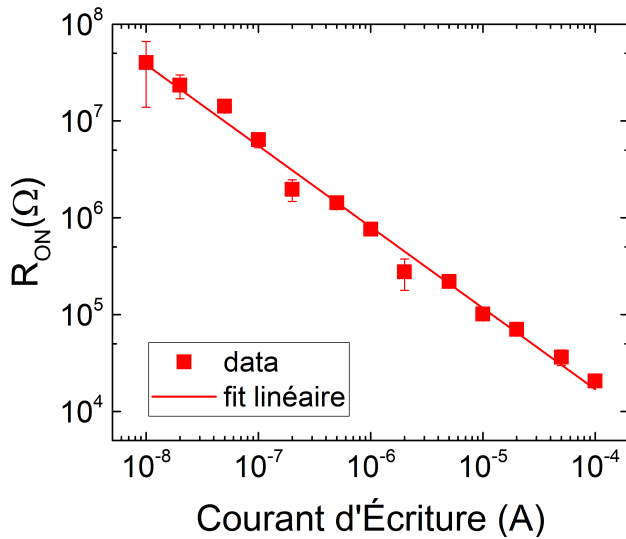


Figure 6: Résistance ON en fonction du courant de contrôle pour une cellule Ag/SOG/PEDOT:PSS. Le balayage en tension varie de 0 V à 3 V avant de redescendre à 0.2 V avec un courant de contrôle de 10 nA à 100  $\mu$ A.

fig. 7(b), et confirme l'excellente isolation de la couche SOG. Seul un bruit de courant de quelques pA lié au système expérimental est détecté. Suite au scan CAFM initial, la pointe est placée au milieu de la surface de scan et nous appliquons un balayage en tension quasi-statique allant de 0 V à -9.9 V, puis de retour à 0 V avec un courant de 100 nA et une résistance de contrôle de 10 M $\Omega$ . Nous créons localement un filament d'Ag à l'emplacement de la pointe et dans un scan CAFM subséquent (fig. 1.7(c)), un tertre correspondant au filament apparaît à l'endroit de la commutation. Le tertre a une hauteur d'environ 150 nm, un diamètre de 400 nm et consiste en atomes d'Ag ayant traversé la surface SOG et formé le premier électrodépôt. Ceci est appuyé par l'image de courant dépeinte dans la fig. 7(d), qui démontre une conductivité électrique au centre du tertre filamentaire. La partie extérieure du tertre qui ne contribue pas au signal est probablement l'Ag qui reste couvert par le SOG. À cet endroit, l'électrodépôt d'Ag pourrait avoir soulevé le SOG, causant ainsi une variation dans la hauteur, sans toutefois percer la surface du SOG, et ainsi, ne contribue pas au courant. Le courant maximum de 50 nA est directement relié à la résistance de contrôle de 10 M $\Omega$  à une tension de scan de 0.5 V, indiquant ainsi que la résistance du filament doit être bien inférieure à 10 M $\Omega$ .

L'écriture d'un réseau de filaments est essentielle à l'étude en vue de coupe des filaments par MEB-FIB : un filament unique indéfini par le système CAFM est difficilement localisé et détecté par le MEB à cause de ses faibles dimensions latérales sur la vaste surface isolante. De plus, la découpe du filament en son milieu nécessaire pour révéler sa section transversale est extrêmement difficile. Aussi, le fraisage et le polissage de la section transversale par faisceau de Ga entraîne plus probablement la disparition du filament. Pour cette raison, nous inscrivons une ligne de filaments par CAFM avant de couper l'échantillon de façon perpendiculaire à la ligne avec le faisceau de Ga du MEB-FIB. Cette procédure fait en sorte que la section transversale révèle la

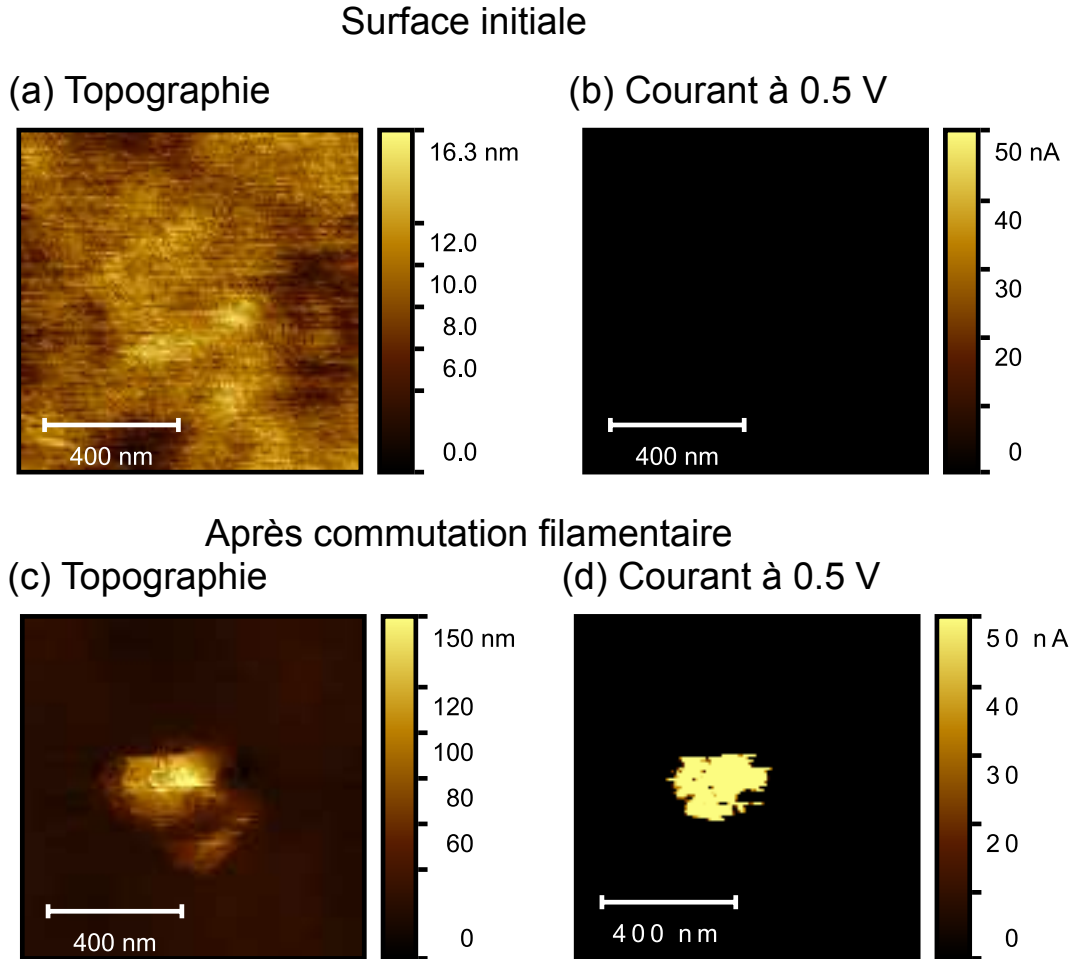


Figure 7: Formation d'un filament local dans les cellules imprimés Ag/SOG. (a) Topographie de la surface plate avec un écart type de 2.23 nm et (b) image de courant avec une tension dans la pointe de 0.5 V démontrant le SOG isolant. (c) Topographie après la formation du filament au milieu de la zone de scan avec un balayage en tension de 0 V à -9.9 V, puis à 0 V, un courant de 100 nA, et une résistance de contrôle de  $10 \text{ M}\Omega$ . (d) Image de courant de 0.5 V démontrant la conductivité électrique du terte filamentaire. Les quatre scans ont une surface de  $1 \mu\text{m} \times 1 \mu\text{m}$  et contiennent 127 x 127 pixels.

portion du filament que nous voulons observer au lieu de l'enlever.

Une découpe par FIB présente la section en vue de coupe des couches Ag/SOG dans les fig. 8(a) et (b). Avant la découpe de l'échantillon, nous déposons une couche protectrice de Pt avec un système d'injection à gaz directement au-dessus de la zone de découpe. Celui-ci augmente la précision de la découpe et la netteté des contours de la section transversale qui sont limitées par la forme Gaussienne de faisceau FIB [27]. L'image en vue de coupe de la surface donnée par le faisceau à électron secondaire est illustrée dans la fig. 8(a). La couche d'Ag imprimée ne forme pas une couche dense et uniforme, mais contient des vides causés par la densification de frittage. Le fait que la couche de Pt ne remplisse pas ces vides démontre que la couche de SOG recouvre complètement celle d'Ag. La rétrodiffusion d'électrons de l'image (b) donne un contraste mieux défini entre le SOG et l'Ag. Le nombre atomique plus élevé de l'Ag comparé à celui du Si et de

l’O du SOG crée plus d’électrons rétrodiffusés et apparait ainsi plus brillant dans cette image. Fig. 8(c) et (b) présentent la section transversale du filament d’Ag écrit par CAFM en une ligne perpendiculaire à la section transversale pour une tension de la pointe constante de -9.9 V et un courant de contrôle de  $10 \mu\text{A}$  balayant la surface à  $0.1 \mu\text{m s}^{-1}$ . Le tertre au-dessus du SOG est prononcé, avec un diamètre d’environ 200 nm. Il est composé d’Ag, qui s’est rompu sous la couche de SOG et s’est déposé au-dessus de celui-ci durant la commutation par CAFM. Dans l’image de rétrodiffusion d’électrons (b), nous pouvons voir que le filament est composé d’Ag ayant migré depuis l’électrode inférieure. L’électrode inférieure démontre un vide distinct juste à côté du filament, où l’Ag est consumé et les trous sont laissés à la place.

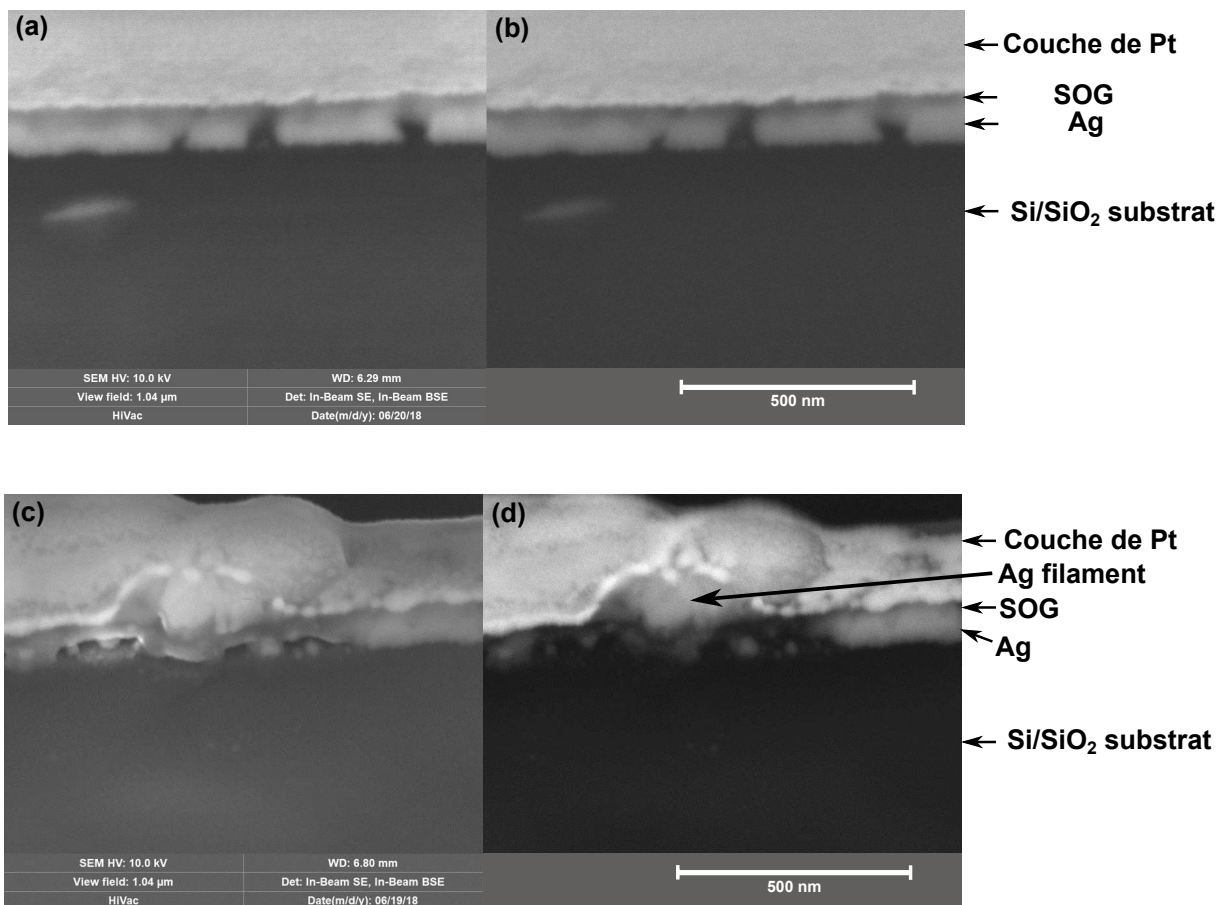


Figure 8: Images (a) d’électrons secondaires et (b) rétrodiffusés de section transversale de la structure Ag/SOG sur un substrat de Si avec une couche isolante de SiO<sub>2</sub> de 100 nm d’épaisseur. (c) Images d’électrons secondaires et (d) rétrodiffusés d’un filament d’Ag commuté à travers la surface de SOG par CAFM. Une ligne de filament est commutée en déplaçant une pointe CAFM à -9.9 V sur la surface à  $0.1 \mu\text{m s}^{-1}$ . La section transversale MEB-FIB est prise perpendiculairement à la ligne de filaments. Une couche protectrice de Pt est déposée sur l’échantillon avant d’effectuer la découpe par faisceau FIB.

## Caractérisation mécanique pour des applications flexibles

Dans cette section, nous étudions la flexibilité mécanique de nos cellules ECM imprimées sur substrats flexibles. Toutes les expériences sont conçues pour reproduire les exigences des applications spécifiques des dispositifs mémoires flexibles. Pour couvrir tous les champs d'application possibles, les attentes concernant la flexibilité peuvent être divisées en deux catégories. Tout d'abord, le dispositif mémoire doit fonctionner quand il est soumis à une déformation statique avec un rayon de courbure spécifique. Ceci concerne les applications pour lesquelles le dispositif doit s'adapter à une surface courbée, comme l'emballage intelligent. Ici, les cellules mémoires doivent commuter de façon reproductible avec un faible rayon de courbure sans que les paramètres de commutation ne dépendent de la contrainte appliquée. Ensuite, d'autres applications possibles incluent les cycles de flexion répétitifs, par exemple pour le lavage de textiles intelligents dans une machine à laver, ou les emballages en papier flexibles qui peuvent être pliés durant le transport. Nous monitorons cette flexion cyclique en suivant de façon continue les caractéristiques de commutation des cellules mémoires après de nombreux cycles et nous déterminons le point de rupture causé par la fatigue de la cellule.

Pour les tests statiques aussi bien que dynamiques, nous utilisons notre dispositif pivoter-et-plier car il offre la possibilité d'appliquer des déformations tensiles et compressives. De plus, cet appareil automatisé est spécialement utile aux tests de flexion cycliques, où des milliers de cycles de flexion doivent être appliqués.

Pour les tests de flexion statiques, nous courbons graduellement l'échantillon et mesurons le comportement électrique de l'échantillon courbé avec un rayon de courbure défini. Ces mesures in-situ sont permises par des connexions soudées sur l'échantillon. Ainsi, nous brossons de la peinture d'Ag *Acheson G 3692* sur les contacts de notre échantillon et soudons des fils de cuivre isolants de 75 µm d'épaisseur sur la peinture d'Ag. L'autre extrémité du fil est ensuite connectée à un système *Keithley 2400 Sourcemeter* pour de simples mesures de résistance des lignes d'électrode, ou des mesures par balayage des cellules complètes.

Dans un agencement crossbar, la flexion peut se produire dans toutes les directions et ainsi des contributions partielles courbées des mots et lignes bits des électrodes doivent être prises en compte. Néanmoins, la disposition typique de nos cellules consiste en une ligne de mots de l'électrode inférieure d'Ag et plusieurs autres lignes de bits plus courte de l'électrode supérieure PEDOT :PSS. Donc, pour les tests de cellules complètes, nous courbons seulement les cellules le long de l'électrode inférieure d'Ag, tandis qu'une déformation mineure est exercée le long de l'électrode supérieure perpendiculaire de PEDOT :PSS.

Des mécanismes de rupture possibles pour les cellules ECM soumises à une flexion statique pourraient être soit une haute variation de  $R_{ON}$  due à la déformation de la ligne d'électrodes, soit une augmentation irréversible de  $R_{ON}$  causée par une fissure dans les électrodes. Les déformations induites pas la contrainte dans la couche isolante de SOG peuvent aussi amener à un courant de fuite plus élevé et ainsi une réduction de  $R_{OFF}$ . Ces deux mécanismes de rupture mènent à un rétrécissement de la fenêtre entre  $R_{ON}$  et  $R_{OFF}$  et ainsi causent une dégradation de la commutation.

Fig. 9 présente  $R_{OFF}$  et  $R_{ON}$  dans une cellule nanoparticules d'Ag/SOG/PEDOT:PSS sur un film PEN de  $125 \mu\text{m}$ . Le rayon de courbure varie de  $8 \text{ mm}$  à  $2 \text{ mm}$ , où un rayon de courbure négatif correspond à une déformation compressive. L'état non-courbé est représenté par deux points de données au centre avec un rayon de courbure infini. Pour chaque rayon de courbure, un balayage en tension quasi-statique est appliqué allant de  $0 \text{ V}$  à  $1 \text{ V}$ , puis à  $-0.2 \text{ V}$ , avant de retourner à  $0 \text{ V}$ , avec un pas de  $0.01 \text{ V}$  et un courant de contrôle de  $2 \mu\text{A}$ . Chaque point de donnée  $R_{OFF}$  de la fig. 9 correspond à la valeur moyenne de l'état HRS dans un régime de tension négative après RESET, tandis que  $R_{ON}$  est donné par la moyenne de toutes les mesures quasi-statique de chaque balayage, où le courant de contrôle est atteint. Fig. 9 ne révèle pas de dépendance de  $R_{OFF}$  ni  $R_{ON}$  sur le rayon de courbure excédant la variation statistique de la commutation de résistance.  $R_{OFF}$  a une valeur moyenne sur tous les rayons de courbure de  $(2.7 \pm 1.9) \cdot 10^7 \Omega$  tandis que  $R_{ON}$ ,  $(4.8 \pm 1.8) \cdot 10^4 \Omega$ . La variation est attribuée à la nature stochastique de la commutation avec une contribution aléatoire causée par le système qui ne contient qu'un nombre limité d'atomes [19]. L'influence de la flexion sur la résistance des électrodes est négligeable comparé à ces variations stochastiques causées par le processus de commutation. La cellule mémoire sur substrat de  $125 \mu\text{m}$  d'épaisseur peut être courbée avec un rayon minimum de  $2 \text{ mm}$  pour les déformations compressives aussi bien que tensile sans démontrer de dégradation de ses caractéristiques de commutation.  $2 \text{ mm}$  est le rayon de courbure minimum qui peut être atteint avec le système pivoter-et-plier pour une distance entre les pinces  $L = 8 \text{ mm}$  et un angle de courbure  $\beta = 108^\circ$ . Un rayon de courbure inférieur pourrait être obtenu en diminuant  $L$ , ou en augmentant  $\beta$ . Il est impossible de diminuer  $L$ , car les cellules mémoires et ses contacts doivent pouvoir tenir entre les pinces. D'autre part, les pinces entrent en contact les unes avec les autres pour des  $\beta$  plus élevés. Cependant, un rayon de courbe de  $2 \text{ mm}$  sur une feuille de substrat de  $125 \mu\text{m}$  d'épaisseur doit exercer une déformation de  $3.1 \%$ . Une feuille plus mince avec une épaisseur de  $25 \mu\text{m}$  peut être courbée avec un rayon de  $0.4 \text{ mm}$  avant d'atteindre  $3.1 \%$ . C'est pourquoi nous sommes confiants que nos cellules mémoires imprimées peuvent être courbées bien au-dessous de  $1 \text{ mm}$  sur des substrats minces, bien que nous ne soyons pas en mesure de le démontrer à travers des mesures in-situ.

La flexion statique induit des changements réversibles dans les structures imprimées, où les changements de résistance des structures imprimées dans l'état courbé retournent à leur état initial après relaxation. Une flexion cyclique par contre suit les changements irréversibles causé par des cycles de flexions répétitifs. C'est pourquoi le paramètre étudié, par exemple la résistance du dispositif, est toujours mesurée dans l'état non courbé entre les cycles de flexion consécutifs pour un rayon de courbure spécifique.

Contrairement aux expériences précédentes, nous n'utilisons pas de fils soudés en guise de contact pour des mesures in situ, mais au lieu, nous mesurons les cellules à l'extérieur du système pivoter-et-plier dans une station de mesures à deux pointes. Ceci est dû au fait que les connexions soudées ne peuvent pas supporter autant de cycles de flexion. Tout comme pour la flexion statique des cellules mémoires, nous étudions uniquement la flexion menant à une déformation des électrodes inférieures d'Ag au cours des expériences de flexion cyclique.

Afin de simuler les contraintes opérationnelles élevées, nous exécutons des cycles de flexion avec

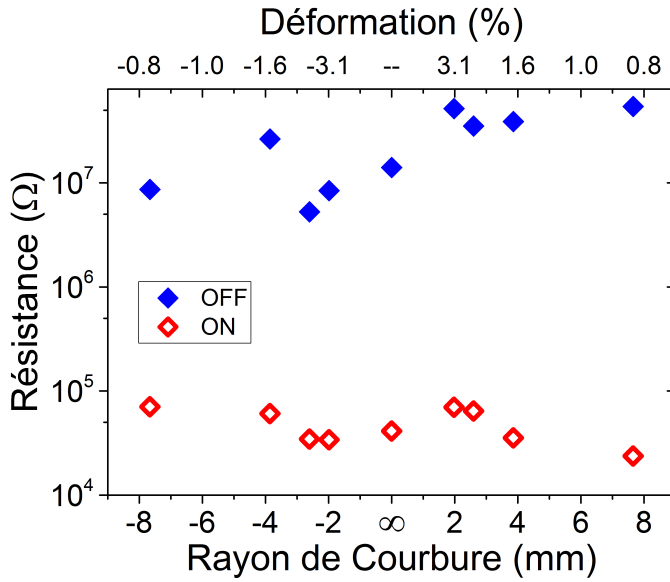


Figure 9: Flexion statique dans toutes les directions d'une cellule Ag/SOG/PEDOT:PSS imprimée sur une feuille PEN de  $125\ \mu\text{m}$  mesurée à l'aide de notre système pivoter-et-plier. Un rayon de courbure négatif indique une déformation compressive, tandis qu'un rayon de courbure infini correspond aux conditions non-courbées. L'échantillon supporte un rayon de courbure de  $\pm 2\ \text{mm}$  exerçant une déformation de  $\pm 3.1\ \%$  pour les distorsions tensiles aussi bien que compressives.

un rayon de courbure minimum de 3 mm pour les déformations compressives et tensiles. Ainsi,  $L$  est fixé à 10 mm et  $\beta = \pm 90^\circ$ . Nous utilisons un substrat feuille PEN avec une épaisseur de 50  $\mu\text{m}$  exerçant une déformation maximale de 0.8 % pour  $r = 3\ \text{mm}$ .

Fig. 10 présente les résultats des tests de flexion cyclique obtenus sur une cellule mémoire complète.  $R_{\text{OFF}}$  et  $R_{\text{ON}}$  sont extraits de balayages en tension quasi-statique allant de 0 V à 4 V, à -0.3 V, puis à 0 V avec un pas de 0.01 V et un courant de contrôle de 2  $\mu\text{A}$ . Nous atteignons plus de 500,000 cycles de flexion complets sans défaillance pour un substrat de 50  $\mu\text{m}$  d'épaisseur. Nous avons arrêté l'expérience avec 500,000 cycles car une telle endurance est suffisante pour la plupart des applications.

### Plasticité synaptique dans les mémoires métallisées électrochimiques pour l'informatique neuromorphique

Le domaine en plein essor de l'informatique neuromorphique dépend de synapses artificielles, c'est-à-dire de la plasticité synaptique des cellules mémoires. Jusqu'à présent, les ANN standards s'appuient sur l'architecture mémoire binaire, ce qui est extrêmement inefficace. C'est pourquoi nous étudions le potentiel de nos cellules ECM pour les synapses artificielles.

STDP est le principe de fonctionnement de base qui gouverne l'apprentissage synaptique dans les sous-groupes informatiques SNN plus performants. Cette section évalue donc en détail l'influence de l'amplitude du potentiel d'action ainsi que celui de la résistance initiale  $R_{\text{init}}$  sur la fonction STDP  $\frac{\Delta R}{R_0}(\Delta t)$ . Notre but est de mieux comprendre comment le processus d'apprentissage

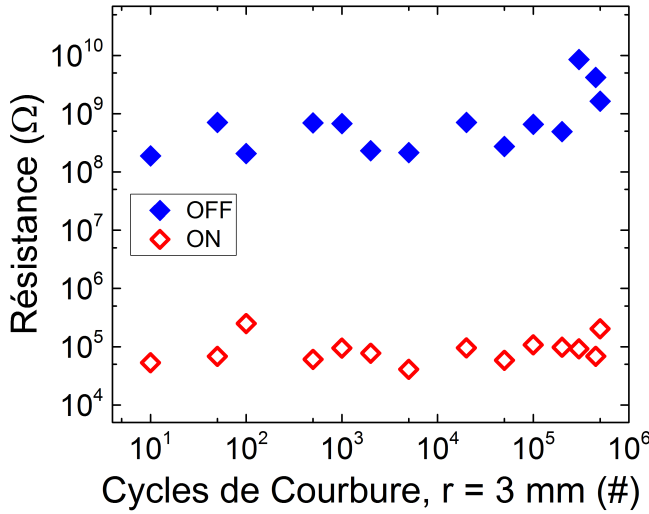


Figure 10: Flexion cyclique des cellules nanoparticules d’Ag/SOG/PEDOT:PSS pour une épaisseur de substrat PEN de 50  $\mu\text{m}$  et un rayon de courbure de 3 mm. Plus de 500,000 cycles de flexion peuvent être atteints

dépend de ces paramètres, qui peuvent être contrôlés directement (potentiel d’action) ou indirectement ( $R_{\text{init}}$ ). Cette compréhension nous permet d’adapter le processus d’apprentissage d’une synapse isolée ou d’un SNN complet pour répondre aux exigences d’une application spécifique. Par exemple, la force qu’une synapse doit avoir pour réagir à un stimulus entrant peut varier en fonction des applications. La force du processus d’apprentissage synaptique prospère dans un réseau neuronal complet. Toutefois, puisque nous investiguons le principe de fonctionnement de base de la plasticité de synapses individuelles, nous travaillons avec des cellules ECM dans le cadre des expériences STDP. Les résultats des cellules individuelles peuvent être appliqués directement aux réseaux neuronaux intégrés.

Le mécanisme d’STDP est expliqué dans la section : la fonction STPD  $\frac{\Delta R}{R_0}(\Delta t)$  dépend de l’intervalle de temps  $\Delta t$  entre les impulsions pré- et post-synaptiques. En pratique, il est donné par :

$$\frac{\Delta R}{R_0}(\Delta t) = \frac{R_{\text{after}}(\Delta t) - R_{\text{before}}(\Delta t)}{\min(R_{\text{before}}(\Delta t), R_{\text{after}}(\Delta t))} \quad (1)$$

où  $R_{\text{before}}$  and  $R_{\text{after}}$  sont les résistances de lecture de la cellule avant et après qu’une superposition des impulsions pré- et post-synaptiques soit appliquée sur la cellule. Afin d’effectuer une mise à l’échelle du dénominateur, nous comparons  $R_{\text{before}}$  and  $R_{\text{after}}$  avant d’utiliser la plus petite valeur ( $\min(R_{\text{before}}(\Delta t), R_{\text{after}}(\Delta t))$ ). Dans la littérature,  $R_{\text{before}}$  est souvent utilisé comme facteur d’échelle, bien qu’il fausse la fonction STDP et cause une sous-représentation de la branche exponentielle pour les  $\Delta t$  positifs. Pour notre polarisation définie, un  $\Delta t$  positif mène à un SET graduel, et donc un  $\frac{\Delta R}{R_0}$  négatif. Un RESET graduel pour un  $\Delta t$  négatif engendre un  $\frac{\Delta R}{R_0}$  positif.

Fig. 11 présente une fonction STDP mesurée sur une cellule mémoire Ag/SOG/PEDOT:PSS

stimulée à l'aide d'impulsions pré- et post-synaptiques telles que décrites dans la Fig. 3 avec une branche exponentielle où  $V(t) = \pm 3 \text{ V} \cdot e^{\mp 0.38 \frac{t}{\text{ms}}}$ . La fonction STDP est ajustée avec les équations suivantes [122]:

$$\begin{aligned}\frac{\Delta R}{R_0}(\Delta t) &= A_+ e^{\frac{\Delta t}{\tau_+}} \quad \text{for } \Delta t > 0 \\ \frac{\Delta R}{R_0}(\Delta t) &= A_- e^{\frac{\Delta t}{\tau_-}} \quad \text{for } \Delta t < 0\end{aligned}\quad (2)$$

à travers les deux facteur d'échelle linéaires  $A_+$ ,  $A_-$ , et les deux paramètres exponentiels  $\tau_+$ ,  $\tau_-$ . Ces paramètres peuvent être utilisés pour analyser de façon quantitative les fonctions STDP.  $A_+$  et  $A_-$  décrivent le changement de résistance maximum et ainsi la vitesse à laquelle le processus d'apprentissage à lieu, c'est-à-dire à quel point la résistance varie pour un stimulus externe donné.  $A_+$  correspond à un processus SET graduel et un renforcement de la connexion synaptique, tandis qu' $A_-$  décrit le processus RESET graduel et l'affaiblissement de la synapse.  $\tau_+$  et  $\tau_-$  indiquent comment le changement de résistance d'une mesure STDP unique dépend de l'intervalle de temps  $\Delta t$ .

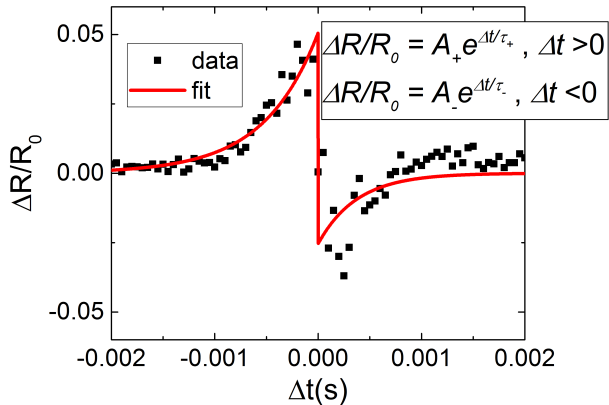


Figure 11: Une fonction STDP générée par des impulsions de tension exponentielles peut être ajustée avec deux fonction exponentielles pour  $\Delta t < 0$  et  $\Delta t > 0$ . Le modèle donne les deux paramètres d'échelle  $A_+$ ,  $A_-$ , ainsi que les deux paramètres exponentiels  $\tau_+$ ,  $\tau_-$ .

Fig. 12 dépeint l'influence de la résistance initiale de la cellule  $R_{\text{init}}$  sur le processus d'apprentissage de la cellule. Pour ce faire,  $R_{\text{init}}$  est mesuré juste avant le début de chaque mesure de fonction STDP. Nous varions  $R_{\text{init}}$  de 2 kΩ à 120 kΩ en commutant graduellement les cellules avec des pulses de tension appropriées. La mesure de chaque fonction STDP utilise les mêmes impulsions pré- et post-synaptiques pour une durée totale de 4 ms et une tension maximale de 2 V. L'influence de  $R_{\text{init}}$  sur les facteurs d'échelle  $A_+$  et  $A_-$  présentée dans la fig. 12(a) décrit une tendance claire. Un  $R_{\text{init}}$  plus élevé conduit à de plus hautes valeurs absolues d' $A_+$  et  $A_-$  et cause un changement relatif de résistance supérieur pour un stimulus externe. La fig. 12(b) démontre que les paramètres exponentiels  $\tau_+$  et  $\tau_-$  sont indépendants de  $R_{\text{init}}$ . En effet, ils dépendent fort probablement de la longueur des impulsions appliquées.

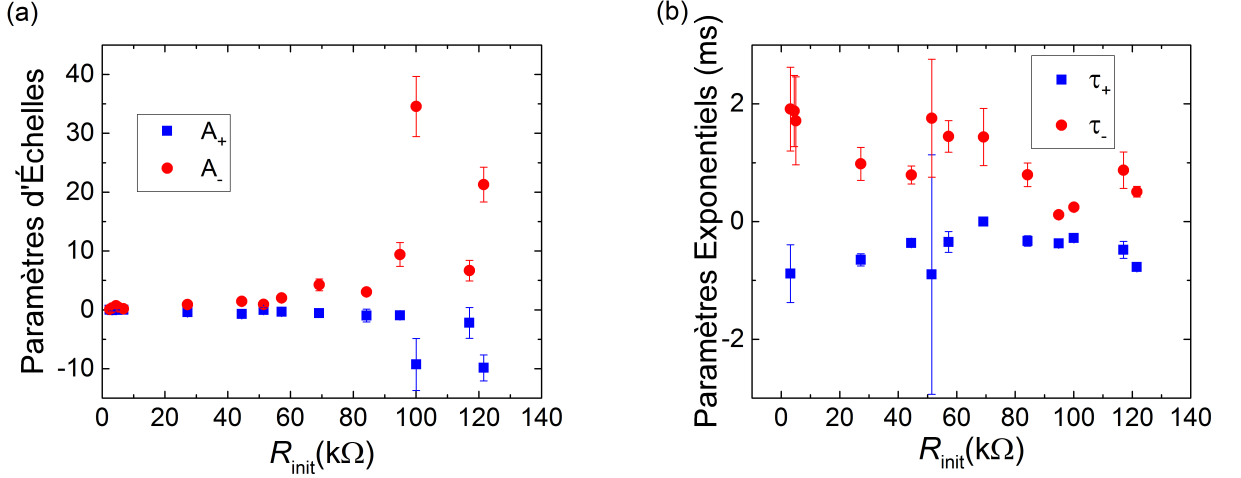


Figure 12: (a) Facteurs d'échelle linéaires  $A_+$ ,  $A_-$ , et (b) paramètres exponentiels  $\tau_+$ ,  $\tau_-$  en fonction de  $R_{\text{init}}$ , la résistance initiale de la cellule avant la mesure STDP. Chaque paire de points  $A_+$ ,  $A_-$ , et  $\tau_+$ ,  $\tau_-$  correspond à une fonction STDP. Les barres d'erreur dépeignent l'erreur sur l'ajustement et correspondent au bruit de la fonction STDP.

Fig. 13 présente l'influence de l'amplitude de la tension des potentiels d'action pré- et post-synaptiques sur les paramètres d'ajustement de la fonction STDP d'une cellule imprimée Ag/SOG/PEDOT:PSS. Les impulsions exponentielles sont similaires à celles utilisées dans les mesures STDP illustrées dans la fig. 11 pour une durée totale de 4 ms et une tension maximale variable. Les paramètres d'échelle linéaires  $A_+$  et  $A_-$  en fonction de la tension maximale des impulsions est présentée dans la fig. 13(a). Entre 1 V et 2 V,  $A_+$  et  $A_-$ , et donc le changement relatif de résistance de la fonction STDP correspondante, sont négligeables, car la tension cumulée des impulsions pré- et post-synaptiques n'excède pas le seuil de tension de commutation de la cellule mémoire. Entre 2 V et 3.2 V, une augmentation de la tension appliquée engendre aussi une hausse en valeur absolue d' $A_+$  et  $A_-$ . Ici, la tension cumulée donnée par la superposition des impulsions pré- et post-synaptiques, qui est presque le double de la valeur maximale de l'amplitude des impulsions individuelles pour les faibles  $\Delta t$ , suffit à déclencher un changement de résistance considérable. Le changement de résistance dépend de la tension maximale cumulée des impulsions, et ainsi  $A_+$  et  $A_-$  varient avec la tension maximale. Une impulsion supérieure à 3.2 V est trop élevée pour générer des fonctions STDP exploitables, car elle laisserait la cellule mémoire dans un état de faible résistance avec un état ON à peine réversible. Les paramètres exponentiels  $\tau_+$  et  $\tau_-$  présentés dans la fig. 13(b) sont sujets au bruit de mesure et ne démontrent aucune dépendance sur l'impulsion.

Pour conclure, l'analyse quantitative des fonctions STDP avec les paramètres  $A_+$ ,  $A_-$ , et  $\tau_+$ ,  $\tau_-$ , donne une information importante quant à l'influence des paramètres internes ( $R_{\text{init}}$  de la cellule) et externes (maximum des impulsions) sur la plasticité synaptique. Plus particulièrement, les facteurs d'échelle linéaire  $A_+$  et  $A_-$  démontrent une forte dépendance sur  $R_{\text{init}}$  et la tension d'impulsion.  $A_+$  et  $A_-$  sont corrélés au changement relatif de la résistance de la cellule

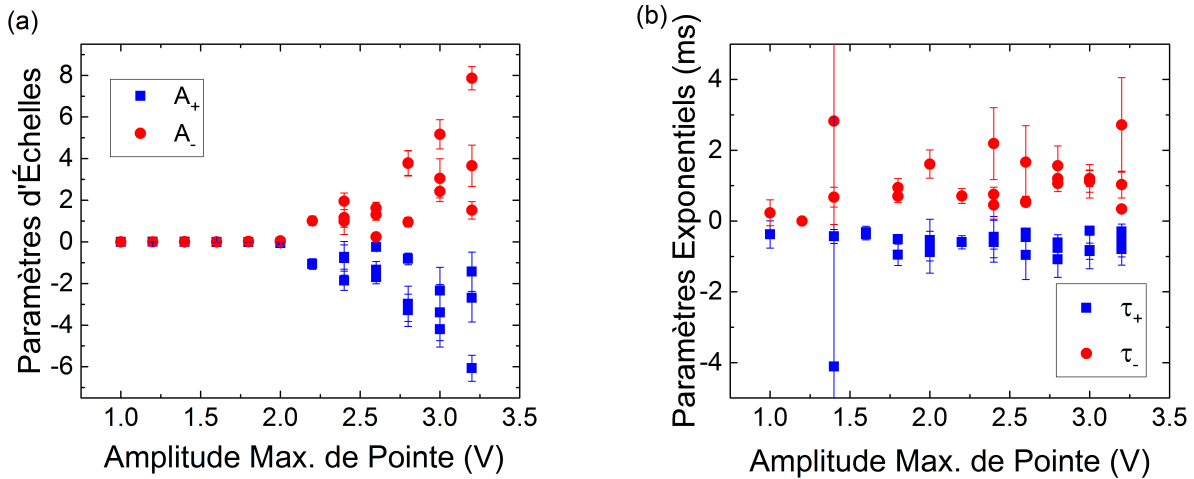


Figure 13: (a) Facteurs d'échelle linéaires  $A_+$ ,  $A_-$ , et (b) paramètres exponentiels  $\tau_+$ ,  $\tau_-$  en fonction de la tension maximale des impulsions pré- et post-synaptiques, la résistance initiale de la cellule avant la mesure STDP. Chaque paire de points  $A_+$ ,  $A_-$ , et  $\tau_+$ ,  $\tau_-$  correspond à une fonction STDP. Les barres d'erreur correspondent à l'erreur sur l'ajustement. (a) Les tensions en-dessous du seuil de 2 V sont trop faibles pour enclencher un changement significatif de la résistance et mènent à des  $A_+$  et  $A_-$  négligeables. Au-dessus de ce seuil de tension,  $A_+$  et  $A_-$  augmentent avec la tension. (b)  $\tau_+$  et  $\tau_-$  sont indépendants de la tension.

pour un stimulus externe et déterminent ainsi la vitesse d'apprentissage, c'est-à-dire comment de multiples impulsions de tension sont nécessaires pour suffisamment programmer une synapse avec une valeur de résistance spécifique.

Si nous voulons travailler avec un ANN spécifique, il est avantageux de connaître cette "vitesse d'apprentissage" des synapses individuelles, puisqu'elle détermine la vitesse à laquelle l'ANN réagit à des jeux de données d'entraînement, ainsi que sa stabilité dans les configurations d'entraînement. Ainsi, il est possible d'adapter les impulsions appliquées à des applications spécifiques. Par exemple, si l'application inclue une quantité de données très élevée, les impulsions de tension appliquées peuvent être réduites pour apprendre de façon ralenti, mais constante. Si seulement un petit jeu de données est disponible, des impulsions de tension élevées pourraient enclencher un apprentissage plus rapide.

## Résumé et perspectives

Cette thèse présente les premières cellules ECM complètement imprimées par jet d'encre. Alors que l'électronique flexible ne possède pas encore la mémoire imprimée appropriée pour les nombreuses applications dans le cadre de l'"Internet des objets", nos mémoires complètement imprimées ont les potentiels de combler ce vide. Les paramètres des dispositifs tels qu'un rendement de 80 %, une endurance de plus de 1100 cycles de commutation, et une rétention de  $8.65 \cdot 10^5$  s peuvent déjà répondre aux demandes dans le domaine de l'électronique imprimé. Dans le but de développer des cellules mémoires pour différentes applications, nous proposons différentes struc-

tures de cellules pour s'adapter aux demandes spécifiques des nombreuses applications possibles :

- Les cellules nanoparticules d'Ag/SOG/PEDOT:PSS démontrent l'endurance et la rétention la plus élevée ainsi qu'une excellente flexibilité
- Les cellules PEDOT : PSS/couche d'amorce de nanoparticules d'Ag/SOG/PEDOT:PSS dénotent un degré de transparence élevé pour des applications dans le domaine de l'électronique transparente. Cependant, ce concept reste limité par une faible endurance
- Une autre approche pour les dispositifs transparents réside dans les cellules nanofils d'Ag/SOG/PEDOT:PSS, qui ont le potentiel d'atteindre une flexibilité encore plus élevée
- Les cellules nanoparticules d'Ag/WO<sub>3</sub>/PEDOT : PSS utilisent des nanoparticules de WO<sub>3</sub> sans frittage en tant que couche isolante et peuvent ainsi servir comme des candidats potentiels dans les cellules mémoires complètement sans-frittage

La commutation locale par CAFM ainsi que les mesures MEB-FIB subséquentes prouvent la nature filamentaire de la commutation et confirment le mécanisme théorique de la commutation. Un modèle de diffusion basé sur la diffusion Fick a été établi pour modéliser la diffusion radiale du filament d'Ag, le mécanisme sous-jacent qui détermine la rétention de l'état ON. Le modèle est capable de décrire de façon quantitative le processus de diffusion et peut être utilisé dans une analyse de prédition de la rétention.

Des investigations de la flexibilité mécanique des cellules mémoires sont effectuées avec un système de flexion fait-maison pivoter-et-plier. Nous appliquons des cycles de flexion statiques ainsi que répétés sur les électrodes individuelles et les cellules ECM compétentes. Les expériences de flexion démontrent l'excellente flexibilité des cellules avec une commutation stable pour un rayon de courbure allant jusqu'à 2 mm pour une flexion statique, et 500,000 cycles de flexion avec un rayon de 3 mm pour une flexion cyclique.

Les mesures STDP indiquent que nos cellules mémoires imprimées peuvent être utilisées comme des synapses artificielles pour une implémentation directe ANN. Nous étudions le processus d'apprentissage et la façon dont nous pouvons directement influencer la vitesse d'apprentissage. Ces trouvailles peuvent être transférées à l'entraînement d'ANN imprimés.

Ce travail établi le processus d'impression pour différentes structures de cellules ECM avec des applications spécifiques, mais laisse la place à des optimisations, tout en apportant des réponses à plusieurs questions jusqu'alors ouvertes.

Le talon d'Achille que reste la rétention impossible à démontrée de nos ECM non-volatiles pourrait être amélioré en réduisant la constante de diffusion de l'Ag dans le matériau isolant. Pour le SOG, ceci pourrait être accompli avec différents protocoles de frittage, ou bien en changeant le type de SOG. Possiblement, un SOG à base de silicate combiné à des températures de frittage plus élevées pourrait donner des plus hautes rétentions.

En ce qui concerne les applications spécifiques, la prochaine étape serait le transfert d'une cellule

individuelle à un agencement crossbar. Ainsi, le problème de *sneak path* pourra être évalué et, si nécessaire, des dispositifs sélecteurs pourraient être ajoutés. De plus, des crossbars d'ECM complètement imprimés pourraient directement implémenter les ANN et mettre en action nos découvertes concernant l'ajustement du processus d'apprentissage

# Contents

<b>Acknowledgements</b>	<b>xxxii</b>
<b>List of Figures</b>	<b>xxxiii</b>
<b>List of Abbreviations</b>	<b>xxxvii</b>
<b>1 Introduction</b>	<b>1</b>
<b>2 Fundamentals</b>	<b>3</b>
2.1 Types of Resistive Random Access Memory . . . . .	3
2.2 State-of-the-Art of Printed Memory . . . . .	5
2.3 Resistive Switching . . . . .	7
2.3.1 Switching Mechanism of Electrochemical Metallization Memory . . . . .	7
2.3.2 Electrode and Solid Electrolyte Materials . . . . .	10
2.3.3 Failure Mechanisms . . . . .	13
2.3.4 Resistive Memory for Neuromorphic Computing . . . . .	14
2.4 Bending Theory . . . . .	19
<b>3 Methods</b>	<b>21</b>
3.1 Fabrication . . . . .	21
3.1.1 Inkjet Printing . . . . .	21
3.1.2 Sintering . . . . .	23
3.1.3 Memory Cell Layout . . . . .	24
3.2 Analysis . . . . .	26
3.2.1 Conductive Atomic Force Microscopy . . . . .	26
3.2.2 Focused Ion Beam Scanning Electron Microscopy . . . . .	27
3.2.3 Electrical Characterization . . . . .	27
3.2.4 Mechanical Characterization . . . . .	28
<b>4 Results and Discussion</b>	<b>33</b>
4.1 Resistive Switching in Printed Ag/SOG/PEDOT:PSS cells . . . . .	33
4.1.1 Spin-on-glass Characterization . . . . .	34
4.1.2 Quasi-Static Electrical Characterization . . . . .	35

4.1.3	Local Filament Formation with Conductive Atomic Force Microscopy . . . . .	38
4.1.4	Retention Analysis . . . . .	43
4.1.5	Summary and Discussion . . . . .	46
4.2	Transparent Memory Cells . . . . .	46
4.2.1	Ag Nanoparticle Seed Layer . . . . .	47
4.2.2	Ag Nanowire Active Electrode . . . . .	49
4.2.3	Summary and Discussion . . . . .	52
4.3	Resistive Switching in Printed Ag/WO <sub>3</sub> /PEDOT:PSS cells . . . . .	53
4.3.1	Quasi-Static Electrical Characterization . . . . .	53
4.3.2	Local Filament Formation with Conductive Atomic Force Microscopy . . . . .	55
4.3.3	Retention Analysis . . . . .	57
4.4	Mechanical Characterization for Flexible Applications . . . . .	58
4.4.1	Static Bending . . . . .	59
4.4.2	Cyclic Bending . . . . .	63
4.4.3	Summary and Discussion . . . . .	69
4.5	Synaptic Plasticity for Neuromorphic Computing . . . . .	69
4.5.1	Implementation of Long- and Short-Term Memory . . . . .	69
4.5.2	Spike-Timing-Dependent Plasticity . . . . .	71
4.5.3	Summary and Discussion . . . . .	76
<b>5</b>	<b>Summary and Outlook</b>	<b>77</b>
<b>A</b>	<b>Fabrication Parameters</b>	<b>79</b>
<b>B</b>	<b>Waveforms for Inkjet Inks</b>	<b>83</b>
<b>C</b>	<b>Normalization of Spike-Timing-Dependent Plasticity Function</b>	<b>87</b>
<b>D</b>	<b>Publications and Conference Contributions</b>	<b>89</b>
	<b>Bibliography</b>	<b>90</b>

# Acknowledgements

First of all, I would like to express my gratitude to my supervisor Prof. Andreas Ruediger and my co-supervisor Prof. Christina Schindler. Within the framework of their fruitful collaboration they gave me the opportunity to work in the exciting field of printed resistive memory. I want to thank Prof. Andreas Ruediger for many encouraging discussions and all his effort to make my stay in Montréal a very enjoyable one. I thank Prof. Christina Schindler for the constant support and her always open door in Munich. The two of you make up the perfect supervising team - I will always keep the last three years in good memory.

I am also indebted to Prof. Shuhui Sun, Prof. Matthew Dawber, and Prof. Alfred Kersch for their invested time and effort as part of the jury committee.

Many thanks go to Michael Kaiser for all his technical support and providing such a good atmosphere in the lab.

Thanks to Dr. Gitanjali Kolhatkar, Dr. Fabian Ambriz-Vargas, Dr. Julien Plathier, and Angel Valdez in Montréal for their help and all the good times we had. Special thanks to Gitanjali for her great support with the French translation of this thesis.

I want to thank the Bachelor and Master students working at the Laboratory for Microsystems Technology in Munich and contributing in various ways to this thesis. Thanks to Jakob Schober, Patrick Popp, Marc Kracklauer, Andrea Kreuzer, Evi Linkerhaegner, Sophia Zeiger, Theresa Schuelein, Sebastian Pschierer, Julian Stark, Sandra Thalmair, Alexandra Bednar, and Joshua Brauns.

For the SEM measurements and FIB cross-sections I want to thank Dr. Constanze Eulenkamp. Viktorija Juhart and Alexander Sindjelic deserve thanks for the viscosity and surface tension measurements.

To all my friends, my family, and especially to my wife, Magdalena: thank you for your immeasurable support and making it possible that I can write these lines today.



# List of Figures

2.1	Classification of different RAM technologies . . . . .	5
2.2	Bipolar resistive switching . . . . .	8
2.3	Schematic of multi bit data storage . . . . .	9
2.4	Methylsiloxane spin-on-glass . . . . .	11
2.5	Neuromorphic Computing - implementation of an ECM cell as artificial synapse .	15
2.6	Neuromorphic Computing - Spike-Timing-Dependent Plasticity . . . . .	16
2.7	Schematic of an Artificial Neural Network . . . . .	18
2.8	Substrate under bending . . . . .	19
3.1	Schematic of droplet generation during inkjet printing . . . . .	21
3.2	Sintering of printed silver nanoparticles . . . . .	24
3.3	Crossbar array with sneak path issue . . . . .	25
3.4	Photograph of printed memory cells . . . . .	25
3.5	Principle of Atomic Force Microscopy . . . . .	26
3.6	Schematic of the rotate-to-bend apparatus . . . . .	29
3.7	Comparison between theoretical and experimentally determined bending radius .	30
4.1	SOG curing temperature plotted versus its refractive index and SET voltage . .	35
4.2	Resistive switching in an Ag/SOG/PEDOT:PSS cell structure . . . . .	36
4.3	Endurance of an Ag/SOG/PEDOT:PSS cell structure . . . . .	37
4.4	Quasi-static multi bit switching of an Ag/SOG/PEDOT:PSS cell structure . .	38
4.5	Schematic of the CAFM setup with current-voltage measurement . . . . .	39
4.6	CAFM area scans on an Ag/SOG layer stack before and after filament formation	40
4.7	Logo of the INRS and the Munich University of Applied Sciences consisting of switched Ag filaments . . . . .	41
4.8	FIBSEM cross section of Ag filament inscribed in SOG using CAFM . . . . .	42
4.9	ON resistance and retention time as a function of pulse width for pulsed switching in an Ag/SOG/PEDOT:PSS cell structure . . . . .	44
4.10	ON resistance as a function of time in an Ag/SOG/PEDOT:PSS cell structure: diffusion of the silver filament . . . . .	45
4.11	Schematic of PEDOT:PSS/Ag nanoparticle seed layer/SOG/PEDOT:PSS cell structure . . . . .	47

4.12 Resistive switching in a transparent PEDOT:PSS/Ag nanoparticle seed layer/SOG/PEDOT:PSS cell structure . . . . .	48
4.13 Transmittance of spin-coated layers of the PEDOT:PSS/Ag nanoparticle seed layer/SOG/PEDOT:PSS cell structure on glass substrate . . . . .	48
4.14 Printed Ag nanowire network . . . . .	49
4.15 Resistive switching in a transparent Ag nanowires/SOG/PEDOT:PSS cell structure . . . . .	50
4.16 Disintegration of Ag nanowires during SET with CAFM . . . . .	51
4.17 Transmittance of spin-coated Ag nanowires/SOG/PEDOT:PSS cell structure on glass substrate . . . . .	52
4.18 Resistive switching in an Ag/WO <sub>3</sub> /PEDOT:PSS cell structure . . . . .	54
4.19 Higher amount of leakage current in Ag/WO <sub>3</sub> /PEDOT:PSS cells leads to lower degree of multi bit data storage . . . . .	54
4.20 CAFM area scans on an Ag/WO <sub>3</sub> layer stack before and after filament formation . . . . .	55
4.21 FIBSEM cross section of Ag filaments inscribed in WO <sub>3</sub> using CAFM . . . . .	57
4.22 ON resistance as a function of time in an Ag/WO <sub>3</sub> /PEDOT:PSS cell structure: diffusion of the silver filament . . . . .	58
4.23 Static bending of a printed Ag nanoparticle line on PEN substrates with different thicknesses . . . . .	60
4.24 Static bending of a printed PEDOT:PSS line on PEN substrates with different thicknesses . . . . .	60
4.25 Static bending of an Ag nanoparticle/SOG/PEDOT:PSS cell in both direction exerting tensile as well as compressive strain . . . . .	62
4.26 Cyclic bending of a printed Ag nanoparticle line in either tensile or compressive direction . . . . .	63
4.27 Cyclic bending of printed electrode lines in both tensile or compressive direction . . . . .	64
4.28 Morphological comparison of printed lines of Ag nanoparticles and nanowires after cyclic bending . . . . .	66
4.29 Cyclic bending of complete memory cells with Ag nanoparticle and nanowire bottom electrodes for different substrate thickness . . . . .	67
4.30 Cracks formed in an Ag nanoparticle/SOG/PEDOT:PSS cell after 1000 bending cycles leading to failure . . . . .	68
4.31 Implementation of long and short term memory in an Ag/WO <sub>3</sub> /PEDOT:PSS cell . . . . .	70
4.32 STDP of a printed Ag/SOG/PEDOT:PSS cell with triangular and exponential voltage spikes . . . . .	72
4.33 Fit of STDP function of a printed Ag/SOG/PEDOT:PSS cell with exponential voltage spikes . . . . .	73
4.34 Fitting parameters of STDP function plotted versus the initial cell resistance . . . . .	74
4.35 Fitting parameters of STDP function plotted versus the maximum voltage of pre- and post-synaptic voltage spikes . . . . .	75
B.1 Waveform for Ag nanoparticle ink . . . . .	83

B.2	Waveform for Ag nanowire ink . . . . .	84
B.3	Waveform for SOG and WO <sub>3</sub> ink . . . . .	84
B.4	Waveform for PEDOT:PSS ink . . . . .	85
C.1	STDP function for $\min(R_{before}(\Delta t), R_{after}(\Delta t))$ and $R_{before}(\Delta t)$ as normalization parameter . . . . .	88
C.2	Fitting parameters of STDP function plotted versus the maximum voltage of pre- and post-synaptic voltage spikes for $\min(R_{before}(\Delta t), R_{after}(\Delta t))$ and $R_{before}(\Delta t)$ as normalization parameter . . . . .	88



# List of Abbreviations

AFM	Atomic Force Microscopy
ANN	Artificial Neural Network
CAFM	Conductive Atomic Force Microscopy
CMOS	Complementary Metal-Oxide Semiconductor
DRAM	Dynamic Random Access Memory
ECM	Electrochemical Metallization Memory
FeFET	Ferroelectric Field Effect Transistor
FeRAM	Ferroelectric Random Access Memory
FIB	Focused Ion Beam
FTJ	Ferroelectric Tunnel Junction
HRS	High Resistive State
LRS	Low Resistive State
MISFET	Metal Insulator Semiconductor Field Effect Transistor
MRAM	Magnetic Random Access Memory
PCM	Phase Change Memory
PEDOT:PSS	poly(3,4-ethylenedioxythiophene) polystyrene sulfonate
PEN	poly(ethylene 2,6-naphthalate)
PET	poly(ethylene terephthalate)
RAM	Random Access Memory
ReRAM	Resistive Random Access Memory
SEM	Scanning Electron Microscopy
SNN	Spiking Neural Network
SOG	Spin-on-glass
SRAM	Static Random Access Memory
STDP	Spike-Timing-Dependent-Plasticity
STT-RAM	Spin-Transfer Torque Random Access Memory
VCM	Valence Change Memory

# Chapter 1

## Introduction

Printed electronics is a rapidly growing segment with a market value of 5.6 billion USD in 2010 and already 26.9 billion USD in 2016 with an expected global growth rate of 13.9 % by the year 2020 [121]. This extremely rapid growth is caused by the various benefits of printed electronics compared to standard semiconductor technology [22]:

- Low production costs: a semiconductor fabrication plant requires a billion USD investment, while in principle printed electronics can be fabricated with a standard office inkjet printer [4]
- The additive printing process is not limited to wafer substrates but can utilize various foils or even paper as substrates
- On-demand printing offers an extremely versatile and customizable production
- Mechanical flexibility is provided by flexible substrates <sup>1</sup>

All of these advantages enable printed electronics to become one of the major technologies contributing to the "Internet of Things" in the framework of the "4<sup>th</sup> Industrial Revolution" [22]. One of the key enabler of the Internet of Things will be low-cost embedded systems, which allow for the detailed monitoring and controlling of production chains or tracking environmental parameters of smart packages [74]. These embedded systems have to track, store and ideally already process various types of data using sensors, electronic circuits, and data transmitters. The field of printed electronics possesses the necessary technological maturity for manufacturing most of the required components with printing techniques. Printed sensors for the acquisition of pressure, strain, temperature, humidity, and more have already been realized [64]. Contact-less data transfer is achieved with printed Radio-Frequency-Identification tags [60] and power supply of the embedded systems could be provided with printed batteries [40]. Various further circuit elements such as resistor, capacitor, and inductor [61] can be printed for the implementation of fully printed electronic circuits. Printed transistors have already been demonstrated in 1994

---

<sup>1</sup>A silicon chip can also feature a certain degree of flexibility when thinned to several  $\mu\text{m}$  and thus can be integrated in flexible electronics [113]. However, the other above mentioned advantages of printed electronics are then omitted and connections from the silicon chip to the substrate foil can be detrimental.

[41] and nowadays fully printed diodes with an operating frequency up to 1.6 GHz are available [115]. However, in order to fabricate fully printed circuits, every single circuit element has to be printable, including the memory unit. Until now, printed memory devices still lack technological maturity. In this regard, Resistive Random Access Memory (ReRAM) is particularly attractive for the printing process since it consists of a simple three-layered structure with a minimum unit cell size of  $4 F^2$ , where  $F$  is the minimum feature size given by the manufacturing process. The small unit cell size can partially compensate for the larger feature size of the printing process compared to thin film deposition combined with lithography.

Previous work on fully printed ReRAM devices mainly utilized the electrohydrodynamic printing method [5][111], which allows for higher printing resolution [66]. However, the higher complexity compared to standard inkjet printing could probably impede industrial upscaling. In 2015, Nau et al. presented the first fully inkjet-printed unipolar resistive memory, which only showed a yield lower than 20 % [100]. At present all other devices fabricated by standard inkjet printing require additional process steps such as lithographic structuring [134] or electroplating [142].[51] The goal of this thesis is to address the unresolved need for printed memory devices to complement low-cost printed system which will facilitate the "Internet of Things".

The thesis is structured as follows: after this introduction, chapter 2 gives an overview of the working principle of ReRAM, describes the material systems, and explains how ReRAM cells can be used for neuromorphic computing. Chapter 3 presents the main fabrication and analysis methods employed for manufacturing and investigation of the memory cells. The experimental results in chapter 4 include the switching characteristics for various material combinations, bending tests for flexible applications, and results of neuromorphic computing. Chapter 5 summarizes the findings of the thesis and gives an outlook on further improvements and future applications.

# Chapter 2

## Fundamentals

The main goal of this thesis is the fabrication of fully inkjet-printed resistive memory cells. Therefore, this chapter gives the reader necessary background information and basic theoretical fundamentals for a better understanding and interpretation of the experimental results. Firstly, different types of ReRAM technology are put in a bigger context and compared to both state-of-the-art memory as well as other prototypical and emerging memory technology. Secondly, the switching mechanism of electrochemical metallization memory (ECM), the sub-group of ReRAM used in this thesis, is illustrated in more detail. Then, the various materials making up the memory cells are described. Finally, a short overview of how bending creates strain in an object gives the theoretical background on the bending tests applied on the flexible memory cells.

### 2.1 Types of Resistive Random Access Memory

In a Random Access Memory (RAM) structure, the individual memory cells are organized in an array. The read and write times do not depend on the physical location of the memory cell in the array - therefore the name "random access". RAM can be divided into volatile and non-volatile memory. While non-volatile memory is able to retain stored data without power, volatile memory cannot store data for a longer time and therefore has to be refreshed periodically in order not to lose stored information. Fig. 2.1 shows a selected classification of different types of RAM. Nowadays, mostly static RAM (SRAM) and dynamic RAM (DRAM) are used as volatile memory. DRAM utilizes a capacitor structure and differentiates between two charge storage levels as the binary logic states. The unavoidable self-discharge of the capacitor causes the volatile nature of the memory. SRAM uses a flip-flop circuitry, where typically six transistors are needed to store one bit. In a modern personal computer, the faster SRAM is employed as cache memory, whereas DRAM typically makes up the main primary memory.[137]

The group of non-volatile memory comprises numerous different types of technology. As classification system the different technologies are grouped according to their technological maturity. "Baseline" memory is industrial standard, "prototypical" memories are already commercially available, but mostly for niche applications, and "emerging" memories have shown proof-of-

concept operation but still have to solve technological issues.

Flash, the most dominant non-volatile memory technology, uses a floating gate of a transistor structure for the storage of electrons and thus can distinguish between two logical states as presence or absence of electrons. Although it is the industrial standard for most storage class memory applications, it has shortcomings in endurance and write time.

Ferroelectric RAM (FeRAM) as one of the prototypical memories employs a ferroelectric insulator in a capacitor structure and can switch between two different polarizations to store binary information. It features high retention and endurance and fast read and write times. However, it is subjected to an intrinsic physical limit of scaling and therefore is a poor candidate for high density memory devices. Phase Change Memory (PCM) uses materials which can be thermally switched between an amorphous state and a crystalline state. The high resistance of the amorphous state and the low resistance of the crystalline state enable binary data storage. PCM is an advanced technology: the first PCM technology was released 2011 by Samsung [137, p.671]. On the other hand, the high current densities required for the phase transition lead to a high power consumption compared to alternative technology and can cause thermal crosstalk between adjacent cells, i.e. the high temperature during programming of one cell disturbs a neighboring cell [114]. Furthermore, PCM relies on rare materials such as Ge, Sb, and Te. In Magnetic RAM (MRAM), the tunneling probability of electrons depends on the relative magnetization of the ferromagnetic layers below and above a tunneling dielectric. Thus, the two magnetization states parallel and anti-parallel correspond to two logical states and can be characterized by the device resistance. MRAM suffers from a low OFF to ON ratio, which requires a sophisticated read-out circuitry [85]. Spin-Transfer-Torque-RAM (STT-RAM) uses spin-polarized electrons to switch the magnetization of the ferromagnetic layer. This allows for better scaling, i.e. higher memory density compared to MRAM, but STT-RAM still faces the disadvantage of a low OFF to ON ratio [63].

The group of emerging memory is the least mature concerning the technological level. However, all of the presented memory technologies have the potential to serve as a suitable universal memory if various technological obstacles can be solved. To provide a better overview, the focus lies on the most promising technologies. A more extensive description can be found in the 2017 report of the *International Roadmap for Devices and Systems* [1]. The Ferroelectric Field Effect Transistor (FeFET) consists of a Metal Insulator Semiconductor FET (MISFET) structure, whose gate dielectric is replaced by a ferroelectric layer. This enables a non-destructive read operation compared to the destructive read-out of FeRAM. Ferroelectric Tunnel Junctions (FTJs) use an ultra-thin ferroelectric layer sandwiched between two asymmetric electrodes as switchable tunneling barrier. The ferroelectric polarization (up or down) of the thin film modulates the barrier height and therefore also the tunneling current and its electric resistance. The group of ReRAM can be further divided into Valence Change Memory (VCM) and Electrochemical Metallization Memory (ECM). Both use a conductor-insulator-conductor sandwich structure, where the high resistive state (HRS) is the pristine state with the insulating layer acting as barrier and in the low resistive state (LRS) a conducting filament connects the two conducting electrodes. For VCM, this filament consists of oxygen vacancies in the oxide insulator, whereas ECM utilizes a metallic

filament. Both types of memory show high endurance, long retention times, high scalability, and low power switching. Typically, VCM features a larger endurance, while ECM has a larger resistance ratio between LRS and HRS. Both VCM and ECM require selector devices, when used in crossbar arrays (see 3.1.3). It is worth noticing that ECM is also often referred to as Conductive Bridge RAM (CBRAM) or Programmable Metallization Cell (PMC).[1][137]

All of the above presented non-volatile memories can feature multi level switching, i.e. they are able to store more than 2 bits per memory cell. However, two properties are essential for achieving a maximum amount of addressable bits per cell: reproducible and stable resistive states and a high ratio between the resistance values of ON and OFF state. MRAM technology has for example a too low OFF to ON ratio to achieve a high degree of multi level switching.

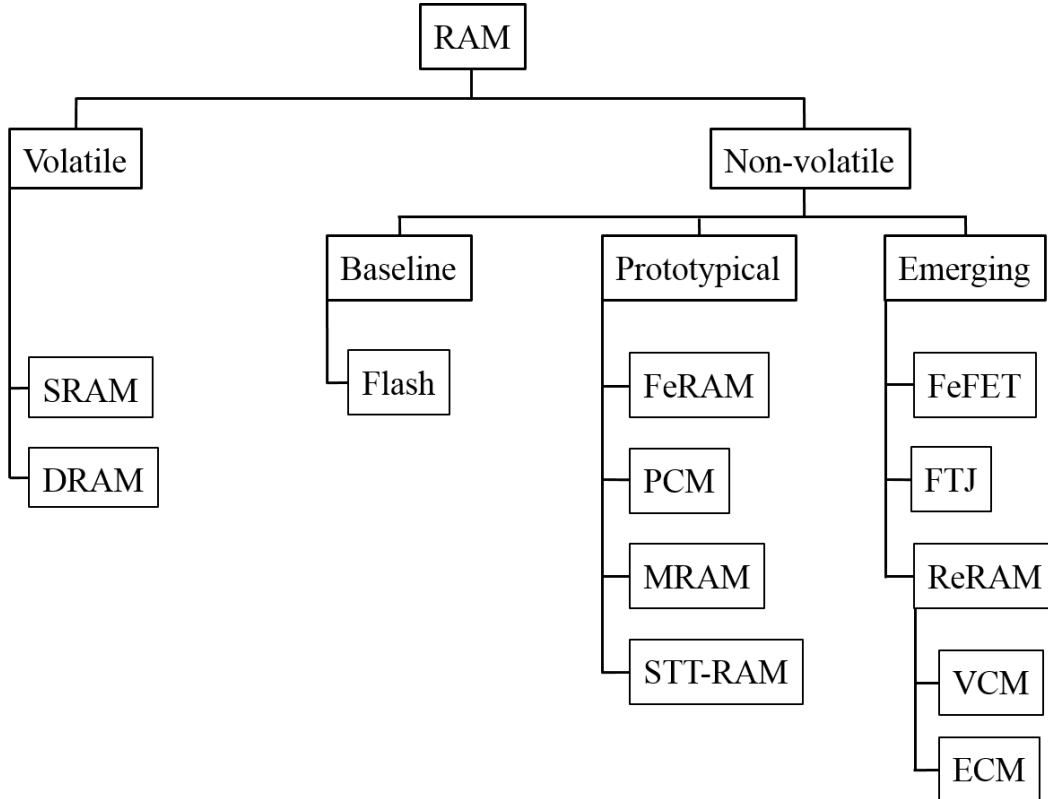


Figure 2.1: Classification of different RAM technologies showing only the most relevant types. Non-volatile RAM is categorized according to maturity of technology into baseline, prototypical, and emerging memory. Graph adapted from [1]

## 2.2 State-of-the-Art of Printed Memory

Due to its high growth rates, the field of printed electronics features vivid evolution and change. Until now, printed electronic devices mostly incorporate semiconductor chips as memory devices, but directly printed memory experiences considerable improvements. This section gives an overview on the state-of-the-art of printed non-volatile memory.

Flash as the most dominant memory based on semiconductor chips has been printed by using

organic materials [62]. However, the switching voltage of up to 50 V is too high to be driven by batteries in a self-sustaining device [62]. Printed PCM, MRAM, and STT-RAM have not yet been reported. For PCM, the printability of the phase change material combination Ge, Sb, and Te remains challenging. The performance of MRAM and STT-RAM relies on a thin tunnel barrier in the nm range, which is extremely difficult to achieve with printing technology. The same holds true for FTJs, where thin ferroelectric layers have already been spin-coated [87], but printed FTJs have not yet been reported. Ferroelectric polymers enable printing of FeRAM structures [82]. Their printed ferroelectric layer has to be thicker compared with evaporated layers to prevent short-circuits of the electrodes. Therefore, printed FeRAM also suffers from high switching voltages of approximately 20 V [82].

Due to its simple three-layered structure, ReRAM is particularly attractive for the printing process. In the last years, this has led to an increasing amount of publications on printed ReRAM devices. Research is conducted on various structures and material combinations and involves combinations of different printing methods as well as partially printed cells.

In 2014, Zou et al. reported on bipolar Ag/Cu/Cu<sub>x</sub>O/Ag ReRAM with printed Ag layers and electroplated Cu [142]. The cells' switching characteristics and flexibility are promising, but the electroplating step is a disruptive, time-limiting factor in the production process. In 2016, Vilmi et al. presented an inkjet-printed Ag/TiO<sub>x</sub>/Ag memory cell, which is already connected to a piezoelectric transducer to form a self-sustaining device [134]. This combination of a memory cell with an energy-harvesting sensor is highly innovative. However, the fabrication requires an additional lithography step and the cell is limited to few switching cycles before failure. Vescio et al. published their findings on Au/HfO<sub>2</sub>/Ag ReRAM cells, where the HfO<sub>2</sub> and Ag layers are inkjet-printed, while the Au bottom electrode still relies on sputtering in 2017 [132].

Fully printed ReRAM using electrohydrodynamic printing have been repeatedly reported by the Choi group of Jeju National University and focuses on unipolar Ag/insulator/Ag structures [5][26]. Being able to achieve a higher printing resolution, the more complex electrohydrodynamic printing method might be challenging to be used in a high-throughput industrial process. In 2017, Catenacci et al. used aerosol jetting to print ECM cells, where switching occurs through the SiO<sub>2</sub> shell of Cu-SiO<sub>2</sub> core-shell nanowire composites [21]. While showing promising device parameters, the random distribution of the nanowires enhances the cell-to-cell switching variation.

The first fully inkjet-printed ReRAM was reported in 2015 by Nau et al. as an Ag/poly(methyl methacrylate)/Ag structure [100]. The unipolar cells are already connected together with selector diodes to form a 5x5 crossbar. This structure shows as first feasibility test that ReRAM cells can be fabricated by inkjet-printing alone. However, the low yield of below 20 % calls for structural changes or improvements of the printing process.

All these works confirm the high interest in printed memory devices while also showing that further improvements are required prior to transition to industrial applications.

## 2.3 Resistive Switching

For every new memory technology the basic memory unit, also called memory cell, has to be switchable between the two logical states "0" and "1" to enable binary logic. "Resistive RAM" is a descriptive term, since the logical states are defined by the memory cell's resistance: a high resistance state (HRS) corresponds to "0" and a low resistance state (LRS) correlates to "1". This section describes the physical mechanisms of the switching process for ECM cells. In this framework, diffusion is an important phenomenon which determines the retention time, a benchmark parameter of a memory device. Therefore, we model for the radial diffusion of the metallic filament is implemented. Due to their aptitude for multi level switching, ECM cells are particularly attractive for the fast growing field of neuromorphic computing. Therefore, a motivation for neuromorphic applications is given and it is shown how ECM can be beneficially used in this context.

### 2.3.1 Switching Mechanism of Electrochemical Metallization Memory

An ECM cell consists of an insulating layer, which is sandwiched between two (often different) electron conductors as electrodes. The resistance between the two electrodes defines the logical state of the ECM cell and can be switched between at least two different resistance states (HRS and LRS) by applying appropriate voltages to the electrodes. Two different switching mechanisms have to be distinguished: bipolar and unipolar switching. Unipolar switching is independent of the voltage polarity and is not subject of this work. Bipolar switching appears in asymmetric cell structures and depends on the voltage polarity. Switching from HRS to LRS (SET process) and switching back to HRS (RESET process) only occurs for different polarity of the applied voltage.

For *bipolar* switching in ECM, one of the electrodes consists of an oxidable metal, e.g. Ag or Cu, whereas the other one is made of an electrochemically inert material, e.g. Pt or inert polymers. Although memories are switched and read out by pulses in devices, switching with a triangular, "quasi-static" voltage sweep reveals further information about the switching mechanism such as the switching voltages (see Fig. 2.2). When a voltage is applied between the two electrodes, where a positive active electrode is defined as positive bias, the current-voltage-diagram shows insignificant current for a low positive bias. This represents the initial HRS, which is dominated by thermionic emission or space charge limited current flow through the insulating layer (inset A) [25]. At a sufficiently high bias, atoms of the active electrode (here Ag) get oxidized and the positive Ag ions migrate to the negatively polarized inert electrode. There they get reduced and form an electrodeposit made of elemental Ag (inset B). Since the electric field is highest at this first electrodeposit, further electrodeposition continues at this starting point and results in a filamentary growth from the inert to the active electrode. When it reaches the active electrode, the cell switches to the LRS (inset C). During and after this SET process, an external current compliance limits the current flow in order to prevent excessive currents from damaging the cell. For the RESET process from HRS to LRS, the voltage has to be reversed, i.e. the active electrode has to be negatively charged. The filament dissolution of the RESET process is determined by the

high morphological asymmetry between the needle-shaped Ag filament and the active electrode [46]. At the interface between filament and insulator, electrochemical dissolution and redeposition of Ag occurs. At the thinnest part of the filament in contact with the active electrode, Joule heating strongly enhances this process, leading to Ostwald ripening and filament rupture [137, p.698]. Once the filament is initially ruptured, electrochemical processes and ion migration dissolve the filament again. The Ag atoms of the filament get oxidized again and the Ag ions migrate back to the now negatively polarized active electrode, where they get reduced (inset D). The RESET re-establishes the HRS by a complete or only partial dissolution of the filament with a remaining but disconnected filament.

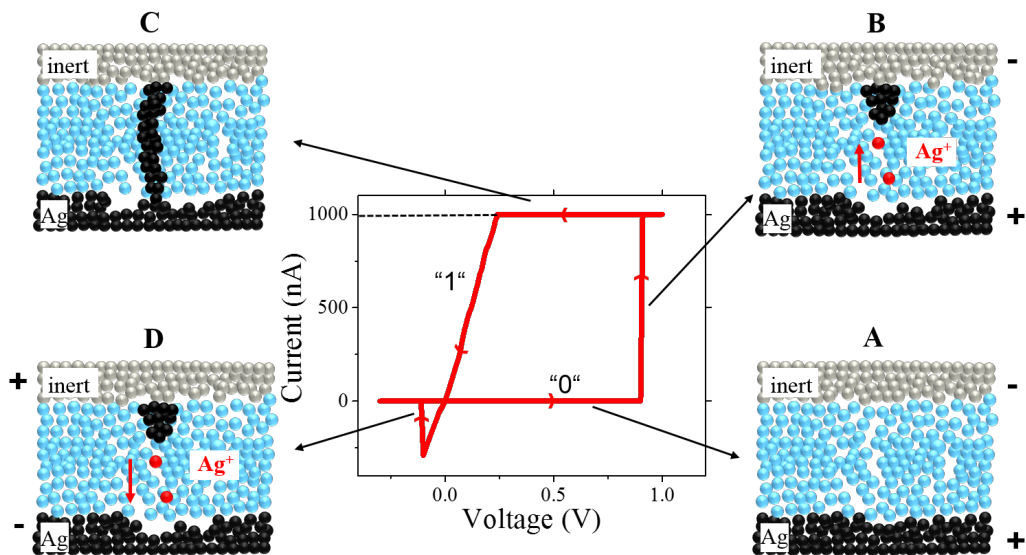


Figure 2.2: Bipolar switching of ECM memory: (A) high resistance OFF state, (B) filament growth, (C) low resistance ON state, (D) filament dissolution under reversed voltage. The middle inset shows corresponding current voltage characteristic with a SET voltage of approximately 0.9 V and a current compliance of  $1 \mu\text{A}$ . Adapted from [130]

*Unipolar* switching usually appears in symmetric cell structures with two active electrodes. The SET process is equivalent to the bipolar switching with the sole difference that switching is feasible for both voltage polarities in a symmetric cell structure. While a current compliance is used during the SET process, RESET happens without compliance and therefore at a high current in the micro- and milliampère range and low voltages compared to SET. Consequently, the filament rupture during RESET is caused by a thermal breakdown due to Joule heating. After the initial rupture, the filament dissolution due to the applied voltage takes place analogous to the bipolar RESET.

For both switching mechanisms, various materials were found to serve as suitable insulators, such as  $\text{Ag}_2\text{S}$ ,  $\text{ZnO}$ ,  $\text{SiO}_2$ ,  $\text{GeSe}$ , and polymers [59][68][116][140][97]. Most materials require an initial forming process for the first switching in a pristine cell. This so-called electroforming is a current-limited soft dielectric breakdown during the first SET process. The first filament

formation defines a structural template in the matrix of the insulator and ensures preferential filament growth for the subsequent switching cycles [137, p.697]. Therefore, for most materials, the first SET process requires a significantly higher voltage than the subsequent cycles.

The external current limitation during the SET process limits the ionic current which can flow during the switching process. Hence it controls the amount of metal atoms contributing to the filament diameter and consequently its resistance. A low current compliance ensures a thin filament and high resistance of the LRS, whereas a high limit leads to a thick filament with a low resistance of the LRS. This gives rise to a possible enhancement of the cells' memory density by multi bit data storage. A cell can not only store the two logical states HRS and LRS, but the LRS can be divided into several logical states with different filament diameter and resistance.  $2^n$  distinguishable states in one single cell lead to an amount of  $n$  bit which can be stored in the cell. 4 different states, the HRS and 3 different LRS, could be attributed to 4 different logical states: "00", "01", "10", and "11" and therefore represent 2 bits in terms of data storage (see schematic in fig. 2.3). The number of discernible LRS depends on the complexity of the read-out circuitry and the stability of the substates of the LRS. Sensitive read-out electronics for magnetic RAM can distinguish resistance ratios of 1.3 [85]. ReRAM devices with 92 distinguishable states, i.e. 6.5 bits, have already been presented [123]. A high degree of multi bit operation requires stable and reproducible LRS as well as a large resistance window between HRS and LRS. This allows to easily distinguish HRS and LRS and provides enough difference in resistance between HRS and LRS for a considerable variation of the LRS.

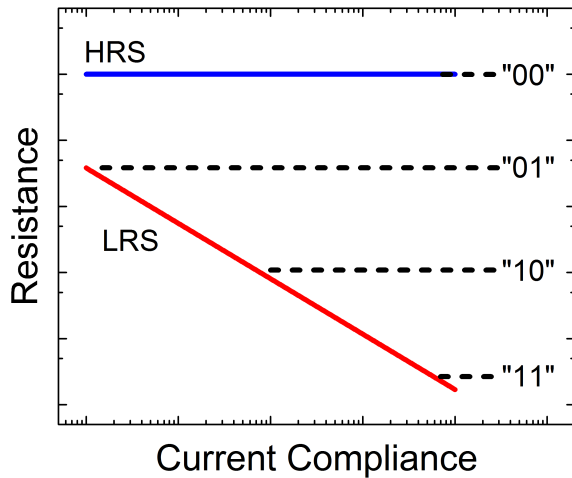


Figure 2.3: Schematic of multi bit data storage. Depending on the current compliance, different substates of the LRS can be accessed. In this example the LRS is divided into 3 different resistance levels, which gives 4 logical states or 2 bits together with the HRS.

### 2.3.2 Electrode and Solid Electrolyte Materials

This subsection covers the basic properties of all materials used for the conductor-insulator-conductor sandwich stack of the memory cells. The various different material compositions with a cell consisting of three or four single layers are given in chapter 4. Here, the individual materials are described in detail: Ag as active bottom electrode in nanoparticle or nanowire shape, spin-on-glass (SOG) or  $\text{WO}_3$  as insulating material, and the conducting polymer poly(3,4-ethylenedioxythiophene) polystyrene sulfonate (PEDOT:PSS) as inert electrode.

Ag is commonly used as active electrode material in ECM cells due to several advantages. Its standard electrode potential for oxidation (relative to the standard hydrogen electrode)  $E^0(\text{Ag}^+/\text{Ag}) = 0.80 \text{ V}$  is smaller compared to commonly used inert electrodes such as Pt with  $E^0(\text{Pt}^{2+}/\text{Pt}) = 1.18 \text{ V}$  and Au with  $E^0(\text{Au}^+/\text{Au}) = 1.69 \text{ V}$  and can therefore easily be oxidized [16][105]. Furthermore, the standard Gibbs free energy of oxide formation  $\Delta_f G^\circ(\text{Ag}_2\text{O}) = -11.2 \frac{\text{kJ}}{\text{mol}}$  [70] has a smaller absolute value than those of electrolyte materials such as  $\Delta_f G^\circ(\text{WO}_3) = -542.5 \frac{\text{kJ}}{\text{mol}}$  and  $\Delta_f G^\circ(\text{SiO}_x) = -856.4 \frac{\text{kJ}}{\text{mol}}$  [23]. Hence, the created  $\text{Ag}^+$  ions migrating through the solid electrolyte only show weak interaction with the insulating material and are not prone to react and remain as oxide in the electrolyte [105]. Ag inks for inkjet printing can consist of solutions containing dissolved Ag [120], but mainly use suspended Ag nanoparticles in a solvent [67]. Suspensions of Ag nanoparticles are typically synthesized from an Ag precursor such as silver nitrate and covered with a surfactant which inhibits agglomeration or sedimentation of Ag nanoparticles in the ink [67]. The size distribution of the created Ag nanoparticles can be influenced by the precursor concentration or reaction parameters such as temperature. The shape of the nanoparticles can even be changed from spherical to a cylindrical nanowire shape. To that end, poly(vinyl pyrrolidone) is added to the solution during synthesis, which coordinates to specific crystal orientations of the emerging Ag nanoparticles and stops the growth at these faces of the nanoparticle surface. At the faces not covered with poly(vinyl pyrrolidone) the silver nitrate can still be reduced and Ag growth is limited to these surfaces [124]. This procedure can produce cylindrical Ag nanowires with very high aspect ratios. The nanowire diameter is typically in the range of tens of nm, while their lengths can amount to several tens of  $\mu\text{m}$ . To offer an optimized printability, the ink's solvent composition is tailored to meet the requirements of the printing process (see subsection 3.1.1). After printing most inks are sintered to remove solvents, possible surfactants, and to achieve high conductivity (see subsection 3.1.2).

A *UTDots AGIJ* silver nanoparticle ink with a particle diameter smaller than 10 nm is used, which is diluted with *UTDots Solvent* to achieve a silver content of 25 wt.%. This dilution results in a decreased thickness of the printed Ag line and thus facilitates a complete coverage with SOG and prevents short circuits between bottom and top electrode. The diluted *UTDots AGIJ* ink has a dynamic viscosity of 11.2 mPa s, a density of 0.71  $\frac{\text{g}}{\text{cm}^3}$ , and a surface tension of 28.2  $\frac{\text{mN}}{\text{m}}$  at 20°C. The surface tension is determined using the pendant drop method with a *Kruess drop shape analyzer* [11]. A *Brookfield Rotation Viscometer DV2TLV* with a cone/plate system serves to measure the dynamic viscosity of the materials [93]. A detailed summary of the parameters of the different materials, which are crucial for inkjet printing, can be found in table 3.1.

A *Clear Ohm® ink-Y* from *Cambrios* with Ag nanowires of 20-40 nm diameter and tens of  $\mu\text{m}$  length serves as nanowire ink. It is worth mentioning that the nozzle diameter of 21  $\mu\text{m}$  is similar to the length of individual Ag nanowires. Most possibly, flow induced alignment of the nanowires during printing reduces clogging of the nozzles due to jammed nanowires [36]. Since the ink solely uses isopropanol as solvent, it is diluted with the high boiling point solvent 1-pentanol in a volume ratio of 1:2 in order to prevent clogging of the nozzles caused by evaporating solvent [86]. The diluted *Cambrios ink-Y* shows a dynamic viscosity of 7.7 mPa s, a density of 0.80  $\frac{\text{g}}{\text{cm}^3}$ , and a surface tension of 23.3  $\frac{\text{mN}}{\text{m}}$  at 20°C.

Spin-on-glasses (SOG) are a material class consisting of a solution of solvents and spin-on material. It is commonly used in a spin-coating process for planarizing and insulating structured layers on a wafer. Here, it serves as ink for the printing process. The spin-on material consists of a silicon-oxide compound which condenses into a  $\text{SiO}_x$  layer after a thermal curing step.

There are two main groups of SOG: silicate and siloxane based SOG.

The silicate SOG forms a strong  $\text{SiO}_x$  network through a condensation reaction of the  $\text{Si}(\text{OH})_4$  groups by losing water. The significant film shrinkage creates high stress values in the cured film of typically 500 MPa and facilitates crack formation [24]. Doping the silicate SOG with phosphorous modifies the  $\text{SiO}_x$  network and reduces the film stress to typically 200 MPa.

The siloxane SOG contains methyl (-CH<sub>3</sub>) and ethyl (-C<sub>2</sub>H<sub>5</sub>) groups bonded to the Si-O backbone, which lower the film stress to approximately 200 MPa and improves the crack resistance (see Fig.2.4). Siloxane SOG usually has a higher viscosity and leads to thicker films and better planarization.

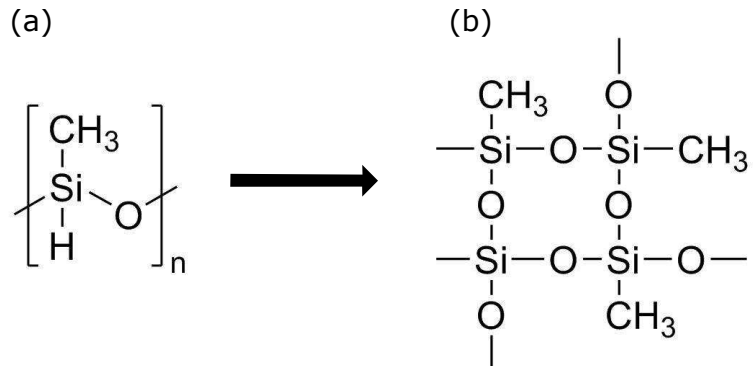


Figure 2.4: (a) Methylsiloxane SOG with one methyl group on the Si-O backbone. (b) Cured methylsiloxane SOG film with organic rests reducing the film stress.

Both types of SOG require a thermal curing step to form a  $\text{SiO}_x$  film. Silicate SOG can be cured at high temperatures of 700°C to 1000°C in order to form pure  $\text{SiO}_x$  networks. For lower temperatures, silanol (Si-OH) groups can be found in the film. Siloxane SOG is limited to 450°C, because the breaking of organic groups from the network at higher temperatures leads to higher leakage currents [2]. For both types of SOG, curing at lower temperatures leads to remaining silanol or organic remainders in the  $\text{SiO}_x$  structures. Siloxane SOG is used for the ECM cells in

this work due to its superior crack resistance and planarization behavior.

SOG solutions are designed and optimized for the spin-coating process and therefore usually do not meet the inkjet printing requirements since their viscosity is too low and they face a high concentration of low boiling point solvents. The latter can lead to print head clogging due to increased evaporation of the ink at the printing nozzles. Mixing the SOG with other solvents in order to increase its viscosity can jeopardize the insulating behavior of the film [39]. Therefore, in this work the SOG is not diluted with any solvents. This leads to a more complicated printing process with satellite droplets due to the low viscosity and a distinct coffee stain effect (see subsection 3.1.1), but ensures good insulation of the SOG.

As methylsiloxane SOG a *Honeywell Accuglass<sup>TM</sup> T-11 111* SOG is used with a dynamic viscosity of 1.7 mPa s, a density of 0.90  $\frac{\text{g}}{\text{cm}^3}$ , and a surface tension of 21.9  $\frac{\text{mN}}{\text{m}}$  at room temperature. The phosphosilicate SOG *Honeywell Accuglass<sup>TM</sup> P-5S* shows a dynamic viscosity of 1.6 mPa s, a density of 0.87  $\frac{\text{g}}{\text{cm}^3}$ , and a surface tension of 25.3  $\frac{\text{mN}}{\text{m}}$ .

As alternative to SOG as amorphous, but dense  $\text{SiO}_x$  layer, crystalline, but not sintered  $\text{WO}_3$  nanoparticles can be employed. The loose structure of the  $\text{WO}_3$  nanoparticle agglomeration offers a great amount of interface states and voids between the individual nanoparticles, which can influence the switching mechanism. The *Avantama P-10*  $\text{WO}_3$  nanoparticle ink consists of a dispersion of 2.5 wt% of  $\text{WO}_3$  nanoparticles of 12-16 nm size in isopropanol with a dynamic viscosity of 2.5 mPa s, a density of 0.80  $\frac{\text{g}}{\text{cm}^3}$ , and a surface tension of 20.2  $\frac{\text{mN}}{\text{m}}$ .

ReRAM cells with bipolar switching mechanism most often use an inert electrode consisting of Pt or W [105]. Nanoparticle inks containing Pt or W would require sintering temperatures to generate conductive layers, which surpass the highest temperatures typical polymer foil substrates can withstand. Therefore, the organic polymer PEDOT:PSS serves as printed inert top electrode. PEDOT:PSS is highly conductive, transparent, and shows a high ductility. Therefore, it is one of the main workhorses of organic electronics and finds applications in organic light emitting diodes, solar cells, or field-effect transistors [31][108][49]. PEDOT:PSS is a blend of the oxidatively doped, cationic PEDOT which is electrostatically bond to a PSS anion [99]. The morphology of a dried film is anisotropic with lentil-shaped structures with a size of tens of nm [99]. These individual grains contain a PEDOT-rich core and a PSS-rich shell and are held together by hydrogen bonds created between the sulfonate groups of PSS. The electrical conductivity originates from a hopping process of charge carriers and highly depends on the morphology of the PEDOT:PSS [34]. Added organic solvents interact with PEDOT chains and can change their structure and let them uncurl. This can to a great extent increase the conductivity due to elevated mobility [75].

A *Clevios<sup>TM</sup> P Jet N V2* PEDOT:PSS ink from *Heraeus* serves as top electrode and is a standard inkjet ink for organic electronics. Its dynamic viscosity is 22.5 mPa s, its density 1.00  $\frac{\text{g}}{\text{cm}^3}$ , and its surface tension is 24.8  $\frac{\text{mN}}{\text{m}}$ .

### 2.3.3 Failure Mechanisms

An ideal ReRAM cell is able to switch an infinite amount of times between HRS and LRS without changing its switching behavior. However, real memory devices are subjected to material degradation, which can induce various types of failure of the memory cell. This subsection will describe the most common failure mechanisms for ECM cells.

A cell can get stuck in either LRS or HRS without being able to switch to the other state again and causing irreversible failure of the cell. An irreversible LRS originates in a metal filament with a high thickness, where the Ostwald ripening process assisted by Joule heating does not suffice to cause a filament rupture. Therefore, the filament cannot be electrochemically disintegrated again. This failure mode is usually caused by a too high current compliance, which allows a high ionic current during the SET process and leads to a too thick filament.

A cell stuck in the HRS without being able to SET again can be related to degradation of the active electrode. The active electrode has to serve as material reservoir and provide the metal atoms making up the filament. When the active electrode is not structured as bulk material but itself is composed as nanostructures with the same dimension as the filament, a considerable part of the electrode is consumed during the SET process. Repetitive switching, i.e. migration and diffusion of the active metal atoms, can lead to a sparse dispersion of active metal atoms over the cell structure, which is not able to form a filament again. This failure mode only occurs when the active electrode is composed from sparsely distributed nanostructures such as individual nanoparticles or nanowires.

Whereas the first two mechanisms are related to the active electrode, degradation of the insulating layer can also lead to degradation and failure of the switching process. The ideal insulator for ECM has to block electronic leakage current while still allowing ionic current during SET and RESET. The soft dielectric breakdown as well as consecutive switching cycles can cause a degradation of the insulating layer, which increases the amount of electronic leakage current. This leads to a decrease of the resistance value of the HRS and therefore narrows the resistance window between HRS and LRS.

An additional failure mechanism is related to the diffusion of the metal filament in the LRS into the insulator without applied voltage, which determines the retention time. This diffusion process can be mathematically expressed using Fick's law of diffusion.

Isotropic diffusion of one material into another caused by random movement of each particle can be described by the diffusion equation, regardless of whether a salt diffuses in a liquid or metal atoms diffuse in a crystal lattice of a semiconductor. The diffusion equation is also called Fick's second law since it is a combination of Fick's first law together with the continuity equation [35]:

$$\frac{\partial C}{\partial t} = \nabla \cdot (D \nabla C) \quad (2.1)$$

, where  $C(x, y, z, t)$  is the particle concentration field and  $D$  is the diffusion coefficient. For a constant diffusion coefficient it becomes a linear second-order partial differential equation, which can be solved for given initial and boundary conditions.

The radial diffusion of the metallic filament only depends on the radial distance  $r$  from the filament center due to its cylindrical structure. Therefore, equation 2.1 can be transferred into the cylindrical coordinate system and only the partial derivatives in  $r$  have to be considered:

$$\frac{\partial C}{\partial t} = \frac{1}{r} \frac{\partial}{\partial r} (r D \frac{\partial C}{\partial r}) \quad (2.2)$$

The boundary conditions are an initially uniform metal concentration throughout the cylinder  $C_1$  and a constant concentration  $C_0$  outside of the initial cylinder radius  $r \geq r_0$ .  $C_0$  represents the small background metal concentration of metal in the insulator due to diffusion from the electrode and preceding switching cycles. With these boundary conditions the differential equation 2.2 can be solved and leads to:

$$M(t) = M(t=0) \sum_{n=1}^{\infty} \frac{4}{\alpha_n^2} e^{-\frac{D}{r_0^2} \alpha_n^2 t} \quad (2.3)$$

, where  $M_t$  is the quantity of metal which is left in the initial cylinder in time  $t$ ,  $M(t=0)$  the corresponding quantity at time  $t = 0$  and  $\alpha_n$  are roots of the Bessel function of the first kind of order zero ( $J_0(\alpha_n) = 0$ ) [28]. A detailed deduction of the formula can be found in [28].

The electrical resistance of the filament  $R_{\text{fil}}(t)$  is given by the formula:

$$R_{\text{fil}}(t) = \rho \frac{l}{A(t)} \quad (2.4)$$

, where  $\rho$  is the electrical resistivity of the metal,  $l$  is the length of the filament, and  $A(t)$  is the cross sectional area of the cylindrical filament. Thus, with  $R_{\text{fil}}(t) \propto \frac{1}{M(t)}$  and  $R_{\text{fil}}(t=0) \propto \frac{1}{M(t=0)}$  equation 2.3 becomes:

$$R_{\text{fil}}(t) = \frac{1}{\frac{1}{R_{\text{fil}}(t=0)} \sum_{n=1}^{\infty} \frac{4}{\alpha_n^2} e^{-\frac{D}{r_0^2} \alpha_n^2 t}} \quad (2.5)$$

This relationship between  $R_{\text{fil}}$  and  $t$  can be used to model the memory cells' behavior and determine information on the diffusion coefficient or the maximum retention time.

While variation or even degradation in the switching behavior of memory cells is highly detrimental in a conventional computing architecture, it can even be advantageous for neuromorphic computing, since it directly represents stochastic variability inherent to biological computing systems [56].

### 2.3.4 Resistive Memory for Neuromorphic Computing

The human brain outperforms conventional computers when it comes to real-time processing of unstructured data, such as image, video or voice recognition. This is achieved by its radically different structure: it is extremely parallel with a three-dimensional organization and combines storage and computation [69]. This results in a superior power efficiency with a power consumption of only approximately 15 W for one human brain [3]. By contrast, computers built to perform comparable tasks using CMOS logic and the von-Neumann architecture have power consumptions in the range of kW to MW. IBM simulated a computing architecture with  $5.3 \cdot 10^{11}$

neurons, and  $1.37 \cdot 10^{14}$  synapses, which represents the actual numbers in the human brain. The supercomputer necessary for the computation used 7.9 MW of power and ran approximately 1500 times slower compared to a real time brain operation [56][138].

Therefore, in order to mimic the brain's architecture with an Artificial Neural Network (ANN) it is not sufficient to simulate the architecture using CMOS logic. Instead, the brain structure has to be directly reproduced with suitable devices. Here, an ECM cell can mimic the function of a synapse and reproduce its plasticity, which is essential for the learning process. A synapse located between two neurons can gradually change its electrical resistance and thus create a stronger or weaker connection between them. The synaptic plasticity, i.e. the ability of synapses to strengthen or weaken, can be emulated by the strengthening and weakening of the metallic filament of ECM cells. To that end, the ECM cell has to show multi bit data storage, where it can gradually change its resistance by varying the radius of the filament when stimulated with different current compliances or appropriate voltage pulses (see fig. 4.4).

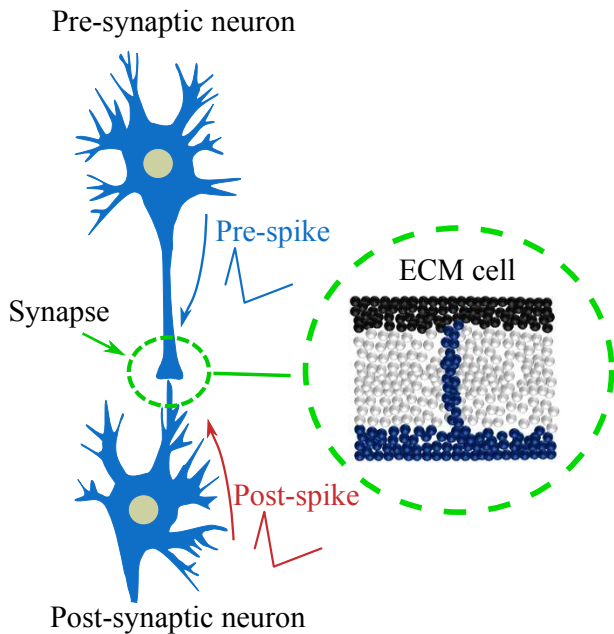


Figure 2.5: An ECM cell can adopt the behavior of a synapse. The synaptic plasticity, i.e. gradual change in the synapse's resistance, is realized by an increase or decrease in the diameter of the metallic filament.

Fig. 2.5 shows an ECM cell representing a synapse located between two neurons. The synaptic connection is directional, hence neurons can be classified in a pre-synaptic neuron and a post-synaptic neuron. A neuron can be modeled as an integrate-and-fire device, where incoming voltage spikes from other neurons are integrated and once a threshold is reached, the neuron "fires" a spike itself. In biological or neuropsychological background this voltage spike is often called "action potential". Voltage spikes from both pre- and post-synaptic neuron pass a synapse. The plasticity of the learning process, i. e. increase or decrease of a synapse's resistance, is linked to the time difference  $\Delta t$  between two spikes coming from pre- and post-synaptic

neuron. A pre-synaptic voltage spike followed by a post-synaptic spike (positive  $\Delta t$ ) implies a causal link, where the pre-synaptic neuron triggered the post-synaptic neuron to fire. Therefore, the synapse decreases its resistance to enhance such interactions in the future. Similar, a negative  $\Delta t$  (post-synaptic spike preceding a pre-synaptic spike) leads to an increase of the synapse's resistance, since a post-synaptic spike triggering the pre-synaptic neuron to fire would be against the causal direction of the synaptic connection. Hence, the increased synapse's resistance impedes interactions between the two neurons in the future. This strengthening and weakening of the synapse depending on  $\Delta t$  is called Spike-Timing-Dependent Plasticity (STDP).[65]

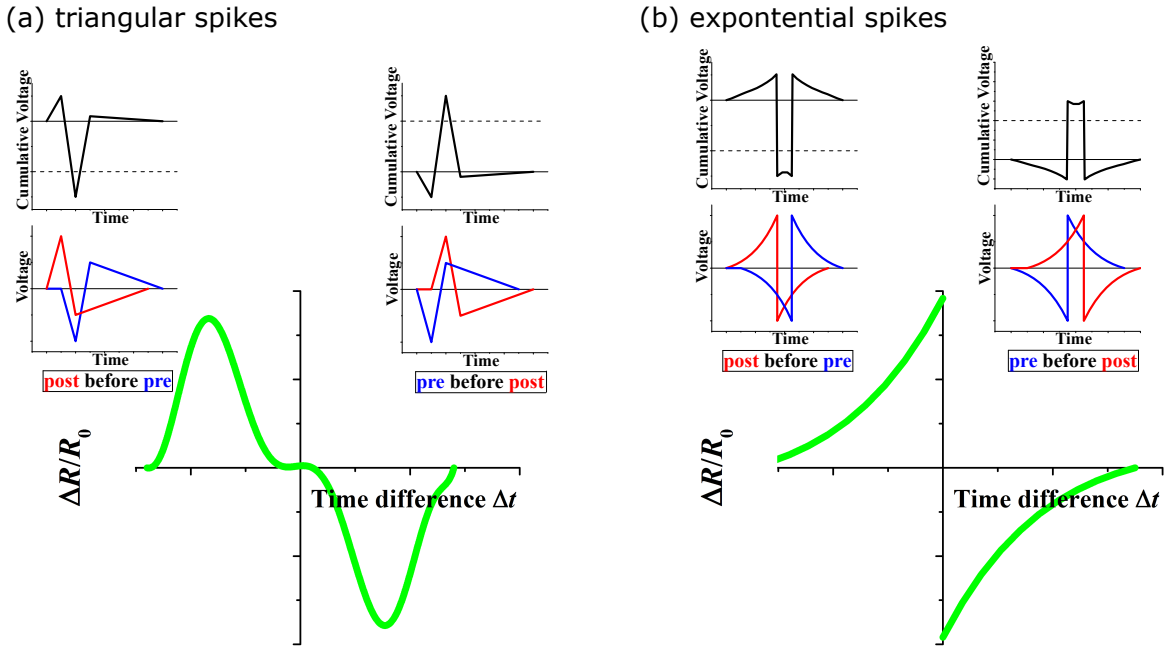


Figure 2.6: Schematic of the Spike-Timing-Dependent Plasticity (STDP) learning rule. Both (a) triangular and (b) exponential voltage spikes can trigger a resistance change in the cell. The insets show how the pre- and post-synaptic voltage spikes superimpose to a cumulative voltage. For appropriate  $\Delta t$ , this cumulative voltage can exceed the voltage threshold (dotted line) necessary for a gradual resistance change of the cell. Adapted graph is submitted.

A schematic of the synaptic learning behavior STDP is depicted in fig. 2.6. For the synapse, voltage spikes coming from the two different neurons have a different polarity. Fig. 2.6(a) shows STDP for triangular voltage spikes, which represent biologically inspired action potentials [10]. Here, the pre-synaptic spike is set as a triangular, negative pulse with a positive, smaller tail and vice versa for the post-synaptic spike. The voltage amplitude of the individual spikes is adjusted so that the amplitudes lie below the voltage threshold of the ECM cell. Thus, the individual spikes do not affect the cell resistance, but only a superposition between pre- and post-synaptic spike may trigger a change in the filament. If the pre-synaptic spike reaches the synapse before the post-synaptic spike (positive  $\Delta t$ ), the positive tail of the pre-synaptic spike superimposes the

positive post-synaptic pulse. This results in a higher voltage spike which triggers the synapse and leads to a potentiation (see inset of fig. 2.6(a)). The ECM cell is gradually SET, leading to a thicker metallic filament and a decrease in resistance. For a negative  $\Delta t$ , the post-synaptic spike precedes the pre-synaptic spike and the resulting high negative voltage induces a depression of the synapse, i.e. a gradual RESET of the ECM cell.

The shape of the pre- and post-synaptic voltage spikes considerably determine the shape of the STDP function [109]. Various shapes of action potentials can be found in biological neurons depending on the type of neuron [10]. The triangular voltage spikes of fig. 2.6(a) results in a STDP function similar to two Gaussian-shaped peaks, where the maxima occur at a specific value  $|\Delta t|$ . This is due to the fact that the maximum absolute voltage of the overlap of pre- and post-synaptic spike occur, when the positive pulse of one spike coincides with the tail of the other spike. Another alternative for the shape of the action potential are exponential voltage spikes, where both pre- and post-synaptic spike are a combination of two decaying exponential functions of opposite polarity (see inset of fig. 2.6(b)). The resulting STDP function also has the shape of two decaying exponential functions with the maximum change in resistance for very small  $\Delta t$ . This is due to the fact that the superposition of pre- and post-synaptic spike causes a maximum absolute voltage for  $\Delta t$  close to  $\Delta t = 0$ . Therefore, the smallest steps of  $\Delta t$  trigger the highest change in resistance. The exponential STDP function from fig. 2.6(b) simplifies a quantitative analysis, since one exponentially decaying branch can be described by two parameters: maximum amplitude, and a time constant. By contrast, one Gaussian-shaped branch of fig. 2.6(a) is defined by three parameters: position, maximum amplitude, and full-width-half-maximum.

It is worth noticing that for STDP experiments the measurement setup does not apply separate pre- and post-synaptic voltage pulses with a time delay, but for each  $\Delta t$  the calculated superposition (black inset in fig. 2.6) is applied as a voltage pulse.

Efficient computing with an artificial, brain-inspired computer architecture calls for a specific combination of ReRAM cells to form a network. An ANN is given by interconnected groups of nodes (see Fig. 2.7(a)), where each circular node represents a neuron and each connection arrow stands for a synapse. The synapse's conductance is referred to as its synaptic weight  $w_{ij}$ . The input values  $V_i$  are connected to the output values  $I_j$  of the next node layer via the sum of all involved weight connections:  $I_j = \sum_i w_{ij} V_i$ . During the supervised learning process in a machine learning algorithm, the weights of the ANN are adjusted with a training data set. This weight adjustment minimizes the so-called cost function of the ANN by an iterative backpropagation process. A detailed overview over this network training process can be found in [13]. For the example of a simple face recognition algorithm with an ANN, each node of the input layer would represent one pixel of the investigated image. This information gets reduced through the one or more hidden layers and the output layer only contains the information "face of person A" or "not face of person A".

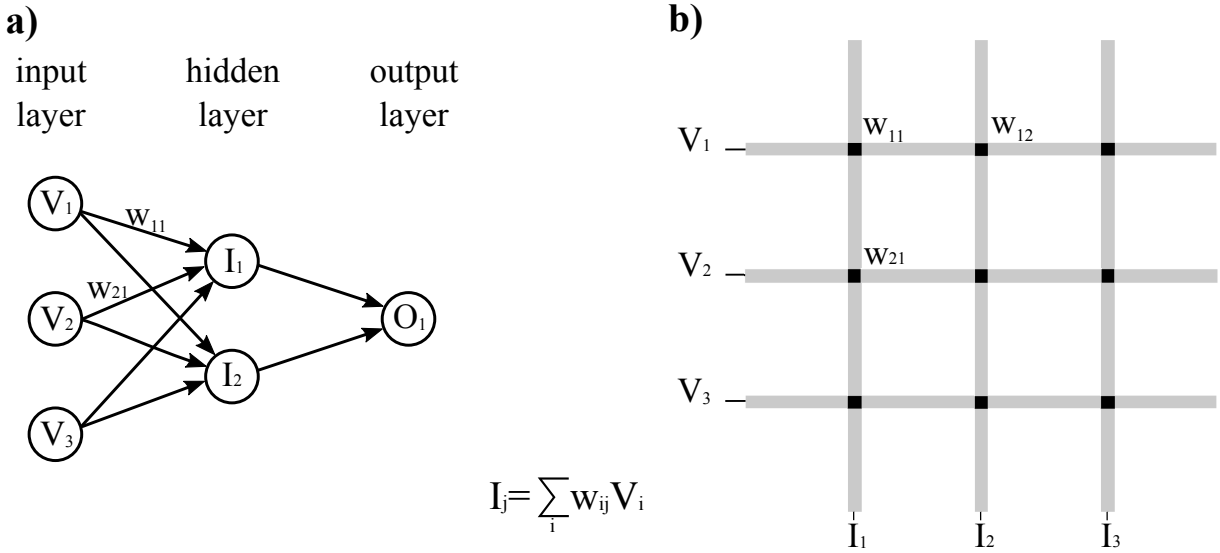


Figure 2.7: (a) Architecture of an ANN with an input, one hidden, and an output layer. (b) Crossbar array directly representing the ANN architecture: the input values  $V_i$  can be attributed to the voltages applied to the wordlines, the synaptic weights  $w_{ij}$  represent the conductance values of the ReRAM cells, and the node values  $I_j$  are the output currents of the bitlines.

The correlation between fig. 2.7(a) and (b) shows that an ANN can be directly implemented with a ReRAM crossbar structure. The output current  $I_j$  is connected to the input voltage  $V_i$  via Kirchhoff's current law:  $I_j = \sum_i w_{ij} V_i$  with the weight of the ANN being attributed to the conductance of the memory cell [141]. Each layer can be realized as one ReRAM crossbar array, while the neurons are constructed with the integrate-and-fire neuron model and for example using CMOS technology.

Based on the basic ANN structure shown in fig. 2.7(a) several models have been proposed to explain the representation of data in the network and its learning process. Although there are various different types of ANNs, historically they can be grouped into three generations of neural network models. The first generation networks from the 1940s do not consider any temporal information of the voltage spikes. Instead, they use integrate-and-fire neurons, which only release a spike, when the inputs to the neuron weighted with the synaptic weights reach a certain threshold [92]. The second generation encodes information in the firing rate of the spikes and therefore can generate non-binary outputs of neurons. However, only the third generation of ANNs, also called spiking neural networks (SNNs), directly models time by relying on the exact timing of individual spikes. SNNs use integrate-and-fire neurons and a learning process depending on the timing of the spikes such as STDP [54]. SNNs are biologically more realistic and computationally more powerful compared to ANNs from the first and second generation [84].[42]

## 2.4 Bending Theory

Flexible electronic devices have to guarantee a certain amount of flexibility to prevent malfunction or failure. Therefore, device testing to prove and quantify its resilience against bending is crucial. This section gives a very basic overview on how strain acts on printed structures on a substrate during bending.

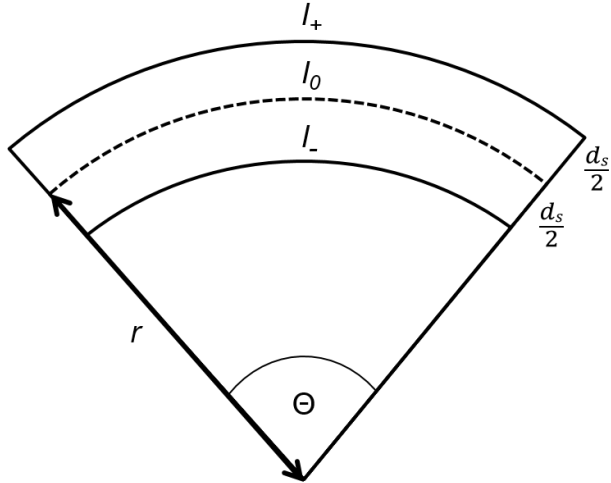


Figure 2.8: When the substrate is bent over a specific bending radius  $r$ , its middle, neutral axis remains at the initial length  $l_0$ . The outer surface is stretched to  $l_+$  due to tensile bending, the inner surface is shortened to  $l_-$  due to compressive bending.

When a substrate of thickness  $d_s$  is bent over a bending radius  $r$ , structures on the substrate experience a strain  $\epsilon$ . The bending can either be free or over a cylinder. If there is no additional plastic deformation, the middle, neutral axis of the substrate is not subjected to strain and keeps its initial length  $l_0$ . The middle plane of the substrate is bent to an arc with the length  $l_0 = r\Theta$ . The outer surface of the substrate experiences tensile strain and is stretched to  $l_+ = (r + \frac{d_s}{2})\Theta$ . Similarly, the inner surface is subjected to compressive strain and is shortened to  $l_- = (r - \frac{d_s}{2})\Theta$ . A schematic of the bent substrate can be seen in fig. 2.8. The strain  $\epsilon$  acting on deposited structures on the substrate can therefore be positive for tensile and negative for compressive bending:

$$\epsilon = \frac{l_{\pm} - l_0}{l_0} = \frac{(r \pm \frac{d_s}{2})\Theta - r\Theta}{r\Theta} = \pm \frac{d_s}{2r} \quad (2.6)$$

For the sake of completeness, the thickness  $h$  of the printed structures should be added into the formula to account for  $\epsilon = \frac{d_s+h}{2r}$ . Since the foil substrate usually has a thickness of tens of  $\mu\text{m}$ , while the printed structures are a few hundreds of nm thick, it can be neglected.

Bending a conductor on a substrate, for example a printed Ag line on a polymer foil, results in a change in its resistance. This is caused by a change in geometry of the conductor and for some materials also induced by the piezoresistive effect. The normalized change in resistance  $\frac{\Delta R}{R}$  is

linked to the strain  $\epsilon$  via the gauge factor  $k$  in a linear behavior:

$$\frac{\Delta R}{R} = k \cdot \epsilon \quad (2.7)$$

$k$  depends on the material and geometry of the conducting structure on the substrate.[14]

# Chapter 3

## Methods

In the same way that the *Fundamentals* chapter covers the theoretical fundamentals necessary for a better understanding of the results, this chapter describes the most important practical techniques which are used in this thesis. The fabrication of the ECM cells presents inkjet printing followed by the sintering process and illustrates the layout of the memory cells. Atomic force microscopy and electron microscopy are described as well as the electrical characterization setup. These analysis techniques are mainly used for the characterization of the printed memory cells. Finally, the in-house built rotate-to-bend setup used for the mechanical characterization of the cells' flexibility is described.

### 3.1 Fabrication

#### 3.1.1 Inkjet Printing

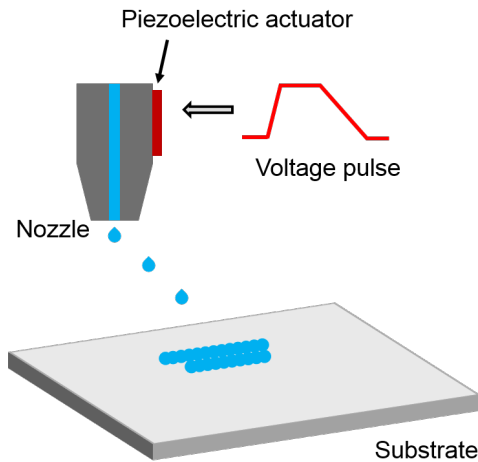


Figure 3.1: Schematic of the inkjet printing process with a piezoelectric actuator located next to the ink channel and the nozzle.

Inkjet printing is an additive manufacturing method, which provides two main advantages: Firstly, in order to fabricate one structured layer of material, inkjet printing uses one addi-

tive process step under ambient conditions, whereas standard optical lithography requires four to five process steps in cleanroom environment. Therefore, inkjet printing accounts for extremely low production costs. Secondly, in contrast to cleanroom technology, which is limited to rigid wafer substrates, inkjet printing can use any substrate with acceptable surface roughness. Printing on flexible foils enables various applications in the field of flexible electronics.

A piezoelectric actuator is located next to an ink-filled channel behind the nozzle. When a tunable voltage pulse, i.e. waveform, is applied to the piezoelectric material, it deforms and an ink droplet is pushed out of the nozzle (see Fig. 3.1). The voltage pulse can be tuned to match a wide variety of inks with different viscosities and surface tensions. All the different waveforms for the various inks are shown in appendix B. An inkjet ink consists of a solution or dispersion of functional material in a liquid vehicle, the solvent. Inks can contain metal nanoparticles, conducting as well as non-conducting polymers, insulators or photochemically active materials [119]. In any case, the ink has to match requirements concerning its fluid properties in order to be printable. The so-called  $Z$  number, the inverse of the Ohnesorge number, is a dimensionless value to determine an ink's aptitude for inkjet printing [37]:

$$Z = \frac{\sqrt{L_N \rho \sigma}}{\eta} \quad (3.1)$$

, where  $L_N$  is the nozzle diameter,  $\rho$  is the density of the ink,  $\sigma$  is its surface tension and  $\eta$  its dynamic viscosity. It was empirically shown that the range of  $1 < Z > 10$  is optimal for drop-on-demand inkjet printing. For  $Z < 1$ , typically the high viscosity hampers the dissipation of the pressure pulse in the ink: For  $Z > 10$ , satellite droplets accompany the main droplet and affect the print quality [112][131].

Table 3.1: Density  $\rho$ , surface tension  $\sigma$ , dynamic viscosity  $\eta$ , and the  $Z$  number for the different inks. The exact product name and dilution process for the silver inks is described in subsection 2.3.2

ink	density [g cm <sup>-3</sup> ]	surface tension [mN m <sup>-1</sup> ]	viscosity [mPa s]	$Z$ number for $L_N = 21 \mu\text{m}$
Ag nanoparticle ink	0.71	28.2	11.2	1.8
Ag nanowire ink	0.80	23.3	7.7	2.6
SOG T11	0.90	21.9	1.7	12.2
SOG P5S	0.87	25.3	1.6	13.8
WO <sub>3</sub> ink	0.80	20.2	2.5	7.4
PEDOT:PSS ink	1.00	24.8	22.5	1.0

All parameters of equation 3.1 for the different inks are shown in table 3.1. The  $Z$  numbers are calculated for  $L_N = 21 \mu\text{m}$ , the nozzle diameter of the *DMC-11610* cartridge of the *Dimatix DMP2832* printer. Except for the SOG inks, the  $Z$  numbers for all materials are within the printing range  $1 < Z > 10$ . The  $Z$  numbers of 12.2 for the T11 SOG and 13.8 for the P5S SOG lead to unpreventable satellite droplets during printing. Those smaller satellite droplets

can follow a different trajectory than the main droplet and form an array of small SOG dots next to the printed SOG line on the substrate. However, this does not cause any functional disadvantage of the printed memory cells.

After the droplet hits the substrate, the substrate-droplet interface expands and comes to rest after a series of damped oscillations [131]. The final radius, i.e. the spreading of the ink droplet depends on the surface energy of the substrate and the interaction between ink and substrate. It can be tailored for specific inks by rinsing the substrate with either polar or non-polar solvents or subjecting it to an oxygen plasma prior to printing. For example, oxygen plasma treatment enhances a substrate's hydrophilic properties. As a result, a non-polar ink would spread less, whereas a polar ink would spread more on a substrate treated with oxygen plasma.

To pattern a given structure on a substrate, a grid of droplets is printed which overlap and form the structure. The distance between the drops on the substrate, the so-called drop spacing, is a crucial factor for printing quality and has to be adjusted according to the ink properties and its interaction with the substrate. If the drop spacing is too high, the droplets on the substrate tend to not overlap and therefore gaps arise in the structure. If it is too low, too much material is deposited and the structure will get bulged [66]. Therefore, the drop spacing has to be optimized for any given combination of ink and substrate.

Another important effect on the feature of the printed structure is the so-called coffee stain effect, which describes the tendency of the dissolved material to deposit at the fringe of the structure. Its name stems from the typical ring shape of a dried coffee droplet. Directly after the ink droplet wets the substrate, the evaporation rate of the solvent is higher at the fringe of the structure, where the contact line between the ink and the substrate is pinned [32]. Hence, material from the center flows to the fringe, causing more deposited material at the boundary and creating a higher feature size of the structure at the fringe. To limit the coffee stain effect, an ink with low solvent content is favorable. Moreover, heating the substrate during printing reduces the coffee stain effect since it increases the evaporation rate of the entire printed structure [126]. A mixture of two solvents with different boiling temperatures can also reduce the effect [125].

### 3.1.2 Sintering

After printing a pattern on a substrate, the solvent has to be removed by evaporation. Some inks, e.g. inks containing an intrinsically conducting polymer, are now fully functional and do not need any additional process step. However, most of the inks, especially those containing metal nanoparticles, require an additional sintering step.

A sintering step comprises an elevated temperature treatment of the printed structures. Metal nanoparticles are usually covered with a polymeric stabilizing layer to prevent coagulation of the ink. After printing, this polymeric layer acts as an insulator between the individual nanoparticles [66]. The thermal treatment removes the polymeric layer and fuses the nanoparticles, which form a network of conductive tracks. It is worth noticing, that the melting temperature of metal nanoparticles is considerably lower compared to bulk material due to the high surface area to volume ratio of the particles [17]. Thus, a printed metallic structure can achieve a resistivity

close to the value of the bulk material [45]. The effects of sintering a printed silver nanoparticle line can be seen in Fig. 3.2.

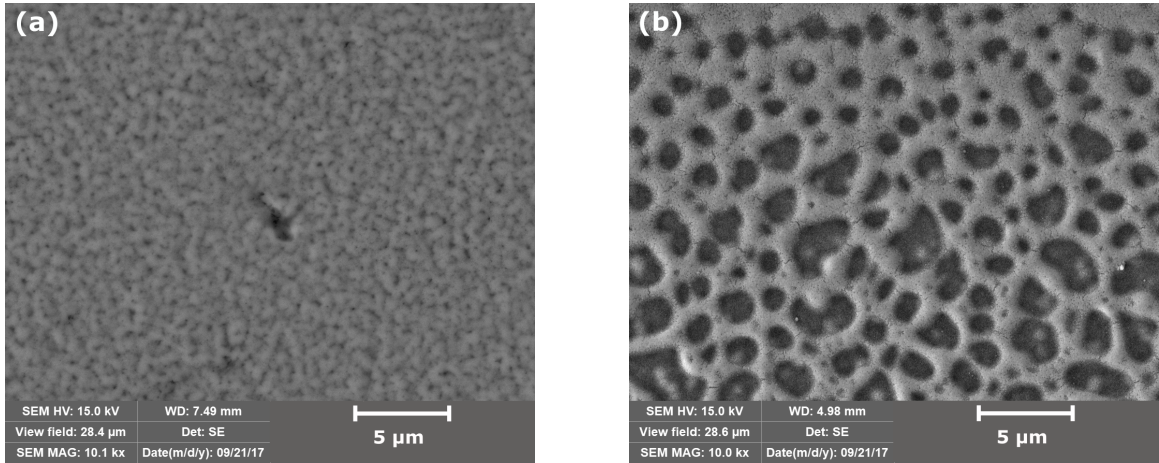


Figure 3.2: Inkjet-printed line of silver nanoparticles with 10 nm average diameter. (a) Un-sintered. (b) Sintered at 200°C in an oven. The sintering process leads to a densification and creates a conductive layer.

For thermally conducting substrates, the sintering process can take place on a hotplate. Polymer foil substrates with poor heat conduction should be sintered in an oven, which allows for purging with inert gases during sintering. This can prevent oxidation of the metal layers at the applied elevated temperatures. Alternative sintering methods include photonic, electrical, or microwave sintering as method for the heat input [101][6][107].

### 3.1.3 Memory Cell Layout

ReRAM cells can achieve a cell size of  $4F^2$ , when structured in a crossbar array. Here, the minimum feature size  $F$  denotes the smallest possible structures feasible by the fabrication process. In a crossbar array the parallel lines of the bottom electrodes are crossed perpendicularly by the parallel lines of the top electrodes (see Fig. 3.3(a)). The bottom and top electrodes are also called wordlines and bitlines in this layout. A specific cell can be switched and read out by applying voltages between its respective word- and bitlines. However, so-called sneak paths of the current through neighboring cells can jeopardize the measurements. Neighboring cells in the LRS can lead to critical leakage currents (see Fig. 3.3(b)). There are various approaches to limit the sneak path issue. In passive arrays, specific read out and write schemes can be used. To write or read out a cell its wordline is charged with an input voltage of  $V_{in}$  and its bitline is set to ground. To minimize the voltage drop between the target cell and its neighboring cells, all the other word- and bitlines are charged with  $V_{in}/2$ . Another approach inserts a transistor as selector device at each intersection of word- and bitlines and efficiently suppresses any leakage currents [77]. For unipolar devices, pn-diodes can be used as selector devices [73]. A more detailed overview over different types of selectors can be found in [55]. The stacking of two identical memory cells on

top of each other creates a complementary device and can limit the sneak path issue without any additional selectors [80].

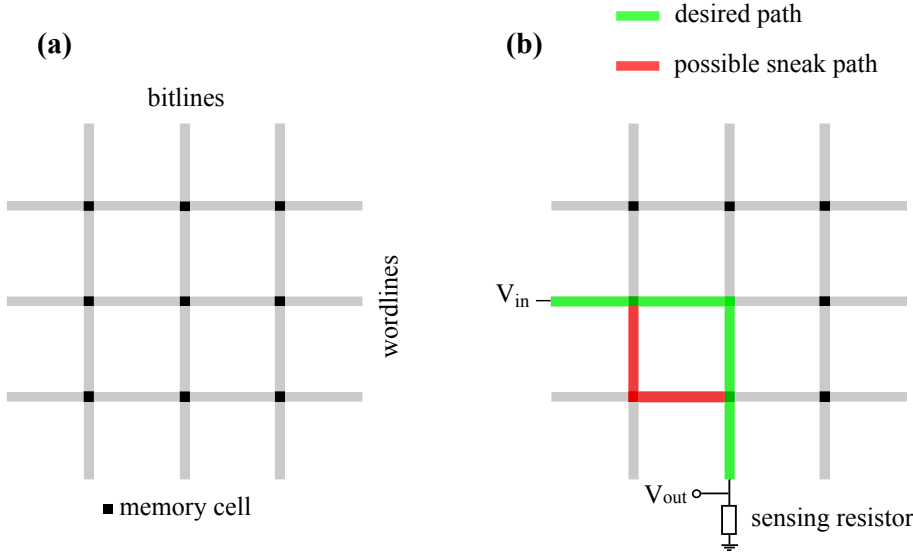


Figure 3.3: (a) Schematic of a crossbar array where each intersection of wordline and bitline forms one memory cell. (b) Sneak path issue: the desired current path for the target cell in the middle is depicted in green. Undesired leakage currents can "sneak" through neighboring cells and distort the measurement (shown in red).

However, in order to rule out any influence of sneak path currents, mostly structures with only one wordline and several bitlines are used in this thesis. Thus, all measurements are clearly attributed to processes on the single memory cell level only. Fig. 3.4 shows 5 printed memory cells. One Ag nanoparticle bottom electrode acts as wordline, which is covered by a layer of SOG. Five perpendicular PEDOT:PSS top electrodes make up the bitlines.

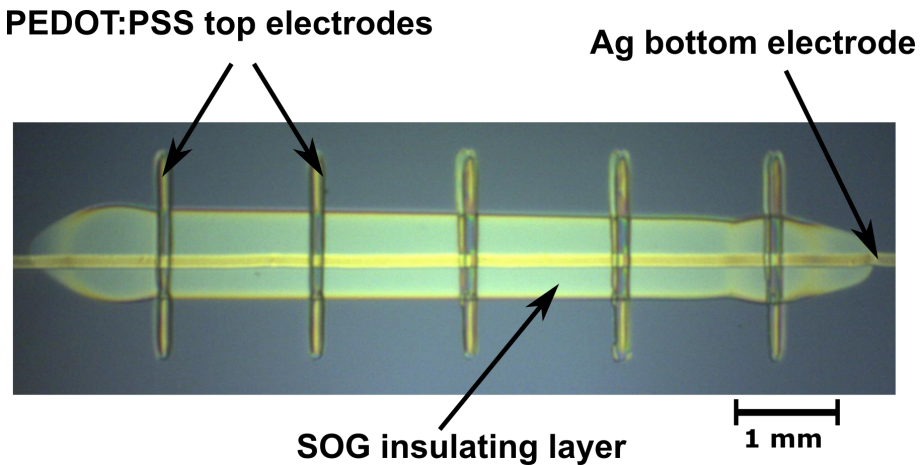


Figure 3.4: Photograph of printed memory cells with one Ag nanoparticle electrode as wordline and 5 PEDOT:PSS top electrodes on a Si/SiO<sub>2</sub> wafer.

## 3.2 Analysis

### 3.2.1 Conductive Atomic Force Microscopy

Atomic force microscopy (AFM) is one of the most powerful and well-established techniques for surface imaging at the nanoscale. A sharp probe attached to a cantilever raster scans the sample surface and gives a three-dimensional image of the topography. Precise positioning of the probe with respect to the sample is achieved by piezo-electric scanners, which rely on the inverse piezo-electric effect. For the lateral raster scanning in x-y-direction, the sample is usually attached to a flexure scanner. The change in height ( $\Delta z$ ) is detected by an additional linear piezo scanner combined with an optical setup (see Fig. 3.5).

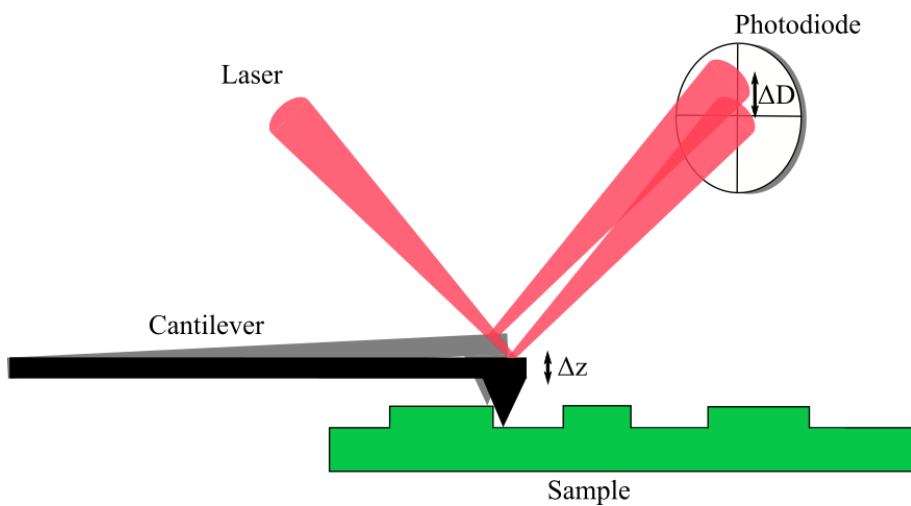


Figure 3.5: Basic working principle of an AFM. A change in topography by  $\Delta z$  bends the cantilever and leads to a deflection of the laser spot on the photodiode by  $\Delta D$ .

When the tip is brought into contact with the sample surface, the cantilever bends due to attractive Van-der-Waals forces or Pauli repulsion. A laser beam is reflected from the cantilever onto a four-sector photodiode and the change of the laser spot position by  $\Delta D$  indicates the deformation of the cantilever on the sample. The deflection of the laser spot on the photodiode is used as feedback signal for the feedback loop of the z-piezo scanner.

In contact mode operation, the tip is always in mechanical contact with the sample surface and the laser deflection, i.e. cantilever deformation is kept constant during scanning. Contact mode operation allows for high scan speeds, but the combination of lateral and normal forces reduces the resolution. Furthermore, the tip is prone to wear by the sample or vice versa.

However, the constant mechanical contact between probe and sample gives the possibility to measure the space-resolved conductance of the sample. This technique is called conductive atomic force microscopy (CAFM) and requires the probes to be coated with conductive layers such as Pt, Au or doped diamond [98]. By applying a voltage between probe and sample during scanning, the sample's electrical properties can be measured simultaneously with its topography. It should be noted that the coating increases the tip diameter and thus leads to a reduced lateral

resolution. Furthermore, the coating is prone to wear or delaminate due to lateral forces or melt due to high current densities at the apex of the tip during scanning.

CAFM not only enables current mapping of the sample, but also local current-voltage measurements. To that end, constant voltage or current-voltage-sweeps can be applied to the resting tip in order to locally manipulate the sample.

All AFM and CAFM measurements are performed using a *SmartSPM 1000* system from *AIST-NT*, which provides different current ranges for scanning and local current-voltage-sweeps of either 1 nA, 100 nA or 10  $\mu$ A. Pt/Ir-coated *ANSCM-Pt* probes from *Applied NanoStructures Inc.* with a tip radius of 30 nm are used for the conductive measurements. To limit the current, a compliance resistor can be inserted in the circuit.

### 3.2.2 Focused Ion Beam Scanning Electron Microscopy

CAFM enables the active creation of the metallic filament and gives a top view of its topography. However, the vertical stacking of the metal-insulator-metal layers impedes direct imaging of the filament's cross section. In order to access the side of the filament, the sample can be cut with a focused ion beam (FIB) directly at the side of the filament and the cross section can be imaged using scanning electron microscopy (SEM).

SEM uses a focused electron beam to obtain an image of a sample by raster scanning its surface. The interaction of the electron beam and the sample generates interaction products which can be identified by suitable detectors. Secondary and backscattered electrons are used for imaging. Secondary electrons result from inelastic scattering between the primary electron beam and weakly-bound outer shell electrons in insulators or semiconductors or conduction band electrons in metals. Due to their low kinetic energy of typically less than 10 eV, only secondary electrons within the first few nanometers of the sample are able to escape the sample and can be detected. Therefore, secondary electrons are used for imaging the sample surface.

Backscattered electrons are produced by an elastic scattering process between the primary electron beam and the sample material. Elements with higher atomic number have a higher yield for backscattering electrons than elements with low atomic number. Hence, heavy elements appear brighter in the SEM image compared to light elements. This makes backscattered electrons especially suitable for detecting areas of different elemental composition in the sample.

Cross sections can be milled and polished with a FIB of Ga ions. The FIB cuts the sample vertically under an angle of 90° while the electron beam images the cross section from the side. For the used *Tesca Lyra 3* system, the imaging angle is 55°.

### 3.2.3 Electrical Characterization

While two-layer structures of active bottom electrode and insulating layer can be measured electrically with the CAFM setup with the Pt-coated tip acting as inert electrode, complete ECM cells are measured with a two-point probe station. Here, two tungsten needles are placed on contact pads of the top and bottom electrode with micrometer manipulators.

Two basic modes of operation can be used for the electrical characterization of ECM cells: quasi-

static voltage sweeps and voltage pulses. Quasi-static sweeps provide exact switching voltages, while voltage pulses give information on switching speed and can lead to an approximation of the amount of charge needed for the SET process. Furthermore, applications in memory devices will use voltage pulses for reading and writing to ensure fast device operation.

Quasi-static voltage sweeps are performed using a *Keithley 2400 Sourcemeter*, which can set a current compliance between 1 nA and 1.05 A with a duration of the individual voltage steps of 80 ms. All triangular voltage sweeps from 0 V to a positive voltage, back to 0 V followed by a negative sweep to a negative voltage and back to 0 V are operated with a step size of the staircase sweep of 0.01 V.

An *ArC ONE* measurement system is used for voltage pulses. The *ArC ONE* from *ArC Instruments* is specifically designed for the electrical characterization of ReRAM cells and can apply voltage pulses with an amplitude of  $\pm 12$  V and a minimum pulse width of 90 ns. All STDP measurements are performed with the *ArC ONE* measurement system. It is also able to perform voltage sweeps, but since its lowest compliance current is 10  $\mu$ A, the *Keithley 2400 Sourcemeter* is preferably used for sweep measurements.

### 3.2.4 Mechanical Characterization

The printing process offers the possibility to use flexible foils as substrates for electronic devices such as printed memory cells. However, for the targeted usage in flexible applications the device performance under bending has to be tested and evaluated. Due to the extremely broad range of possible applications, there are various different requirements for device flexibility [48]. Therefore, an apparatus testing the device flexibility has to be able to detect both the lowest possible bending radius before malfunction as well as to track the gradual device degradation caused by repetitive bending cycles. The latter is also called bending fatigue and requires an automated setup, which can guarantee uniform and reproducible bending cycles.

Several different bending apparatus have been used in literature. In a push-to-flex apparatus the sample is mounted onto a linear translation stage, where buckling of the sample leads to unguided bending [76]. Here, the bending radius can either be calculated or directly measured with a camera. For a better control of the bending radius, a roller-flex setup automatically bends the sample over a cylinder with a fixed diameter [18]. The additional forces acting on the sample with the roller-flex apparatus can be compensated by adding a second flexible substrate in an on-belt bending setup [78]. A flex-e-test apparatus clamp the sample into grips with defined curvatures and moves over a bent surface [43]. Thus, the sample is forced to bend over the defined curvatures of the grips.[52]

According to Harris et al. [48], the ideal automated bending test setup has to fulfill the following requirements:

- achieve uniform strain over the entire sample
- guarantee controlled and reproducible bending parameters such as strain and strain rates

- minimize contact with the sample in order not to damage the tested electronic device on the substrate
- automated in situ measurement of relevant device parameters such as electrical conductivity

Except from the push-to-flex apparatus, all of the above-mentioned setups face the drawback of the device on the substrate touching the bending apparatus during compressive bending. This inhibits electrical connections to the sample needed for in situ measurements and can even damage the measured device. While the push-to-flex apparatus sufficiently meets the requirements, it cannot execute consecutive cycles of tensile and compressive bending, which can occur in various application schemes. Therefore, a novel device is constructed which meets the above-mentioned requirements and provides consecutive bending in compressive and tensile direction.

The so-called rotate-to-bend apparatus clamps the sample into grips on either side. One of the grips is fixed, whereas the other is rotatable on a circular arc as can be seen in fig. 3.6. With the memory cell on the top side of the foil, the left clamp moving downward creates a tensile strain on the cell, while an upward movement leads to a compressive strain. The angle of rotation  $\beta$  is defined as the angle between the rotated left clamp and its initial position, where the sample is not subjected to any bending deformation.  $\beta$  is defined positive for downward movement i.e. tensile strain and negative for upward movement and compressive strain. The bending rotation is performed by a stepper motor (*RB-SOY-03; 12V 0.4A 36oz-in Unipolar Stepper Motor*), which is driven by a motor driver (*RB-Ard-35; Arduino Motor Shield Rev3*) and controlled by an *Arduino* microcontroller (*RB-Ard-34; Arduino Uno R3 USB Microcontroller*). For in situ electrical measurements a thin insulated copper wire can be soldered onto the foil and connected to a *Keithley 2400 Sourcemeter* to read or write the memory cells during bending.

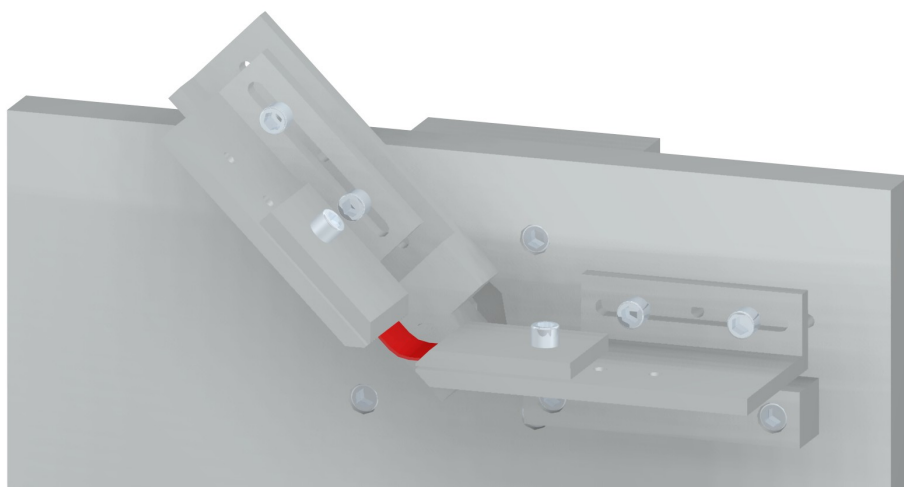


Figure 3.6: Schematic of the rotate-to-bend apparatus with the fixed right clamp and the rotatable left clamp. Both clamps are movable on their guide rail to set the spacing  $L$  between them. The bent sample is depicted in red color.[52]

The sample has to be positioned between the clamps so that the memory cell lies exactly in the center between the clamps, where the minimum bending radius  $r$  occurs at the apex of the bent substrate. The bending radius is then a function of the angle of rotation  $\beta$  and the distance between the clamps  $L$  which is the length of the substrate subjected to bending. For a push-to-flex apparatus with unclamped ends of the sample, Park et al. [106] propose the following equation:

$$r(dL) = \frac{L}{2\pi\sqrt{\frac{dL}{L} - \frac{\pi^2 d_s^2}{12L^2}}} \quad (3.2)$$

, where  $dL$  is the shortening of the initial sample length  $L$  in the horizontal linear stage due to the bending and  $d_s$  is the substrate thickness. Although this formula describes an unguided bending with an unclamped substrate, it can still be applied to the setup where the substrate is tightly clamped in the grips. The bending in the rotate-to-bend setup is very similar to free bending, because the clamps fixing the substrate are rotated as well and follow the rotational motion. However, while the linear stage of a push-to-flex setup is determined by  $dL$ , the determining variable for the rotate-to-bend apparatus is the angle of rotation  $\beta$ . Therefore, formula 3.2 has to be changed to be a function of  $\beta$ :

$$r(\beta) = \frac{L}{2\pi\sqrt{(1 - \sin(\frac{180^\circ - |\beta|}{2})) - \frac{\pi^2 d_s^2}{12L^2}}} \quad (3.3)$$

The middle plane of the substrate is subjected to the bending radius  $r$ . Hence, for tensile or compressive bending, half of the substrate thickness has to be added or subtracted to obtain the exact bending radius acting on the printed memory cell lying on the substrate. However, for substrate thicknesses not exceeding 125  $\mu\text{m}$ , this effect is insignificant and not taken into account. Therefore, for positive and negative values of  $\beta$  only the absolute value is considered.

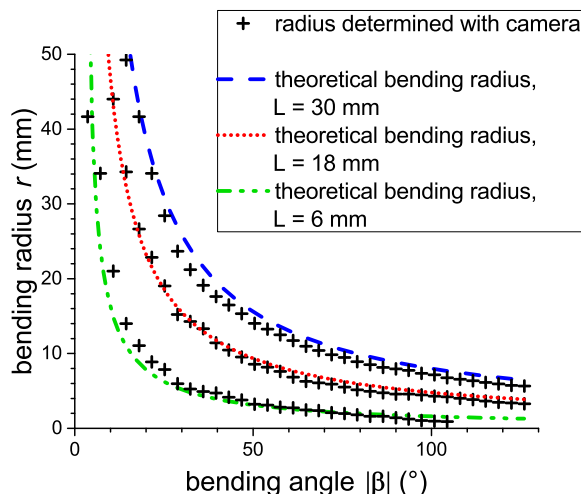


Figure 3.7: Comparison of the theoretical bending radius given by equation 3.3 with the experimentally determined values for a distance between the clamps  $L$  of 6, 18, and 30 mm.[52]

Equation 3.3 is experimentally validated by comparing the calculated bending radius with experimentally measured values detected with a camera. Therefore, a *UI-1550LE-C-HQ* camera is placed in front of the sample in line with the center point of rotation. A measurement rod next to the bent sample serves as reference to measure the sample's curvature by fitting circles in the bent curvature in the camera recordings for varying  $\beta$ . The direct comparison between theory and experiment for three different  $L$  of 6, 8, and 30 mm can be seen in fig. 3.7 and shows good agreement.[52]



# Chapter 4

## Results and Discussion

The main scope of this thesis is to show the feasibility of inkjet-printing fully functional resistive memory cells. After the first successful feasibility study, various cell architectures are designed to meet specific requirements of different applications. An Ag nanoparticles/SOG/PEDOT:PSS cell structure provides high endurance, good degree of flexibility, and a strong potential for multi bit data storage due to the high resistance window between HRS and LRS [51]. Two architectures are optimized to ensure a high degree of transparency for possible applications in transparent electronics: a PEDOT:PSS/Ag nanoparticle seed layer/SOG/PEDOT:PSS structure replaces the opaque Ag bottom electrode with a transparent layer of PEDOT:PSS and a sparse layer of Ag nanoparticles [53]. A second approach changes the dense Ag nanoparticle bottom electrode for a transparent mesh of Ag nanowires. The nanowire tracks ensure high transparency and further show an even improved resilience against bending fatigue [52]. Specific applications, where memory cells are integrated in structures with temperature-sensitive components, require a fabrication process without high temperature sintering steps.  $\text{WO}_3$  nanoparticles can serve as sinter-free insulating layer and combined with already existing sinter-free Ag nanoparticle inks and PEDOT:PSS electrodes could enable completely sinter-free memory cells [15][96].

Both quasi-static and pulsed measurements are used to determine the switching characteristics. Switching the cells using CAFM and a subsequent FIBSEM cross section illuminates the filamentary type of switching. A retention analysis tracks the diffusion of the Ag filament and fits it into a model. Finally, mechanical bending tests show the device performance under bending deformation. The fabrication parameters (type of substrate, printing and sintering parameters, etc.) are referred to as "fabrication protocols A, B,.." and are described in detail in Appendix A.

### 4.1 Resistive Switching in Printed Ag Nanoparticles/ Spin-on-glass/ Polymer Cells

Sputtered as well as thermally evaporated  $\text{SiO}_2$  is already well established as insulating layer for ECM cells [127][117].  $\text{SiO}_2$  is an excellent electric insulator, but can still act as matrix for the filament formation due to a sufficient ionic conductivity [129]. SOG, which condenses into a  $\text{SiO}_x$  layer, has been developed to resemble the characteristics of  $\text{SiO}_2$  layers and can therefore

also be used for ECM operation [94].

The printed and sintered Ag nanoparticle line acts as active electrode. Since the nanoparticles are well connected due to the sintering process, its behavior is comparable to an evaporated or even a bulk electrode. The printed PEDOT:PSS acts as inert top electrode.

A possible alternative switching mechanism would be switching through a thin natural oxide layer on top of the silver electrode [33]. Therefore, Ag/PEDOT:PSS control structures without the insulating SOG middle layer are fabricated as reference cells. Since these cells feature short-circuits, AgO-switching can be excluded and the SOG middle layer is necessary for the filament growth.[51]

#### 4.1.1 Spin-on-glass Characterization

The insulating layer in an ECM cell and its electron and ion conductivity are crucial for the filament growth and dissolution. Therefore, the structuring of the insulator can influence switching parameters such as the amount and ratio of ionic and electronic currents before, during, and after the SET process. The structuring of the SOG can be mainly controlled by its curing temperature.

The methylsiloxane *Honeywell Accuglass<sup>TM</sup> T-11 111* SOG serves as SOG layer for almost all experiments. Only the transparent cell structure PEDOT:PSS/Ag nanoparticle seed layer/SOG/PEDOT:PSS is fabricated with the phosphosilicate *Honeywell Accuglass<sup>TM</sup> P-5S*. Hence, all the subsequently described measurements refer to the *Honeywell Accuglass<sup>TM</sup> T-11 111* SOG, although the *Honeywell Accuglass<sup>TM</sup> P-5S* supposedly shows the same qualitative behavior.

Honeywell recommends a curing temperature of 425°C for both types of SOG. However, common foil substrates such as poly(ethylene terephthalate) (PET) or poly(ethylene 2,6-naphthalate) (PEN) usually cannot withstand temperatures higher than 200°C. Therefore, the influence of the SOG curing temperatures on its structuring and the switching parameters of complete memory cells is investigated. This investigation is only done with the mainly used SOG, Accuglass<sup>TM</sup>T-11 111, but could in principle be similar for the Accuglass<sup>TM</sup>P-5S as well. Fig. 4.1(a) shows the dependence of the SOG's refractive index on its curing temperature. In order to achieve a homogeneously thick SOG layer, it is spin-coated on 2.5 x 2.5 cm<sup>2</sup> pieces of Si substrate and cured for one hour under nitrogen atmosphere at different curing temperatures. The refractive index is determined using a *Plasmos SD2000* ellipsometer. The SOG's refractive index linearly decreases with increasing curing temperature and for curing as low as 100°C almost reaches 1.46, the value for stoichiometric SiO<sub>2</sub>. The refractive index of 1.41 for a curing temperature of 400°C is close to the value given by the manufacturer, which is 1.39 for 425°C. The linear dependence of the refractive index on the curing temperature is caused by outgassing of organic components such as methyl groups or remaining solvents of the SOG layer at higher temperatures. The outgassing results in a nanoporosity of the SOG and thus lowers the refractive index of the layer [104].[51] Fig. 4.1(b) shows the switching voltage  $V_{SET}$  plotted against the SOG curing temperature for fully printed cells (fabrication protocol A). Here, the cells are fully printed with an Ag nanoparticles/SOG/PEDOT:PSS layer structure on Si wafers with a 100 nm thick thermal SiO<sub>2</sub> insulating

layer. The printed SOG layer is again cured for one hour under nitrogen atmosphere. Although the curing temperature influences the refractive index and structuring of the SOG, it has no effect on  $V_{\text{SET}}$ . Other switching parameters such as the resistance of HRS and LRS are also not affected. This can be explained by the fact that filament growth takes place equally in stoichiometric defects of the SOG for low curing temperatures as well as in nanopores for high curing temperatures. Since the curing temperature does not affect the switching parameters, it can be set lower than the recommended 425°C and be adjusted to the heat resistance of the foil substrate. For the mostly used PEN substrates with a temperature stability of up to 230°C the SOG is cured at 200°C.[51]

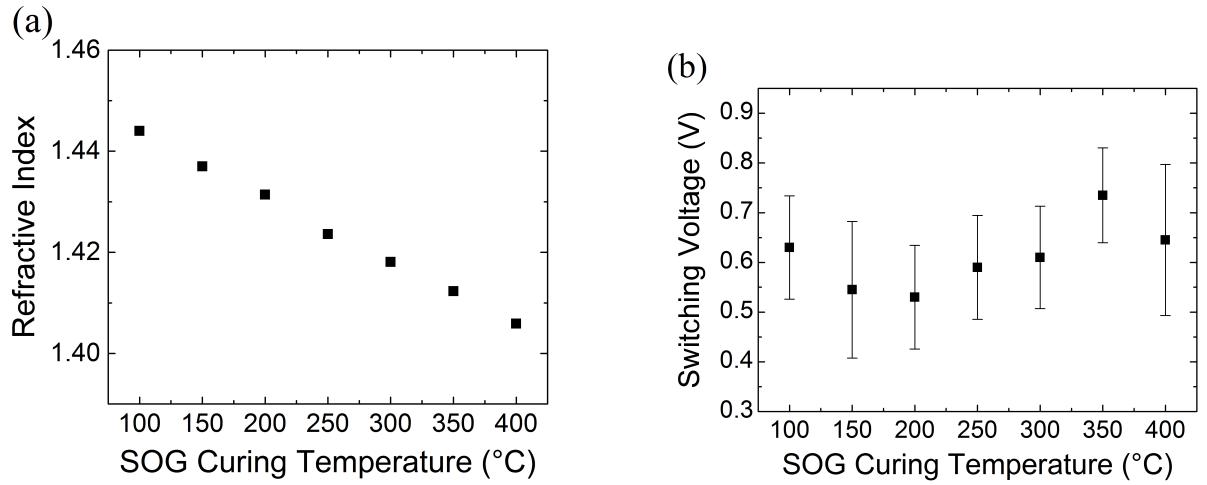


Figure 4.1: (a) Refractive index of spin-coated SOG plotted against the curing temperature. At higher temperatures, organic contents evaporate and lead to a nanoporous SOG layer with lower refractive index. (b) The SET voltage for quasi-static measurements of printed Ag/SOG/PEDOT:PSS cells does not show a significant dependence on the SOG's curing temperature [51].

#### 4.1.2 Quasi-Static Electrical Characterization

In a functional device, where fast operation is important, a memory cell will always be switched and read out by short voltage pulses. However, a quasi-static voltage sweep gradually ramps the voltage in a staircase function and reveals crucial switching parameters: the switching voltage  $V_{\text{SET}}$  from HRS to LRS, the negative switching voltage  $V_{\text{RESET}}$  from LRS to HRS, the resistance values of HRS ( $R_{\text{OFF}}$ ) and LRS ( $R_{\text{ON}}$ ), and the preset current compliance  $I_{\text{cc}}$ . Fig. 4.2(a) shows a typical current-voltage measurement of a fully printed Ag/SOG/PEDOT:PSS cell structure (fabrication protocol B). The sweep goes from 0 V to 1 V, then down to -0.2 V, and back to 0 V with a step size of 0.01 V. The cell switches to the LRS at a voltage of 0.39 V, where it directly reaches the current compliance of 1  $\mu\text{A}$ . At a voltage of -10 mV the cell switches back into the HRS. The linear slopes of fig. 4.2(a) give the resistance values, which can be more easily extracted from the resistance-voltage curve in fig. 4.2(b):  $R_{\text{OFF}}$  is above 1 G $\Omega$  and represents the extremely low amount of leakage current through the SOG layer. This value already exceeds

the detection limit of the analyzing source measuring unit and is therefore also subjected to measurement noise.  $R_{ON}$  is 106 k $\Omega$  for the given current compliance.

It is worth noticing that the applied voltage never reached a value above 0.39 V, although the voltage sweep was programmed to reach 1 V. This is due to the preset current compliance: when the cell resistance drops to 106 k $\Omega$  during SET, Ohm's law only allows an applied voltage of  $V_{max} = 0.11$  V if the current compliance of 1  $\mu$ A shall not be exceeded. The maximum applied voltage is given by  $V_{max} = R_{ON}I_{cc}$ . All the voltage steps in the measurement which cannot be reached due to this compliance are usually all measured at the voltage  $V_{max}$ . Thus, fig. 4.2 shows the values of current and voltage as they are measured in reality. However, data shown in literature is often shown in a more idealized presentation with increasing voltage values in the current compliance [137][128]. Fig. 2.2 also uses the idealized depiction.

It has to be noted that contacting polymer structures often leads to non-ohmic connection with a high contact resistance. Therefore, polymer contact pads are coated with conductive *Acheson G 3692* silver paint to improve the contact for all further measurements.

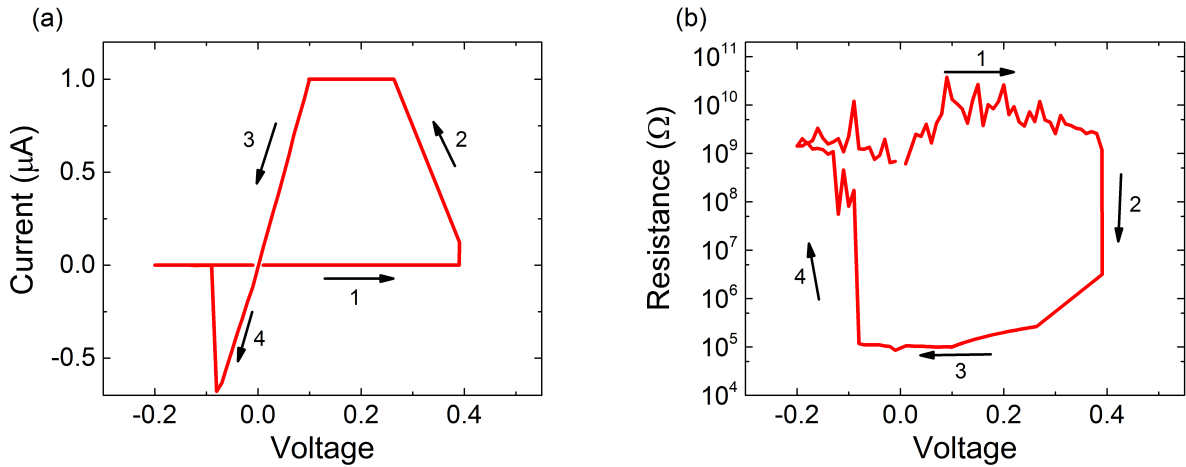


Figure 4.2: (a) Quasi-static current-voltage and (b) resistance-voltage measurements of an Ag/SOG/PEDOT:PSS cell with a current compliance of 1  $\mu$ A.

The endurance describes the maximum amount of possible switching cycles before device failure and represents an important parameter of a data storage device. In nowadays memory devices it can range from  $10^3$  for flash memory to values up to  $10^{17}$  for Dynamic RAM. While ReRAM devices already show endurance values of  $10^{12}$ , cells based on the ECM mechanism with an endurance of  $10^6$  have been reported, but usually show lower endurance in the range of  $10^3$ - $10^4$  [72][19]. The endurance test depicted in Fig. 4.3 shows stable switching operation for more than 1000 switching cycles. Each endurance cycle is a quasi-static voltage sweep from 0 V to 3 V, down to -0.2 V, and back to 0 V with a current compliance of 10  $\mu$ A (fabrication protocol B). For each data point,  $R_{OFF}$  is extracted at -0.2 V, while  $R_{ON}$  is the mean value of all I-V measurements of the cell in the current compliance. The SET Voltage increases with higher cycle

number until 3 V does not suffice for the SET process anymore at approximately 1100 switching cycles. After the endurance test the cell switches into the LRS again at 5.5 V.[51]

It is worth mentioning that the wear of the cells during quasi-static endurance measurements is considerably higher compared to pulsed switching, since a quasi-static voltage sweep can be seen as a step-function of individual pulses. Therefore, the endurance could be higher when pulsed switching is used.

A failure analysis shows that typically more than 80 % out of a batch of fully printed memory cells is fully functional. The malfunctions are mainly caused by short-circuits between bottom and top electrodes due to a flawed printing process, where the SOG layer cannot cover the bottom electrode completely. Most likely, these short-circuits are located at individual elevations in the printed Ag line coming from Ag nanoparticle agglomerations or considerably larger single particles.

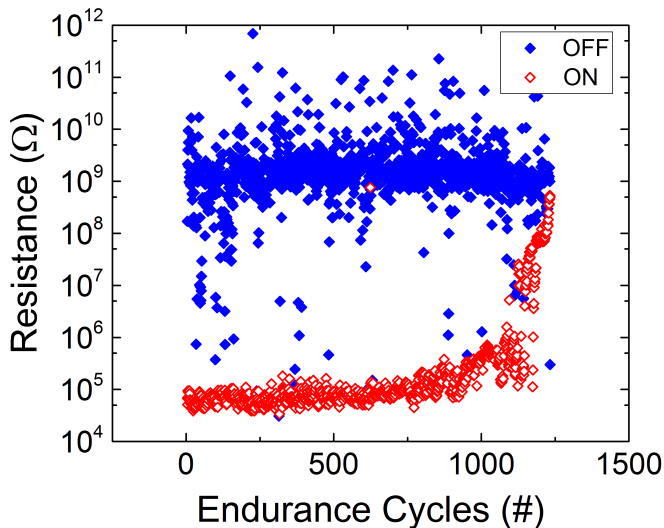


Figure 4.3: Endurance of an Ag/SOG/PEDOT:PSS cell structure using quasi-static voltage sweeps with a current compliance of  $10 \mu\text{A}$  [51].

Concerning memory density, printed electronics in general face the problem of larger lateral feature sizes compared to photolithography. While photolithography offers feature sizes in the nm range, inkjet printing cannot fall below tens of  $\mu\text{m}$  for most materials. Therefore, the option of multi bit data storage described in chapter 2.3.1 can be used for an enhancement of the memory density.

Fig. 4.4 shows the results of quasi-static voltage sweeps with  $I_{cc}$  ranging over four orders of magnitude from 10 nA to 100  $\mu\text{A}$  (fabrication protocol B).  $R_{ON}$  covers more than three orders of magnitude from 40 M $\Omega$  at 10 nA to 21 k $\Omega$  at 100  $\mu\text{A}$ . For even lower values of  $I_{cc}$  the resulting LRS becomes very unstable. The amount of Ag ions building up the filament most likely does not suffice for a stable connection for such low currents. For  $I_{cc} > 100 \mu\text{A}$  the cells are stuck in the LRS and cannot be switched back to the HRS. The filament becomes too thick to be electrochemically reversible.

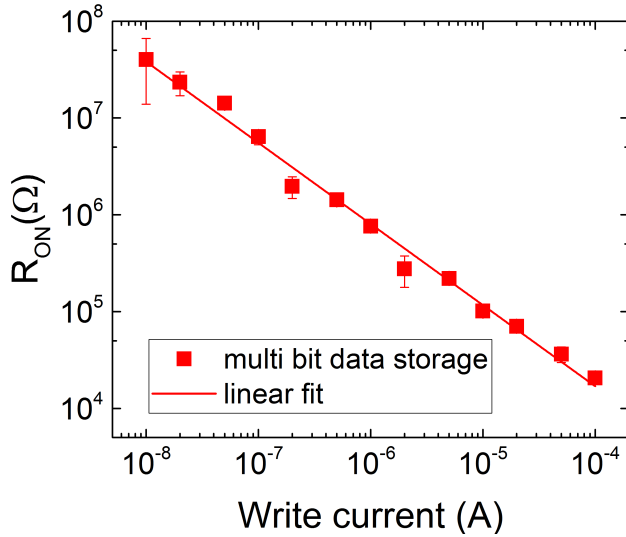


Figure 4.4: ON resistance plotted double-log against the compliance current for an Ag/SOG/PEDOT:PSS cell. The voltage sweeps range from 0 V to 3 V and back down to -0.2 V with current compliances of 10 nA to 100  $\mu$ A.

While the results of fig. 4.4 give experimental evidence for a varying filament diameter, only cutting the sample can reveal the actual filament. This can be achieved by writing the filament with CAFM and cutting the structure with FIBSEM.

#### 4.1.3 Local Filament Formation with Conductive Atomic Force Microscopy

The three-layered structure of an ECM cell with the insulator sandwiched between the two electrodes makes a direct investigation of the metallic filament impossible. Therefore, CAFM is used on two-layered structures consisting of an Ag bottom electrode covered by a SOG film. Instead of a PEDOT:PSS layer, a Pt/Ir-coated tip acts as inert top electrode. A negative voltage applied to the tip creates a local Ag filament. The change in topography and local conductivity caused by the filament can then be measured by CAFM scans. During AFM scans, samples on flexible substrates would show a deteriorated topography due to possible bending. Therefore, rigid pieces of a Si wafer covered by 100 nm of insulation  $\text{SiO}_2$  serve as substrates for all AFM measurements. After forming the filament with the CAFM the filament's cross section can be investigated using a FIBSEM system.

Fig. 4.5(a) shows a schematic of the local filament formation with CAFM. When the conductive probe is in contact with the sample and at rest (not scanning), a quasi-static voltage sweep or a constant voltage is applied on the tip while the sample is grounded. A negative voltage on the tip attracts the Ag cations and creates the filament. It is worth noticing that for a better consistency with all other current-voltage graphs shown in the thesis, the voltage polarity of the CAFM sweep measurements (see fig. 4.5(b)) is reversed. A positive voltage in the CAFM sweep

correlates to a negative voltage on the tip and vice versa. Since the three current ranges of 1 nA, 100 nA, and 10  $\mu$ A do not set an active current compliance, a compliance resistor can be set into the wiring of the sample holder. The regular conductive sample holder contains a 10 M $\Omega$  resistor. To allow a higher current flow during switching a lower resistor can be soldered into the wiring using a different holder.

A typical local current-voltage sweep with a current range of 1 nA and a 1 M $\Omega$  compliance resistor is shown in fig. 4.5(b). The sample consists of a 100 nm thick bottom electrode of thermally evaporated Ag covered with a spin-coated SOG layer. The Accuglass<sup>TM</sup>111 SOG was spin-coated and sintered at 200°C. Since the spin-coated SOG with a thickness in the range of 100 nm would require too high forming voltages, the layer was thinned with 10 % HF to a thickness of 40 nm. The cell switches into the LRS at  $V_{SET} = 4.1$  V and switches back at  $V_{RESET} = 13$  mV.  $V_{SET}$  in the CAFM measurements is considerably higher than  $V_{SET}$  obtained with a two-point probe setup on cells with a top electrode, although the thickness of the SOG is similar. This is possibly caused by the fact that for the local filament formation with CAFM the filament has to be formed through the full 40 nm SOG thickness. For the fully printed cells with a surface-covering top electrode, the effective thickness of the 40 nm SOG covering the rough, printed Ag layer is thinner at spots with a large roughness due to imperfect SOG coverage. Therefore, for the complete cells with three layers the filament has to be formed through an effectively thinner SOG layer thickness and the forming voltage is smaller compared to the CAFM sweeps.

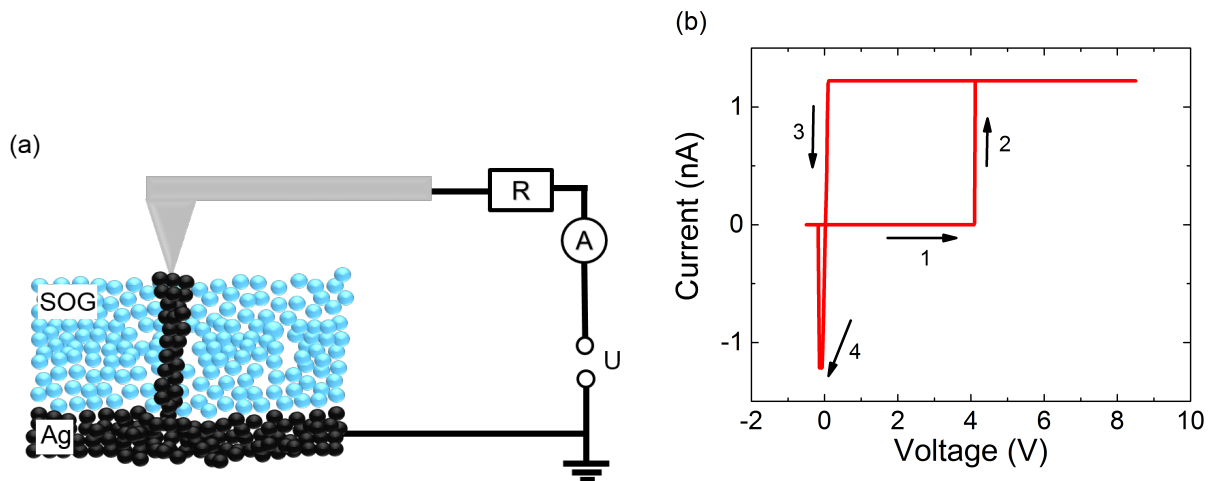


Figure 4.5: (a) Schematic of the CAFM setup with the tip touching the Ag/SOG layer stack and creating an Ag filament. The sample is grounded and a negative voltage on the tip leads to the filament formation. (b) Typical current-voltage characteristic with a current range of 1 nA and a 1 M $\Omega$  compliance resistor. The voltage polarity was changed in the graph for better consistency throughout the thesis. A positive voltage in the CAFM current-voltage curve corresponds to a negative voltage on the tip and vice versa.

The changing topography and conductivity coming from the local filamentary switching can be seen in fig. 4.6 (fabrication protocol A without polymer top electrodes and a SOG sintering tem-

perature of 200°C).

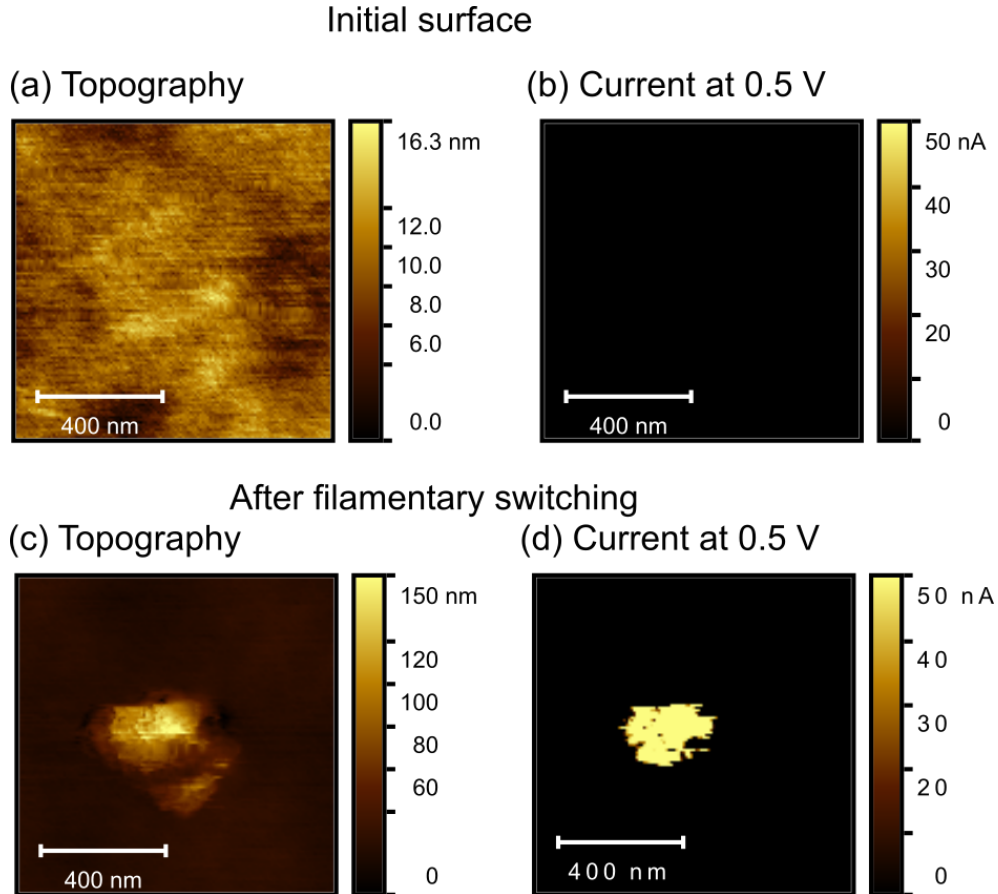


Figure 4.6: Local filament formation in printed Ag/SOG structures. (a) Topography of the flat surface with a root mean square of 2.23 nm and (b) current image at a tip voltage of 0.5 V showing the insulating SOG. (c) Topography after filament formation in the middle of the scan area with a voltage sweep from 0 V to -9.9 V and back to 0 V with a current range of 100 nA and a compliance resistor of 10 MΩ. (d) Current image at 0.5 V demonstrating electrical conductivity of the created filament hillock. All four scans have an area of 1  $\mu\text{m}$  x 1  $\mu\text{m}$  and contain 127 x 127 pixels. Graph adapted from [96].

The area scan of fig. 4.6(a) is taken on a printed Ag line covered with SOG and shows a smooth surface with a root mean square of 2.23 nm. A voltage of 0.5 V applied to the tip results in the current image of fig. 4.6(b) and confirms the excellent insulating behavior of the SOG layer. Only a setup-related noise current of a few pA is detected. After this initial CAFM scan the tip is placed in the middle of the scan area and subjected to a quasi-static voltage sweep from 0 V to -9.9 V and back to 0 V with a current range of 100 nA and a compliance resistor of 10 MΩ. A local Ag filament forms at the tip position and in the subsequent CAFM scan (fig. 4.6 (c)) a filament hillock at the position of switching appeared. The hillock has a height of approximately 150 nm and a diameter of ca. 400 nm and most possibly consists of Ag atoms which breached the SOG surface and formed the first electrodeposit. This is supported by the current image depicted in fig. 4.6 (d), which shows electrical conductivity for the center of the

filament hillock. The outer part of the filament hillock not contributing to the current signal is probably Ag which is still covered by SOG. There, the Ag electrodeposit could have lifted the SOG causing the change in height, but possibly does not break through the surface of the SOG and thus does not contribute to the current signal. The maximum current of 50 nA is directly related to the  $10 \text{ M}\Omega$  compliance resistor at 0.5 V scanning voltage, ergo the resistance of the filament must be much smaller than  $10 \text{ M}\Omega$ .

During the switching process and local filament formation, the tip does not have to be at rest. Instead, it can scan the surface in a defined pattern with a fixed applied voltage and form an array of filaments on the sample. This feature can be used to inscribe the logos of the INRS as well as the Munich University of Applied Sciences on a spin-coated layer of SOG on Ag (see fig. 4.7). This inscribing of filament arrays demonstrates the randomness of the filament generation, i.e. the fact that the filament can be generated anywhere on the Ag/insulator surface.

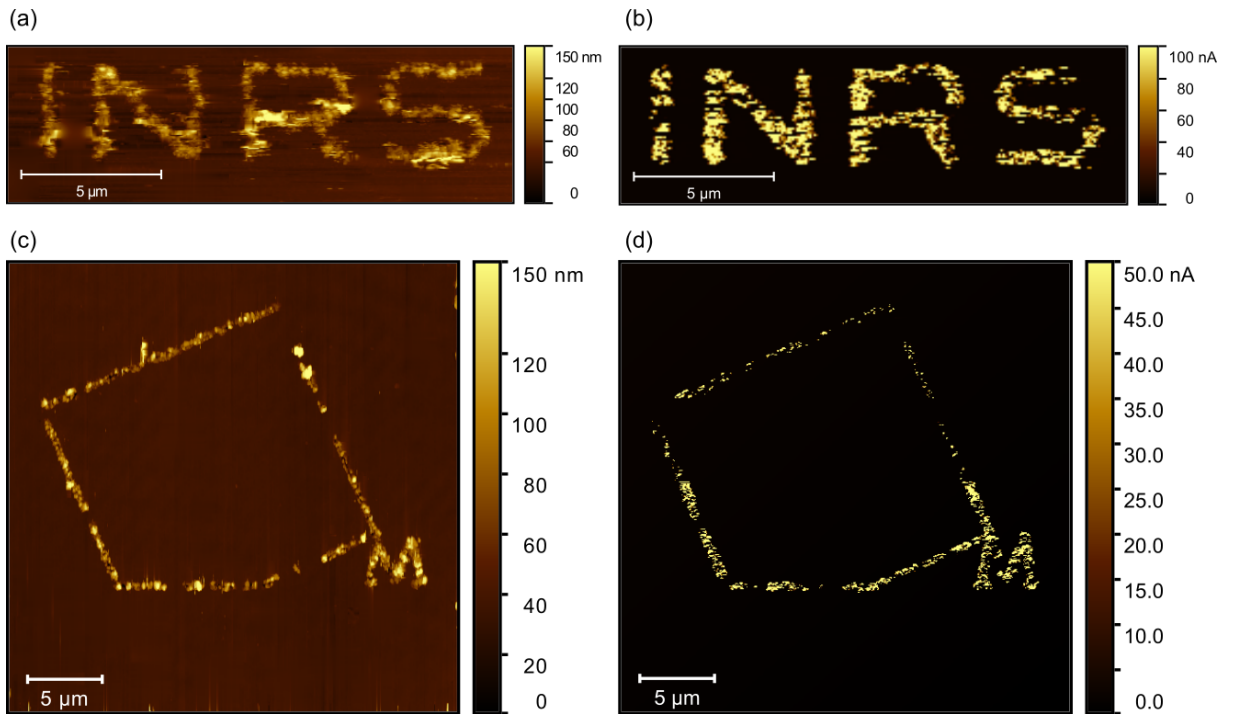


Figure 4.7: Lines of conductive filaments in the shape of the logos of (a) and (b) the INRS and (c) and (d) the Munich University of Applied Sciences. The filaments are switched with a constant voltage of -9.9 V, a current range of  $10 \mu\text{A}$  and a compliance resistor of  $10 \text{ M}\Omega$ , while the tip moves over the surface with a speed of  $0.1 \mu\text{m s}^{-1}$ . Graph adapted from [96].

The writing of filament arrays is also essential for the investigation of the filament's cross section using FIBSEM: a single filament inscribed with the CAFM system can hardly be found and detected with SEM due to the small lateral dimensions of the filament on the much larger insulator surface. Additionally, cutting the filament exactly in the middle to reveal its cross section is extremely challenging. Most possibly, the milling and polishing process of the cross section with the Ga beam leads to the complete removal of the filament. Therefore, a line of filaments

is inscribed with CAFM and the sample is cut in perpendicular to the line with the Ga beam of the FIBSEM. This procedure ensures that the cross section reveals the cut of the filament and does not remove it completely instead.

A FIB cut shows the cross section of the Ag/SOG layers in fig. 4.8(a) and (b). Prior to cutting the sample a Pt protection layer is deposited with a gas injection system directly on top of the area of the cut. It enhances the cutting accuracy and edge sharpness of the cross section which is limited by the Gaussian beam shape of the FIB beam [27]. The surface image of the cross section given by the secondary electron beam can be seen in fig. 4.8(a). The printed Ag layer does not form a dense and uniform layer, but contains voids caused by the densification of the sintering process. The fact that the Pt layer does not fill up the voids shows the complete coverage of the Ag with SOG. The back scattered electron scan in image (b) gives a more distinct material contrast between the SOG and the Ag. The higher atomic number of Ag compared to Si and O in the SOG creates more back scattered electrons and therefore appears brighter in the image.

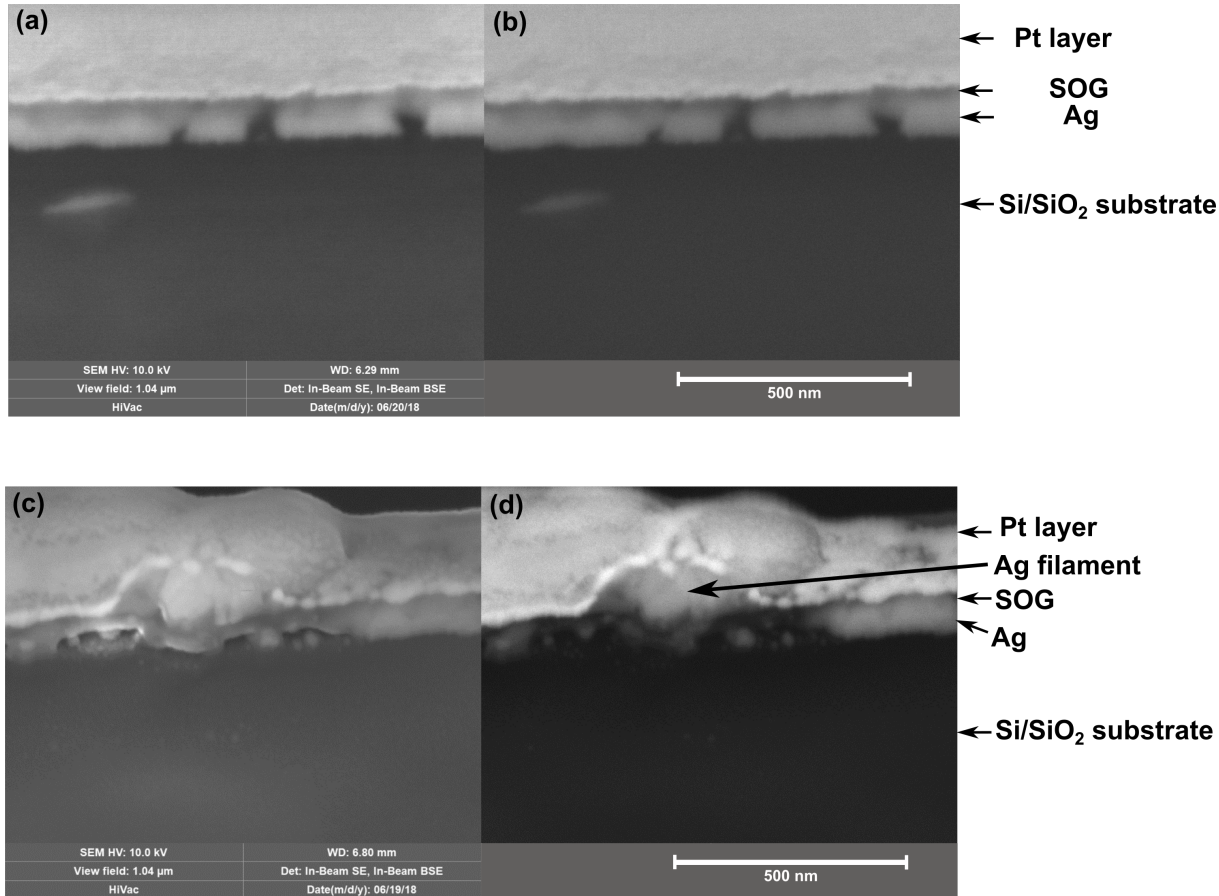


Figure 4.8: (a) Secondary electron and (b) back scattered electron image of the cross section of the Ag/SOG layer structure on a Si substrate with a 100 nm thick SiO<sub>2</sub> insulating layer. (c) Secondary electron and (d) back scattered electron image of an Ag filament switched through the SOG with CAFM. A line of filaments is switched with the CAFM tip at -9.9 V moving over the surface with  $0.1 \mu\text{m s}^{-1}$ . The FIBSEM cross section is taken perpendicular to the filament line. A Pt protection layer is deposited on the sample prior to cutting with the FIB beam.

Fig. 4.8 (c) and (d) show the cross section of the Ag filament written by CAFM as a line perpendicular to the cross section at a constant tip voltage of -9.9 V and a current range of 10  $\mu\text{A}$  scanning the surface at  $0.1 \mu\text{m s}^{-1}$ . The filament hillock on top of the SOG is pronounced with a diameter of approximately 200 nm. It consists of Ag, which broke through the SOG layer and got deposited on top of it during the switching process by the CAFM tip. In the back scattered electron image (d) it can be seen that the filament consists of Ag which migrated from the Ag bottom electrode. The printed Ag bottom electrode shows distinct voids directly next to the filament, where the Ag is consumed and gaps are left instead. For all FIB cuts, the FIB emits a current of 40 pA for the first, coarse milling and less than 1 pA for polishing the side cut.

#### 4.1.4 Retention Analysis

For non-volatile memory applications the maximum retention time is a crucial parameter. It describes the time period over which a memory can maintain its logical state before spontaneously switching back without any external switching command. In a memory device, this would cause undesirable data loss. In the case of ECM, the HRS state has a virtual infinite retention time when there is no material degradation. The decisive state is the LRS condition, where the Ag filament is prone to spontaneously dissolve in the insulating layer. This dissolution results in an undesirable setback to the HRS state. The following subsection focuses on this filament diffusion process and fits the change of the dissolving filament with the Fick diffusion model given in subsection 2.3.3.

The amount of time until an Ag filament is dissolved and ruptures is closely related to its thickness. A thicker filament takes more time until it is fully dissolved and therefore allows longer retention time of the memory cell. This behavior is investigated by applying voltage pulses to a printed Ag/SOG/PEDOT:PSS cell using the *ArC One* system (fabrication protocol B). Positive voltage pulses without any current compliance but varying width and amplitude switch the cell from HRS to LRS. Longer pulse width and higher voltage amplitude result in a lower ON resistance (see fig. 4.9(a)). The underlying mechanism is similar to the multi bit data storage depicted in fig. 4.4, where the ON resistance depends on the current compliance of the quasi-static voltage sweep. For the pulsed measurements, the width and amplitude of the voltage pulse define the amount of ionic currents flowing during the SET operation and thus determine the thickness of the Ag filament. The higher the pulse width and amplitude, the thicker the metallic filament. A thicker filament leads to a lower ON resistance and a longer retention time. Fig. 4.9(b) shows the resulting retention time based on the same measurements depicted in fig. 4.9(a). Periodical read pulses after the SET process give information on the retention time. The read pulses are 3 ms long with an amplitude of 0.2 V. A pulsed read voltage of 0.2 V is low enough to ensure no impact on the cell due to the read out. Since the resistance gradually increases, a threshold resistance of 500 k $\Omega$  is set for the determination of the retention: the time when the cell resistance reaches a value above 500 k $\Omega$  is declared as maximum retention time.

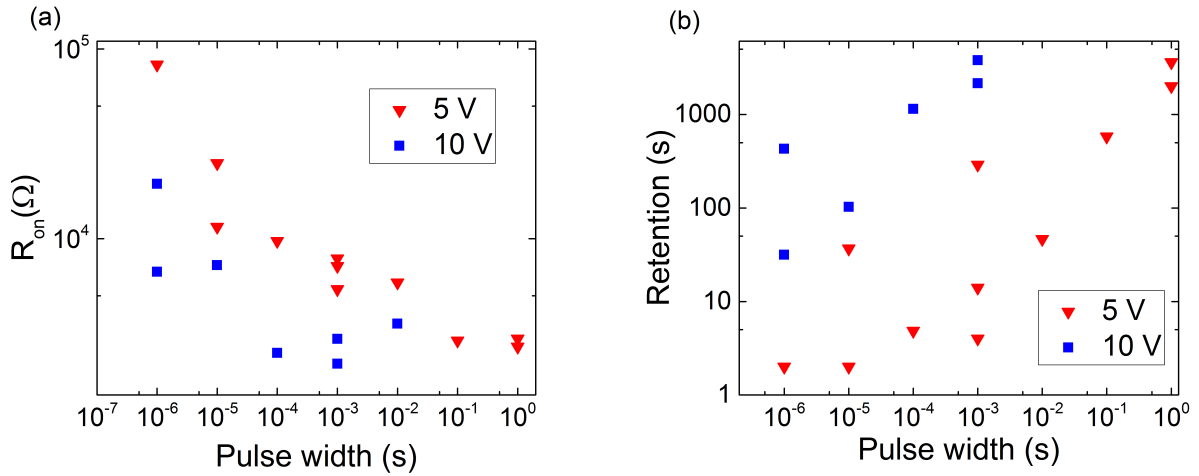


Figure 4.9: Voltage pulses without current compliance applied to a printed Ag/SOG/PEDOT:PSS cell. (a) ON resistance plotted double-log against voltage pulse width: longer pulse width and higher pulse voltage lead to a thicker Ag filament and thus to a lower ON resistance. (b) Retention time versus pulse width (double-log): a thicker filament caused by longer pulse width and higher pulse voltage is more stable against diffusion and therefore shows a longer retention time.

The time-resolved filament diffusion process can be seen in fig. 4.10 (fabrication protocol B). The cell is switched into the LRS with an initial resistance of  $1860 \Omega$  by using a 1 s voltage pulse of 12 V at  $t = 0$  s. Directly after this filament formation, the Ag filament is subjected to isotropic diffusion of Ag atoms and its diameter gradually decreases. The resulting increasing resistance  $R(t)$  is measured with read voltages of 0.5 V over a time period of more than 40000 s.  $R(t)$  in fig. 4.10 is fitted in accordance with equation 2.5 based on the diffusion process with following formula:

$$R(t) \propto A + \frac{1}{\frac{1}{B} \sum_{n=1}^{10} \frac{4}{\alpha_n^2} e^{C\alpha_n^2 t}} \quad (4.1)$$

, with the three fitting parameters  $A$ ,  $B$ , and  $C$ . It is worth noticing, that whereas the sum in the denominator in equation 2.5 goes to infinity, it is already stopped at  $n = 10$  in formula 4.1. Since the exact value of the roots of the Bessel function  $\alpha_n$  can only be determined numerically, it is practically not possible to perform the sum to infinity. However, the fast convergence of the sum allows stopping at  $n = 10$ , where the values for  $\alpha_n$  are taken from reference [30].  $A$  corresponds to the wiring resistance of the two electrodes and is separately measured as approximately  $1600 \Omega$ . Some error in  $A$  is attributed to the fact that the exact location of the filament location and therefore the exact length of the contributing electrode lines cannot be determined.  $B$  is the filament resistance directly after switching ( $R_{\text{fil}}(t = 0)$ ) and can be calculated by subtracting  $A$  from the initial resistance of  $1860 \Omega$ . Hence,  $B$  equals to  $260 \Omega$ .  $C = \frac{D}{r_0^2}$  corresponds to the diffusion constant divided by the initial filament radius squared and is determined by the fit to  $2.2 \cdot 10^{-5} \text{ s}^{-1}$ . In principle,  $r_0$  could be calculated from  $R_{\text{fil}}(t = 0)$  by using the filament length and the specific resistance of Ag. However, the filament length, which correlates with

the SOG thickness, cannot be determined to a sufficient precision due to the varying SOG coverage on the rough Ag line. Another factor of uncertainty comes with the fact that the Fuchs-Sondheimer model has to be applied on conductors with dimensions in the nanometer range in order to compensate for electrons reflected on the conductor surface [38]. The poor knowledge of the exact filament shape and surface prevents such a modeling. Therefore,  $r_0$  is estimated to approximately 100 nm based on the FIBSEM filament cross section shown in fig. 4.8. This is only a rough estimation, since the switching for the FIBSEM cut using a CAFM tip applied a compliance resistor of  $10 \text{ M}\Omega$ , whereas no current compliance is set during pulse switching for the filament generation before the diffusion experiment.  $r_0 = 100 \text{ nm}$  results in a diffusion constant of  $D = 2.2 \cdot 10^{-19} \frac{\text{m}^2}{\text{s}}$ , which is in good agreement with literature values [91]. It is worth mentioning that retention measurements as shown in fig. 4.10 sometimes feature an abrupt, stepwise increase in resistance superimposed on the gradual increase. This is most probably caused by Ag diffusion along the filament growth direction. While the Fick diffusion model only takes into account radial diffusion, Ag diffusion along the filament can change the shape and resistance of the filament. Z. Wang et al. showed with in situ transmission electron microscopy that an Ag filament in a  $\text{SiO}_x\text{N}_y$  insulating layer will change from cylindrical into spherical shape after formation without applied voltage [136]. This diffusion process is a result of the system minimizing its interfacial energy between the insulating layer and the Ag atoms. An abrupt increase in resistance could be related to a similar diffusion process, where the galvanic contact in the filament changes to a tunneling contact between Ag spheres and abruptly increases the cell resistance.

The maximum retention time, i.e. the time until  $R_{\text{ON}}$  surpasses the threshold resistance of  $500 \text{ k}\Omega$  is  $8.65 \cdot 10^5 \text{ s}$ , which is more than 10 days.

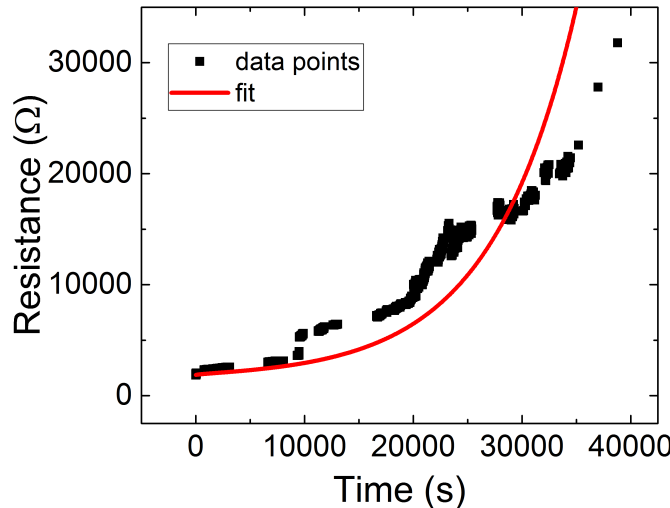


Figure 4.10: Change of the ON resistance of an Ag/SOG/PEDOT:PSS cell over time shows the gradual diffusion of the silver filament. The cell is SET with a 1 s pulse of 12 V and its resistance is periodically measured at a voltage of 0.2 V. The red line shows the fit using formula 4.1 with fixed parameters  $A = 1600 \text{ }\Omega$ ,  $B = 260 \text{ }\Omega$ , and the fitted parameter  $C = 2.2 \cdot 10^{-5} \text{ s}^{-1}$ .

#### 4.1.5 Summary and Discussion

This subsection summarizes the findings of section 4.1 on the printed Ag/SOG/PEDOT:PSS cell structure and puts them into a wider context.

First of all, the sintering temperature is found to not affect the switching behavior of the cells. This allows for sintering at temperatures as low as 100°C, which is crucial for applications on heat-sensitive foil substrates such as PET. The fully printed Ag/SOG/PEDOT:PSS cells show a  $V_{SET}$  of typically 0.4 V, a  $V_{RESET}$  of 0.1 V with  $R_{OFF}$  in the GΩ range.  $R_{ON}$  can be set between 21 kΩ and 40 MΩ depending on the applied  $I_{CC}$  and therefore offers a high potential for multi bit data storage. The cells' endurance with more than 1100 switching cycles and their retention of  $8.65 \cdot 10^5$  s is sufficient for low-cost applications of printed electronics. The retention is fitted to a diffusion model and the diffusion constant of Ag in SOG is extracted. The retention could be enhanced by reducing the diffusion constant. A yield of 80 % of all printed cells exceeds results of printed cells reported in literature [100], but could still be enhanced by improvements in the printing process such as printing a smoother bottom electrode.

The creation of single filaments with CAFM and the subsequent cross section view with FIB-SEM accesses the direct view on the filament and reveals a filament diameter of approximately 100 nm. Furthermore, this analysis shows, that the Ag bottom electrode is partially consumed during the switching process. As the CAFM experiments show, a filament can be created anywhere in the interface Ag/SOG/top electrode and therefore the partial consumption of the Ag bottom electrode can simply be compensated by creating a filament elsewhere in subsequent switching cycles. However, for cell structures with a sparse Ag seed layer as electrode, this could considerably limit the endurance.

## 4.2 Transparent Memory Cells

Transparent electronics is a fast-growing field since it enables many novel applications such as transparent displays or intelligent windows. Although the first transparent conductor has already been established in 1907 [8], the first transparent transistor has only been reported in 2003 [89]. Recently, transparent displays and even transparent photovoltaic cells have been demonstrated and offer a wide range of possible applications [50][83].

For a fully transparent device all electrical and electronic components have to be transparent and therefore the data memory, which is necessary for almost every electronic device, has to be transparent as well. Considering the three-layered structure of ECM for all different cell structures, the insulating layer usually consists of a wide bandgap insulator and hence is transparent. The inert electrode consists of PEDOT:PSS, which is already highly transparent [135]. However, the switching mechanism in ECM cells depends on a metal for the filament formation. Printed metal layers are dense and opaque structures after sintering and although they do not cover the whole area of a printed memory structure, they greatly diminish the degree of transparency. For a crossbar array with equal line and space, i.e. width of metal line and space between individual

metal lines, 50 % of the area would be covered with metal. This would diminish the maximum degree of transparency to less than 50 %. Therefore, two different cell structures replace the opaque Ag layers presented in section 4.1 with conductive, transparent layers which can still provide an Ag reservoir for the filament formation. The first approach replaces the dense Ag bottom electrode with a layer of PEDOT:PSS providing continuous conductivity covered with a sparse layer of Ag nanoparticles. The submonolayer of Ag nanoparticles acts as a seed layer for the filament formation but also provides a high degree of transparency [53]. In a second approach the dense Ag layer of sintered nanoparticles is replaced by a transparent mesh of Ag nanowires.

#### 4.2.1 Ag Nanoparticle Seed Layer

A schematic of the cell cross section with the structure PEDOT:PSS/Ag nanoparticle seed layer/SOG/PEDOT:PSS can be seen in fig. 4.11.

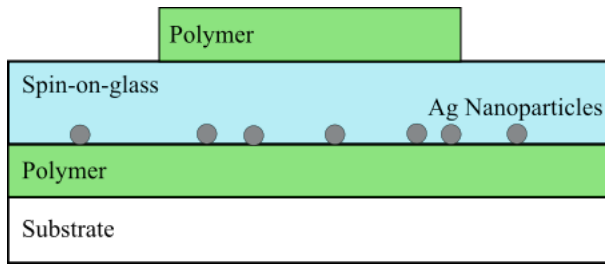


Figure 4.11: Schematic of the transparent PEDOT:PSS/sparse Ag nanoparticle seed layer/SOG/PEDOT:PSS cell structure [53].

The quasi-static current-voltage characteristics of the seed layer cells are similar to those of the cells with a dense Ag bottom electrode. Fig. 4.12 shows a typical current-voltage measurement of a seed layer cell obtained for a voltage sweep with a step size of 0.02 V from 0 V to 3 V, down to -0.5 V and back to 0 V (fabrication protocol C).  $V_{SET}$  is approximately 1.2 V and  $V_{RESET}$  occurs at ca. -0.1 V. Compared to the cells presented in section 4.1  $R_{OFF}$  with 10 M $\Omega$  to 100 M $\Omega$  is significantly lower possibly due to larger leakage currents through the Accuglass<sup>TM</sup>P-5S SOG used for the seed layer cells. Due to the more complicated cell architecture with the two-layered bottom electrode, 50 % of the seed layer cells are malfunctioning as a consequence of short-circuits. Most probably, pronounced coffee stain edges of the PEDOT:PSS bottom layer or possible Ag nanoparticle agglomerations are not fully covered with SOG and are connected to the PEDOT:PSS top electrode. The endurance of the seed layer cells is much lower compared to cells with a dense Ag electrode and typically does not exceed ten switching cycles. Since the cells stay in the OFF state and cannot be SET again, most possibly the Ag seed layer gets at least partially consumed during consecutive switching cycles and therefore no filament can be formed anymore.

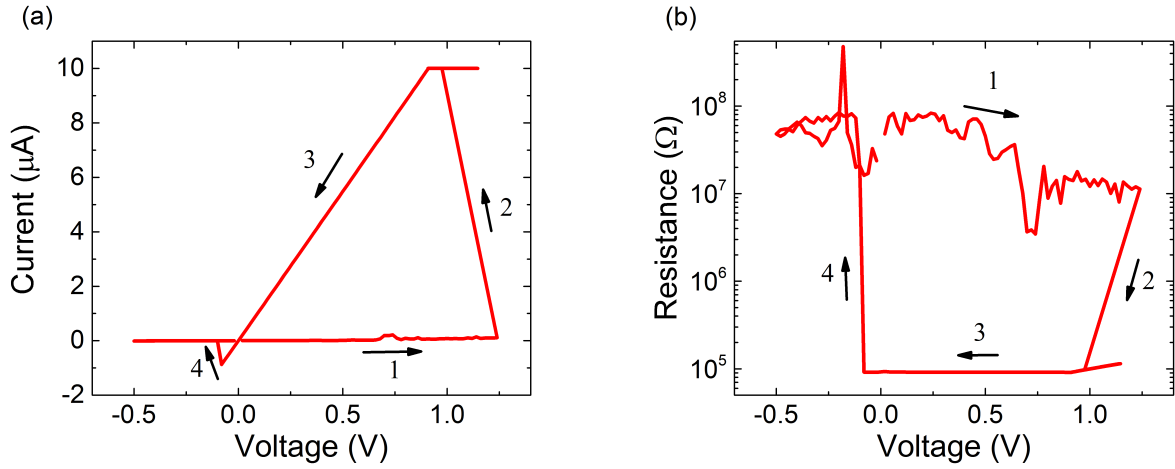


Figure 4.12: (a) Quasi-static current-voltage and (b) resistance-voltage measurements of a PE-DOT:PSS/Ag nanoparticle seed layer/SOG/PEDOT:PSS cell with a current compliance of  $10 \mu\text{A}$  [53].

To evaluate the exact degree of transparency of the memory cells, transparency measurements are performed with a *Perkin Elmer Lambda 19 UV/VIS/NIR Spectrometer*. Since the area of the printed cells is much smaller than the beam cross section used for measuring, samples are prepared by spin-coating. Therefore, the four layers of the cell PEDOT:PSS/Ag nanoparticle seed layer/SOG/PEDOT:PSS are spin-coated on a  $3 \times 3 \text{ cm}^2$  glass substrate with thicknesses similar to those of the printed cells.

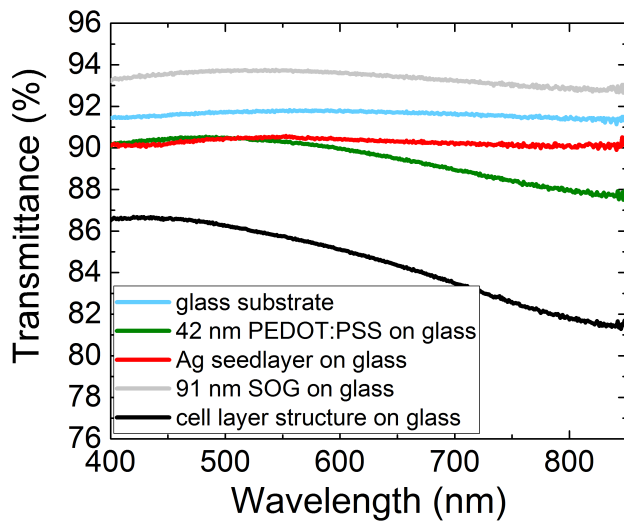


Figure 4.13: Transparency measurement of individual layers as well as the complete stack of the Ag seed layer cell structure on a glass substrate. The thicknesses of the layers are similar to those of the printed memory cells [53].

Fig. 4.13 shows the transparency of the glass substrate covered by the three different materials as well as the complete memory cell for wavelengths between 400 nm and 850 nm. It should be noted that the transparency of the glass substrate covered by the SOG layer is even higher than the one given by the glass substrate alone. Here, the SOG layer acts as anti-reflective coating with a refractive index lower than the value for the glass substrate. The complete layer stack of the seed layer cell on the glass substrate shows an overall transparency of 81 % to 87 % over the whole spectrum.[53]

#### 4.2.2 Ag Nanowire Active Electrode

Printed networks of Ag nanowires offer a reasonable compromise between electrical conductivity and optical transparency. Fig. 4.14 shows SEM images of printed Ag nanowires, which are sintered for 1 h at 140°C under N<sub>2</sub> atmosphere. The nanowires are printed on Si covered with 100 nm of thermally evaporated Au. The galvanic connection between individual nanowires due to the sintering can be seen in fig. 4.14(b). The connected nanowires form a percolated network for current flow through the structure.

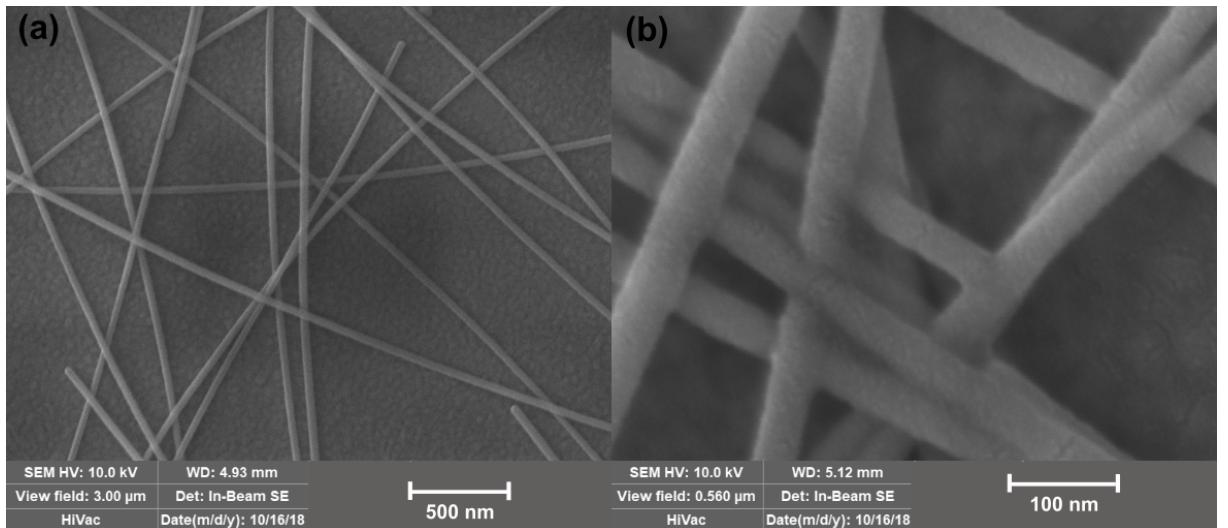


Figure 4.14: SEM images of printed and sintered Ag nanowires on a Au surface. (a) Overview of the percolating network and (b) Details of the sintered joints between the individual nanowires providing high electrical conductivity.

ECM cells with Ag nanowire bottom electrodes follow the same structure as the cells presented in section 4.1 with only the Ag nanoparticle bottom electrode replaced by nanowires. However, the nanowire bottom electrode requires changes in process steps of the SOG layer. At temperatures exceeding 150°C the Ag nanowires start melting and form individual Ag nanospheres which are not connected anymore and thus jeopardize the electrical conductivity of the Ag nanowire network. Therefore, the SOG sintering temperature has also to be limited to 140°C. Furthermore, individual Ag nanowires can protrude out of the printed nanowire network. Hence, a thicker layer of SOG has to ensure a complete coverage of the nanowires to prevent short circuits between bottom and top electrode.

The quasi-static electrical switching of Ag nanowires/SOG/PEDOT:PSS cells is similar to the one with a dense Ag nanoparticle bottom electrode as described in section 4.1. A typical current-voltage measurement of a nanowire cell can be seen in fig. 4.15 (fabrication protocol D). The voltage sweep uses a step size of 0.01 V from 0 V to 3 V, down to -0.3 V and back to 0 V with a current compliance of 10  $\mu$ A.  $V_{SET}$  is approximately 0.8 V and  $V_{RESET}$  occurs at ca. -0.1 V. The cell yield is 68 % and the maximum endurance is 218 switching cycles. After that, the cell does not switch ON again. Most probably, the Ag nanowires get gradually consumed during the switching process via diffusion and hence, the electrical connections in the bottom electrode disappear.

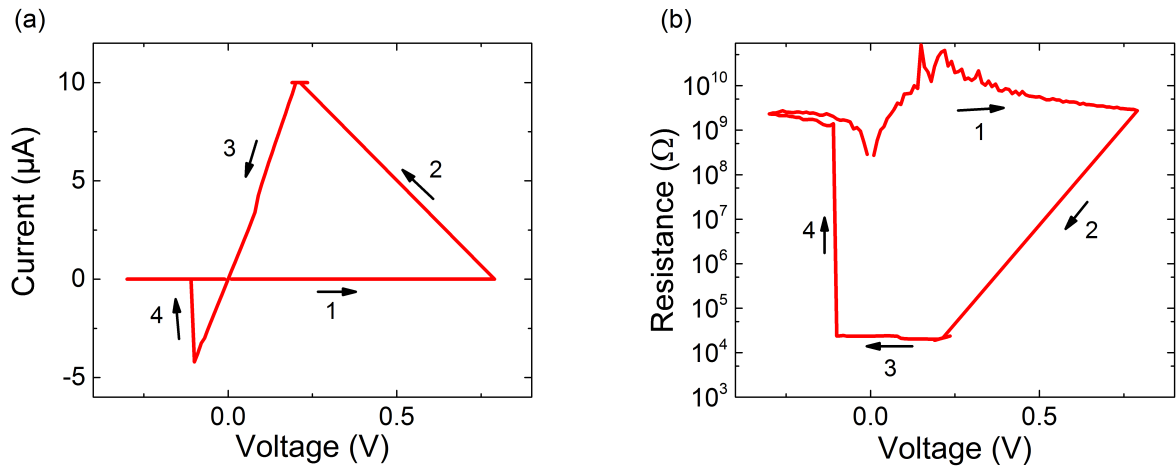


Figure 4.15: (a) Quasi-static current-voltage and (b) resistance-voltage measurements of an Ag nanowires/SOG/PEDOT:PSS cell with a current compliance of 10  $\mu$ A.

The partial disintegration of the Ag nanowires during switching can be visualized with CAFM measurements. To that end, Ag nanowire/SOG structures are fabricated on a Si wafer covered by 100 nm of SiO<sub>2</sub> (fabrication protocol D without polymer top electrode). While quasi-static voltage sweeps with the CAFM tip on top of an individual SOG coated nanowire result in resistive switching, they do not lead to a change in topography as seen with the Ag nanoparticles/SOG structure (see fig. 4.6). Most likely, the Ag reservoir of the Ag nanowires is too small to create a large filament hillock.

The fact that the Ag nanowires are partially consumed during the switching process is confirmed by the following experiment shown in fig. 4.16 : Fig. 4.16(a) and (b) show topography and current map of the Ag nanowire/SOG sample near to the edge of the SOG line. Here, small holes in the SOG due to bubble formation during the outgassing process of the solvent are visible. Ag nanowires in these holes are not covered by SOG and provide leakage current signals during the CAFM scan. After this first scan, the CAFM tip is set to -9.9 V and performs a line scan following the red square with a speed of 0.1  $\mu$ m s<sup>-1</sup>. After this line scan, the topography remains unchanged (see fig. 4.16(c)), but the current image in fig. 4.16(d) gives no electrical signal inside

the square. Most probably, nanowires crossing the contour of the square are partially consumed during the switching process during the line scan. Therefore no electrical connection to the inside of the square remains. This phenomenon confirms the partial disintegration of the Ag bottom electrode during switching and may be the limiting factor for the endurance of Ag nanowire/SOG/PEDOT:PSS cells.

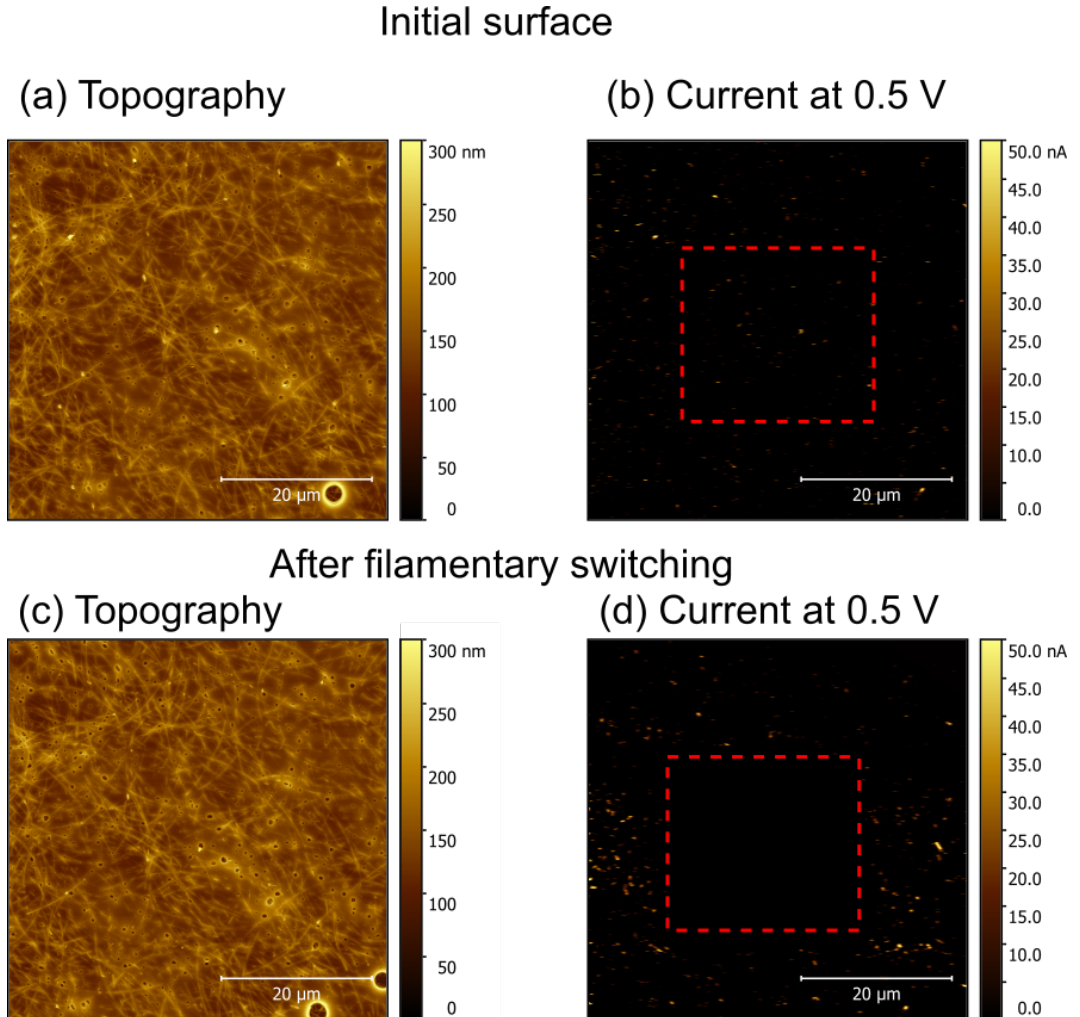


Figure 4.16: CAFM measurements showing the partial disintegration of Ag nanowires during SET in a printed Ag nanowire/SOG structure. (a) Topography of the Ag nanowire/SOG showing the nanowires through the SOG as well as individual holes in the SOG and (b) current image at a tip voltage of 0.5 V showing spots of uncovered nanowires with leakage current. (c) Topography after switching a square of filaments. The tip follows the red square depicted in (b) and (c) at a constant voltage of  $-9.9$  V, a current range of  $10 \mu\text{A}$  and a compliance resistor of  $10 \text{ k}\Omega$ . (d) Current image at 0.5 V showing the absence of spots with leakage currents inside the square. This can be explained by a partial disintegration of the Ag nanowires at the contour of the square during switching, which leaves no electrical connection to the inside of the square. The red line serves solely as guide to the eye. A drift of the sample of approximately  $5 \mu\text{m}$  occurs between the scans (a)/(b) and (c)/(d).

Transparency measurements are again performed on spin-coated layers on  $3 \times 3 \text{ cm}^2$  glass substrates. The individual layers have thicknesses similar to those of the printed layers in the memory cells. The Ag nanowire layer has an overall nominal thickness of 150 nm with single nanowires exceeding this value, protruding up to 300 nm out of the substrate. Fig. 4.17 shows the degree of transparency for the individual layers as well as for the full layer stack. The layer with the most influence on the transparency is the Ag nanowire network, limiting the transparency of the complete cell structure to 55 % to 78 % over the whole spectrum. The thickness of the nanowire layer can be adjusted for specific application in order to find a compromise between high electrical conductivity and optical transparency. It is worthwhile noticing that the overall transparency of a crossbar structure would be substantially higher than the value of the stacked layers, since most of the crossbar area is not covered by all three layers.

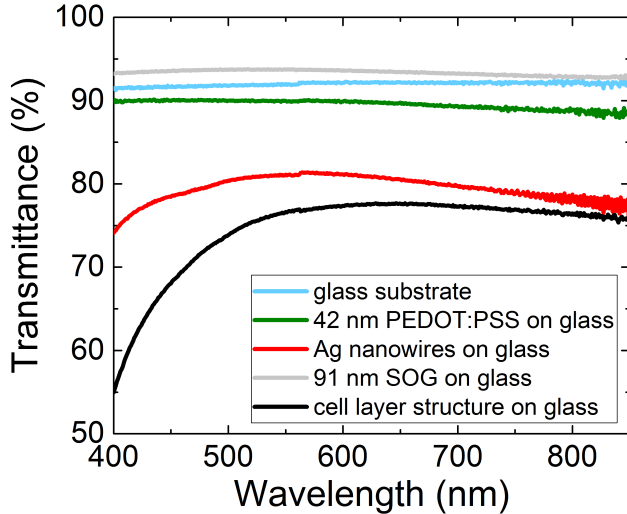


Figure 4.17: Transparency measurement of individual layers as well as the complete stack of the Ag nanowires/SOG/PEDOT:PSS cell structure on a glass substrate

#### 4.2.3 Summary and Discussion

Two transparent cell structures are presented with the bottom electrode of sintered Ag nanoparticles replaced by either a line of transparent PEDOT:PSS covered by a sparse seed layer of individual Ag nanoparticles or transparent Ag nanowires. The seed layer design provides a higher transparency of 81 % to 87 %, but suffers from a low yield of only 50 % and a low endurance of 10 switching cycles. For the Ag nanowire design the transparency is lower with 55 % to 78 %. However, a yield of 68 % and an endurance of 218 cycles outperform the seed layer cells.

Since the malfunctioning of cells is mainly caused by short-circuits, the yield could most possibly be enhanced by improving the printing process. Concerning the endurance, FIBSEM measurements on the sintered Ag nanoparticles/SOG structure (see fig. 4.8) and CAFM measurements

on the Ag nanowire/SOG design (see fig. 4.16) confirm a partial disintegration of the Ag bottom electrode during the switching process. This indicates a relationship between the degree of transparency and the number of possible endurance cycles. More Ag as nanoparticles in the seed layer or nanowires as bottom electrode lower the transparency, but can provide a larger Ag reservoir for subsequent switching. Thus, a trade-off has to be found between transparency and endurance.

## 4.3 Resistive Switching in Printed Ag/WO<sub>3</sub>/PEDOT:PSS cells

WO<sub>3</sub> has already been used as insulating layer in ECM cells. Sputtering as well as electron beam evaporation has been used to achieve dense, thin layers of WO<sub>3</sub> for ECM switching [29][79]. Recently, WO<sub>3</sub> nanoparticles fabricated by anodic treatment of a sputtered W layer have been used as ECM insulating layer for flexible memory cells [58]. However, all reported ECM layouts containing WO<sub>3</sub> still require sputtering or evaporation process steps, which is detrimental to a fast and cost-efficient process flow working on flexible substrates. Fully printed Ag/WO<sub>3</sub>/PEDOT:PSS cells are now fabricated with electrodes identical to the cells using SOG as insulating layer described in section 4.1. The change from an amorphous, dense SOG layer to a loose accumulation of crystalline WO<sub>3</sub> nanoparticles offers a simplified fabrication: unlike SOG, the printed WO<sub>3</sub> does not need a sintering step. Therefore, the usage of WO<sub>3</sub> nanoparticles as insulating layer could enable completely sinter-free printed memory cells. The PEDOT:PSS ink as inert top electrode does not require any sintering step. Even though here the *UTDots AGIJ* Ag nanoparticle ink is still used as bottom electrode with a minimum sintering temperature of 130°C, there are already sinter-free Ag nanoparticle inks, which could be equally used instead [15].

### 4.3.1 Quasi-Static Electrical Characterization

A typical quasistatic switching curve is illustrated in fig. 4.18 (fabrication protocol E). The sweep goes from 0 V to 2 V, then down to -0.3 V, and back to 0 V with a step size of 0.01 V. The cell switches to the LRS at a voltage of 0.37 V, where the sweep halts due to the current compliance of 5 μA. At a voltage of -9 mV the cell switches back into the HRS. For a write current of 5 μA,  $R_{ON}$  reaches a value of 40 kΩ, while  $R_{OFF}$  is in the range of 2 MΩ. When comparing cells using WO<sub>3</sub> as insulator with those using SOG (see section 4.1), the most prominent difference lies in  $R_{OFF}$ . While SOG as excellent insulator ensures a  $R_{OFF}$  in the GΩ range, the same cell architecture and size with WO<sub>3</sub> as insulating layer only reaches  $R_{OFF}$  in the range of MΩ. The loose and porous agglomeration of WO<sub>3</sub> nanoparticles allows a higher amount of leakage current in the HRS.

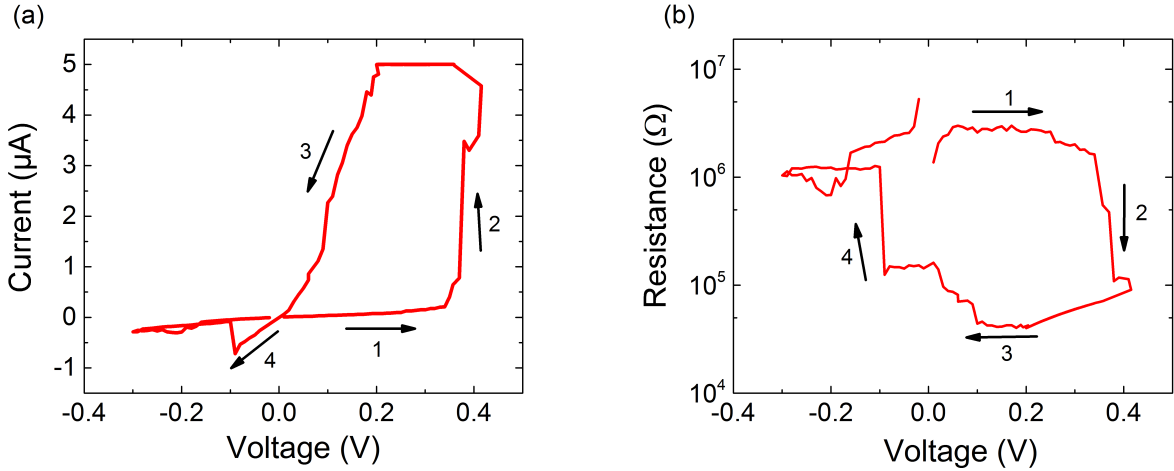


Figure 4.18: (a) Quasi-static current-voltage and (b) resistance-voltage measurements of an Ag/WO<sub>3</sub>/PEDOT:PSS cell with a current compliance of 5  $\mu$ A. Graph adapted from [96].

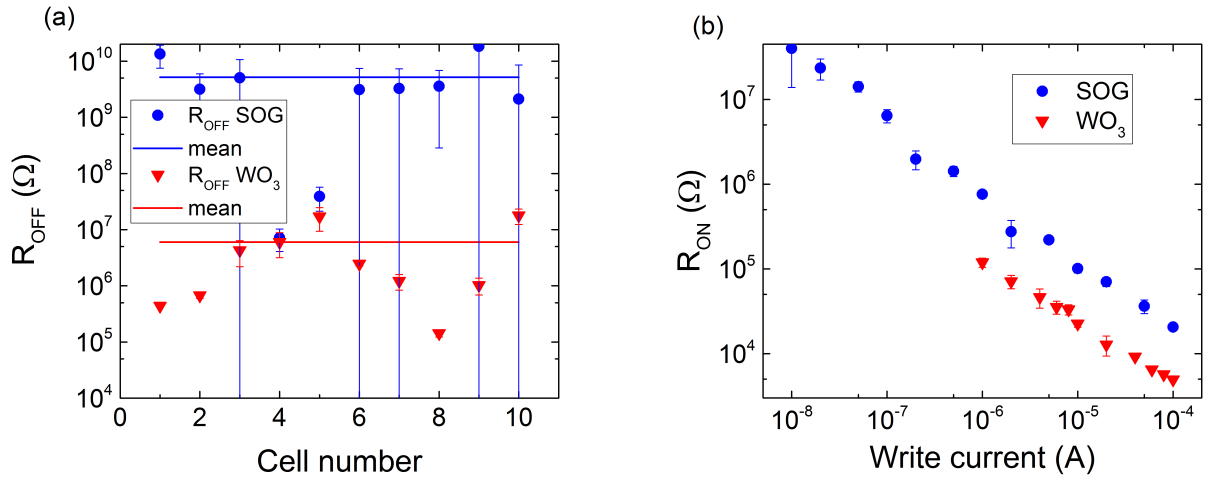


Figure 4.19: (a) Variation of  $R_{OFF}$  over 10 cells with WO<sub>3</sub> and SOG as insulating layer.  $R_{OFF}$  of the WO<sub>3</sub> cells is approximately 3 orders of magnitude lower than for cells with SOG. The large signal error for  $R_{OFF}$  of the SOG cells comes from measurement noise in the sub-nA range. (b)  $R_{ON}$  plotted against the current compliance shows that the cells with SOG can access a larger window for multi bit intermediate states due to their higher  $R_{OFF}$ . Graph adapted from [96].

Fig. 4.19(a) shows the variation of  $R_{OFF}$  over 10 different cells with SOG and WO<sub>3</sub> as insulator (fabrication protocol E). The data points of  $R_{OFF}$  in the graph are the mean values of the cells' resistance in the HRS. While the SOG cells show a  $R_{OFF}$  of  $5.2 \pm 3.0$  GΩ, it is only  $6.0 \pm 3.5$  MΩ for the cells using WO<sub>3</sub> as insulator. The lower  $R_{OFF}$  for the WO<sub>3</sub> cells leads to a narrower resistance window between HRS and LRS, since for both cell compositions  $R_{ON}$  is equally determined by the electrode resistance and the current compliance. As a consequence, the WO<sub>3</sub> cells show a lower potential for multi bit data storage due to the fact that a lower amount of distinguishable intermediate states fits between  $R_{OFF}$  and the lowest possible  $R_{ON}$ . The SOG cells with a  $R_{OFF}$

in the range of  $\text{G}\Omega$  can be switched with an  $I_{cc}$  as low as 10 nA resulting in a  $R_{ON}$  of almost 100 M $\Omega$ . By contrast, cells with WO<sub>3</sub> already feature leakage currents in the HRS of almost 1  $\mu\text{A}$  and therefore cannot be switched with an  $I_{cc}$  lower than 1  $\mu\text{A}$ , which results in a maximum  $R_{ON}$  of approximately 100 k $\Omega$ . This comparison can be seen in fig. 4.19(b), where the SOG data is identical to the one shown in fig. 4.4. The data in fig. 4.19(b) show a slope of  $-0.84 \frac{\Omega}{\text{A}}$  for SOG and  $-0.70 \frac{\Omega}{\text{A}}$  for WO<sub>3</sub>. The discrepancy is most likely caused by additional leakage currents, which lower the resistance and lead to a flatter slope. The variations of the leakage current probably results from a discrepancy in the cell area caused by variations of the printing process. The yield of the printed cells with WO<sub>3</sub> as insulating layer is 76 %, similar to the one for SOG. [96]

#### 4.3.2 Local Filament Formation with Conductive Atomic Force Microscopy

Similar to the CAFM measurements on Ag/SOG layers in subsection 4.1.3, the local filament formation is investigated with CAFM on Ag/WO<sub>3</sub> structures (fabrication protocol E on a Si/SiO<sub>2</sub> substrate without PEDOT:PSS top electrodes).

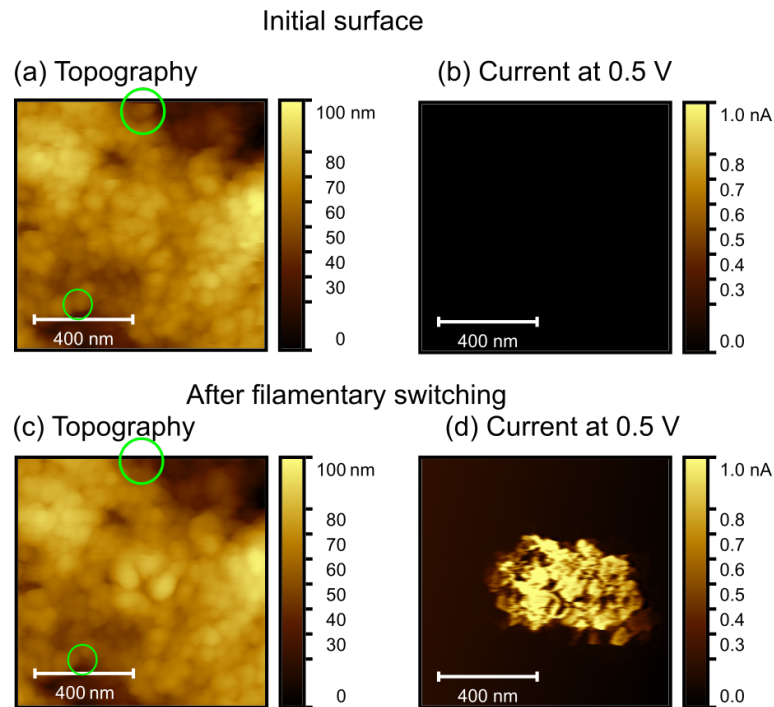


Figure 4.20: Local filament formation in printed Ag/WO<sub>3</sub> structures. (a) Topography of the initial surface with a root mean square of 16.7 nm showing the individual WO<sub>3</sub> nanoparticles and (b) current image at a tip voltage of 0.5 V and a current range of 1 nA showing the insulating WO<sub>3</sub>. (c) Topography after filament formation in the middle of the scan area with a voltage sweep from 0 V to -9.9 V and back to 0 V with a current range of 10  $\mu\text{A}$  and a compliance resistor of 10 k $\Omega$ . (d) Current image at 0.5 V and 1 nA current range demonstrating electrical conductivity of the created filament hillock. All four scans have an area of 1  $\mu\text{m} \times 1 \mu\text{m}$  and contain 257 x 257 pixels. The green circles indicate spots, where individual WO<sub>3</sub> nanoparticles moved during the scanning process. Graph adapted from [96].

Fig. 4.20(a) shows the individual crystalline  $\text{WO}_3$  nanoparticles covering the Ag bottom electrode prior to switching. The corresponding current image at a tip voltage of 0.5 V can be seen in 4.20(b). Here, a current range of 1 nA results in a better resolution. The tip is placed in the middle of the scan area and a voltage sweep from 0 V to -9.9 V and back to 0 V with a current range of 10  $\mu\text{A}$  and a compliance resistor of 10 k $\Omega$  is applied. The subsequent scan depicts the created Ag filament in the middle of the scan area in the topography scan (fig. 4.20(c)) and in the current map (4.20(d)). The area giving a current signal is not uniform and also larger than the changed topography in the middle of scan (c). This could be explained by the fact that the Ag filament fills up the voids between the  $\text{WO}_3$  nanoparticles and therefore a current signal occurs in the gaps between the nanoparticles, which have been filled with Ag atoms. The green circles in fig. 4.20(a) and (c) show individual nanoparticles, which most likely are moved by the AFM tip during scanning and change positions. This illustrates the loose structure of the  $\text{WO}_3$  layer as an agglomeration of unsintered nanoparticles. Similar as shown in section 4.1 a FIBSEM cut can reveal the cross section of the created Ag filament. However, the  $\text{WO}_3$  layer features a higher surface roughness compared to the SOG layer and the filament hillocks created by CAFM are not as prominent in the topography. Therefore, after switching with CAFM, it is not possible to locate individual filaments or even lines of filaments using SEM in order to use a FIB for the cross section view. To that end, the tip of the CAFM at a voltage of -9.9 V on the Ag/ $\text{WO}_3$  structure scans a filled square of approximately 15  $\mu\text{m}$  side length with a scanning speed of 0.1  $\mu\text{m s}^{-1}$  and a distance between the lines of about 800 nm. Thus, a whole area with Ag filaments driven through the  $\text{WO}_3$  nanoparticle layer is created. This area can be located with SEM and a FIB can create a cross section to enable a direct view of the created Ag filaments.

Fig. 4.21(a) and (b) show a secondary electron and back scattered electron scan of the Ag/ $\text{WO}_3$  layer stack covered by the Pt protection layer required for the FIB cut. Voids in the approximately 400 nm thick  $\text{WO}_3$  layer are visible. For this material composition the back scattered electron scan does not show high material contrast due to the fact that the arithmetic mean of the atomic numbers of  $\text{WO}_3$  ( $Z=74$  for W and  $Z=8$  for O) is closer to Ag ( $Z=47$ ) compared to SOG ( $Z=14$  for Si and  $Z=8$  for O). Fig. 4.21(c) and (d) depict a FIB cut in the 15  $\mu\text{m} \times 15 \mu\text{m}$  area of filamentary switching. Ag filaments appearing bright and going from top to bottom can be seen over the whole cross section of the  $\text{WO}_3$  layer. The increased amount of voids in the Ag bottom electrode is most likely caused by Ag atoms leaving the Ag layer to form the filaments. The curled shape of the filaments could be an effect of the nanoparticle structure of the  $\text{WO}_3$  layer, where the Ag filaments tend to grow around the individual  $\text{WO}_3$  nanoparticles.

By comparison of the dense and amorphous SOG layer with the loose agglomeration of crystalline  $\text{WO}_3$  nanoparticles as insulating layer, the  $\text{WO}_3$  suffers from a higher leakage current, although its layer thickness is about 8 times thicker compared to the SOG in the printed ECM cell structure. This can most likely be attributed to the higher amount of surface states between the individual nanoparticles [118]. Therefore, the Ag filaments also fill up the voids between the  $\text{WO}_3$  nanoparticles and form a curlier shape compared to the filament through the SOG.

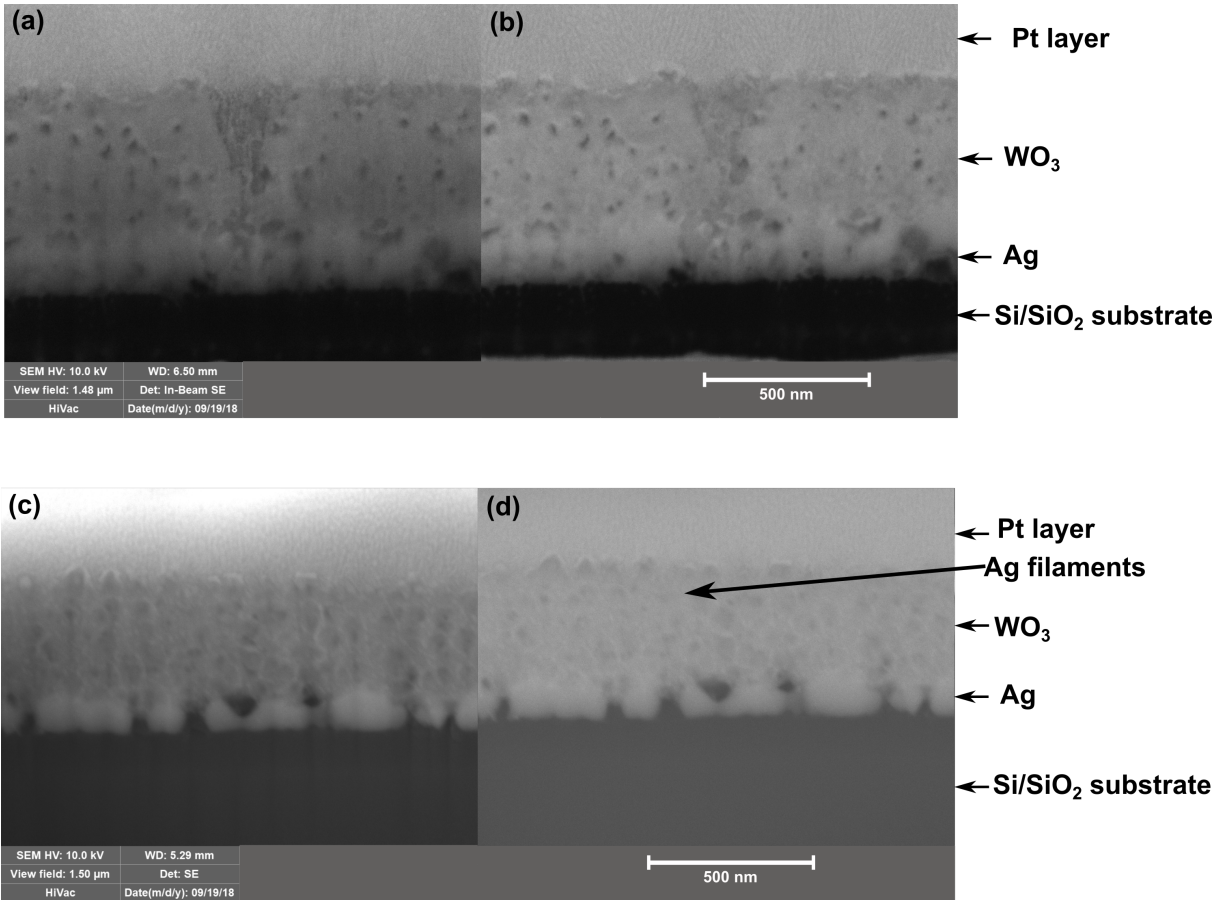


Figure 4.21: (a) Secondary electron and (b) back scattered electron image of the cross section of the Ag/WO<sub>3</sub> layer structure on a Si substrate with a 100 nm thick SiO<sub>2</sub> insulating layer. (c) Secondary electron and (d) back scattered electron image of Ag filaments switched through the WO<sub>3</sub> with CAFM. An area of filaments is switched with the CAFM tip at -9.9 V scanning the surface with 0.1  $\mu\text{m s}^{-1}$ . A Pt protection layer is deposited on the sample prior to cutting with the FIB beam.

#### 4.3.3 Retention Analysis

Similar to the ECM with SOG as solid electrolyte, cells with WO<sub>3</sub> as insulating material show a limited retention time due to spontaneous diffusion of the Ag filament. Consecutive read cycles after filament formation can give more information on the Ag diffusion process. A printed Ag/WO<sub>3</sub>/PEDOT:PSS cell is switched with a voltage pulse of 4 V and 0.1 s followed by consecutive read cycles at 0.2 V. Fig. 4.22 shows the increasing resistance due to the filament diffusion (fabrication protocol E). The fit uses formula 4.1 with the two fixed parameters  $A$ , the electrode resistance, and  $B$ , the initial resistance of the filament. Since the initial resistance directly after switching is 7305 Ω, and the electrode resistance  $A$  is measured as 5280 Ω, and therefore  $B = 2025 \Omega$ . This leads to  $C = \frac{D}{r_0^2} = 5.2 \cdot 10^{-5} \text{ s}^{-1}$ . Again,  $r_0$  remains the biggest uncertainty and can only be approximated by the filament cross section from the FIBSEM image fig. 4.21 as about 20 nm. The difference in switching parameters, i.e. local switching with CAFM tip

and  $10 \mu\text{A}$  current compliance for the FIBSEM image and pulsed switching without any current compliance for the retention measurement, may also result in a difference in filament diameters. Therefore, this analysis gives only an approximation and leads to the diffusion coefficient of Ag in  $\text{WO}_3$  nanoparticles of  $D = 2.1 \cdot 10^{-20} \frac{\text{m}^2}{\text{s}}$ . Although the diffusion coefficient was found to be lower compared to Ag in SOG, the maximum retention time of the Ag/ $\text{WO}_3$ /PEDOT:PSS cells is smaller with  $1.4 \cdot 10^4$  s. A possible explanation could be that even though the diffusion is slower in  $\text{WO}_3$ , the filament diameter is limited to the size of the voids in the  $\text{WO}_3$  nanoparticle structure.

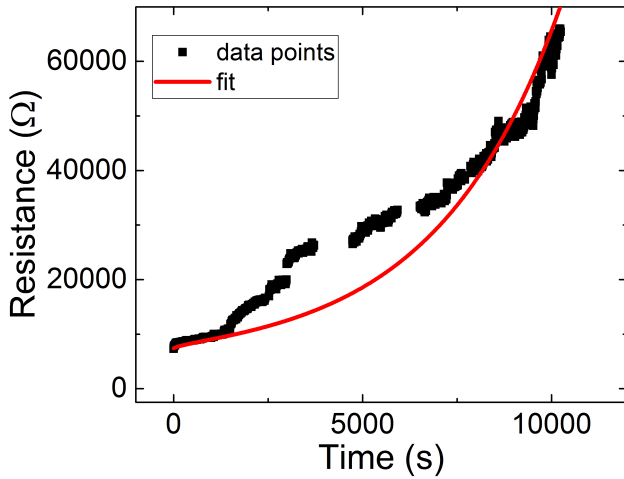


Figure 4.22: Change of the ON resistance of an Ag/ $\text{WO}_3$ /PEDOT:PSS cell over time shows the gradual diffusion of the silver filament. The cell is SET with a 0.1 s pulse of 4 V. The red line shows the fit using formula 4.1 with fixed parameters  $A = 5280 \Omega$ ,  $B = 2025 \Omega$ , and the fitted parameter  $C = 5.2 \cdot 10^{-5} \text{ s}^{-1}$ .

#### 4.4 Mechanical Characterization for Flexible Applications

This section covers the mechanical flexibility of the printed ECM cells on flexible substrates. All experiments are designed to reproduce possible requirements of specific applications for flexible memory devices. Covering all fields of possible applications, flexibility requirements can be divided into two categories. First, the memory device has to be functioning when it is under static deformation at a specific bending radius. This includes applications, where the device has to adapt to a bent surface, for example in smart packaging. Here, the memory cells have to switch reproducibly at low bending radii without the switching parameters depending on the applied strain. Second, other applications may include repetitive bending cycles, for example washing smart textiles in a washing machine or flexible foil packages being bent during transportation. This cyclic bending is monitored by a continuous tracking of the memory cells' switching characteristic after an increasing number of bending cycles. Thus, the fatigue failure of the cell can be determined.

The rotate-to-bend device is used for both static as well as dynamic bending tests, since it offers the possibility to apply both tensile and compressive strain. Furthermore, the automated apparatus is especially useful for the cyclic bending tests, where thousands of bending cycles have to be applied.

Both subsections for static and dynamic bending are organized in a similar structure. First, printed single lines of the electrode materials Ag and PEDOT:PSS undergo the test procedures in order to investigate the influence of the electrodes. Then, complete ECM cells are characterized under bending.

#### 4.4.1 Static Bending

For the static bending tests, the sample is gradually bent while undergoing electrical measurements in the bent state with a defined bending radius. These in-situ measurements are enabled by connection wires soldered to the sample. Therefore, an *Acheson G 3692* Ag paint is brushed on the contacts of the sample and 75  $\mu\text{m}$  thick insulated copper wires are soldered onto the Ag paint. The other end of the wire is then connected to a *Keithley 2400 Sourcemeter* for simple resistance measurements of electrode lines or sweep measurements on complete cells.

Before investigating complete cells, printed single lines of the two electrode materials Ag nanoparticles and PEDOT:PSS are measured. To that end, a 1 cm line of Ag nanoparticles and PEDOT:PSS is printed on *Teonex Q83* PEN foils with thicknesses of 25  $\mu\text{m}$ , 50  $\mu\text{m}$ , and 125  $\mu\text{m}$  (fabrication protocol F of bottom electrode). The different substrate thicknesses allow for a wider variation of the applied strain according to formula 2.6.

Fig. 4.23(a) shows the change in resistance over the bending angle for printed lines of Ag nanoparticles. The resistance decreases for compressive bending (negative angles) and increases for tensile strain (positive angles). The bending angle is varied in steps of 1.8° (one step of the stepper motor) up to  $\pm 108^\circ$  and the line resistance is measured for every step in the bent state. A distance between the clamps of  $L = 15$  mm results in a minimum bending radius of 3.7 mm according to formula 3.3. As the Ag lines act as strain gauge, the change in resistance is direct proportional to the applied strain  $\epsilon$  (see equation 2.6), which for a given bending radius is direct proportional to the substrate thickness  $d$  (see equation 2.7). Thus, the change in resistance is also direct proportional to the substrate thickness  $d$  for a given bending radius. This can be seen in the different slopes of the curves in fig. 4.23(a). Fig. 4.23(b) shows the change in resistance versus the strain, where a maximum strain of  $\pm 1.6\%$  can only be achieved with the 125  $\mu\text{m}$  thick foil. The inset shows the linear region of the curves for small strains. Here, the curves of all three substrates share the same slope  $k = 3.2$ , which represents the gauge factor. The gauge factor being larger than 2 indicates a piezoresistive effect of the Ag nanoparticles [71]. The deviation of the 125  $\mu\text{m}$  thick sample for tensile strain in the inset can be attributed to plastic deformation of the PEN substrate. For higher strains ( $\epsilon > 0.7\%$ ) the change in resistance increases nonlinearly. This behavior can be explained by crack onset strain, where the sample is no longer in the elastic regime and cracking already occurs [44],[52]

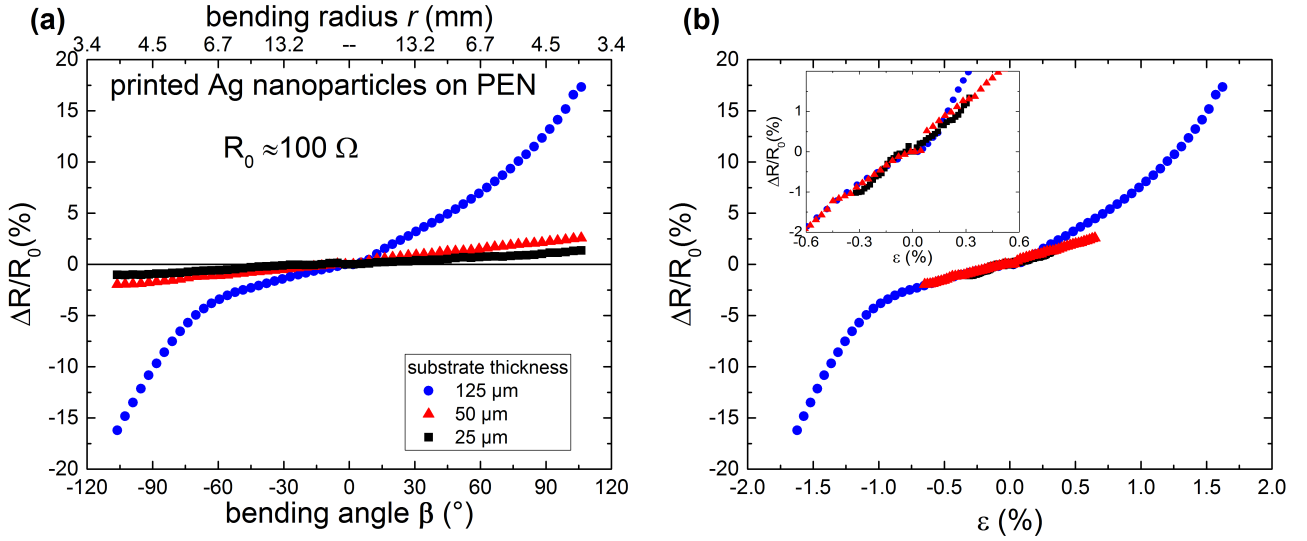


Figure 4.23: Static bending of printed Ag nanoparticle lines. The normalized change in resistance is plotted against (a) the bending angle and (b) the strain  $\epsilon$ . Negative angles represent compressive, negative strain (decreasing resistance), positive angles lead to positive, tensile strain (increasing resistance). The experimentally determined bending radius is depicted as a top x-axis in (a). The inset of (b) shows the linear behavior for small strains with the gauge factor  $k = 3.2$  as slope.[52]

The same static bending tests for a printed 1 cm long PEDOT:PSS line shown in fig. 4.24 give a more complex behavior.

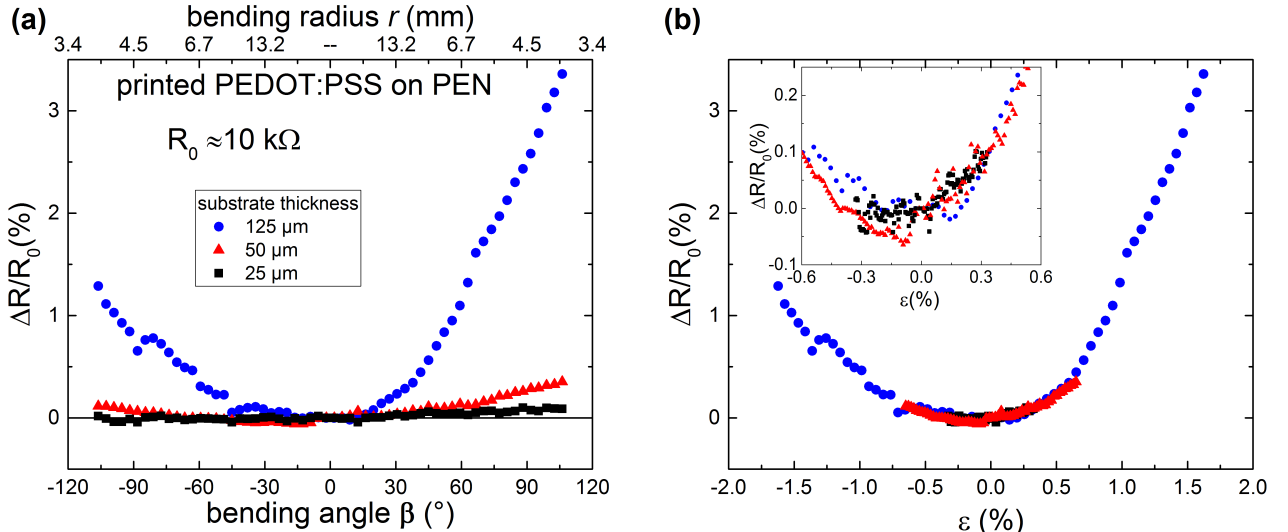


Figure 4.24: Static bending of printed PEDOT:PSS lines. The normalized change in resistance versus (a) bending angle and (b) strain shows an increase in resistance for both tensile as well as compressive bending. The inset of (b) shows the behavior for small strains.

Five layers are printed as a 1 cm long line with a drop spacing of  $5 \mu\text{m}$  and 1 jet at  $60^\circ\text{C}$ . The PEDOT:PSS is subjected to a nonlinear increase in resistance for both tensile and compressive strain. Studies have shown a nonlinear behavior of the PEDOT:PSS resistance for tensile deformation [81][133], but until now the effects of compressive strain have not been investigated. The fact that compressive strain results in an increase of resistance indicates that not only a macroscopic change of the line's geometry during bending influences the resistance. Most probably, the complex interplay between the two electrostatically bound ionomers PEDOT and PSS changes during bending and leads to the increase of the resistance, regardless of the direction of the bending. A movement of the individual PEDOT:PSS grains during bending leading to decohesion could also affect the resistance [34]. The matching curves in the inset of fig. 4.24(b) shows that this behavior solely depends on the strain and can be reproduced for different foil thicknesses. The small variations are caused by measurement uncertainty.

The static bending tests on the single lines of Ag and PEDOT:PSS give an estimation of the electrodes' influence on the static bending of complete cells. Therefore, the width and height of the lines investigated in fig. 4.23 and 4.24 are similar to the parameters used for the printed memory cells. The length of the electrodes varies for the cell layout, though. For the 1 cm long printed Ag lines with a typical resistance of  $100 \Omega$ , a strain of  $\pm 1.6\%$  leads to a change in resistance of  $100 \Omega \pm 17\%$  or  $(100 \pm 17) \Omega$ . The 1 cm long PEDOT:PSS lines typically show a higher resistance of  $10 \text{ k}\Omega$ . The maximum applied strain of  $\pm 1.6\%$  causes a maximum increase in resistance for tensile deformation of  $10 \text{ k}\Omega \pm 3.4\%$  or  $(10 \pm 0.34) \text{ k}\Omega$ . Hence, the PEDOT:PSS has a lower relative change in resistance, but due to its higher absolute resistance also the absolute change in resistance is higher compared to the Ag.

In a crossbar array bending can occur in any direction and therefore partial contributions of both the bent word- and bitlines of the electrodes have to be taken into account. However, the typical cell layout only consists of one wordline of the Ag bottom electrode and several shorter bitlines of the PEDOT:PSS top electrode (see subsection 3.1.3). Thus, for the tests of the complete cells, the cells are only bent along the longer Ag bottom electrode, while exerting only minor strain on the perpendicular PEDOT:PSS top electrodes. For crossbar arrays, bending directions perpendicular to both electrode lines and even angular bending might be of interest.

Possible failure mechanisms for ECM cells undergoing static bending could either be a high variation of  $R_{\text{ON}}$  due to deformation of the electrode lines or even an irreversible increase of  $R_{\text{ON}}$  caused by crack formation in the electrodes. Strain induced cracks in the SOG insulating layer could also lead to a higher amount of leakage current and therefore reduce  $R_{\text{OFF}}$ . Both failure mechanisms result in a tightening of the resistance window between  $R_{\text{ON}}$  and  $R_{\text{OFF}}$  and therefore cause degradation of the switching behavior.

Fig. 4.25 shows  $R_{\text{OFF}}$  and  $R_{\text{ON}}$  for an Ag nanoparticle/SOG/PEDOT:PSS cell on a  $125 \mu\text{m}$  PEN foil (fabrication protocol F). The bending radius is varied from 8 mm to 2 mm, where a negative bending radius is attributed to compressive deformation. The unbent state is shown as two data points in the center with infinite bending radius. For each bending radius a quasi-static voltage sweep is applied from 0 V to 1 V, down to -0.2 V, and back to 0 V with a step size of 0.01 V and a current compliance of  $2 \mu\text{A}$ . Each data point for  $R_{\text{OFF}}$  in fig. 4.25 is the mean value of the

HRS state in the negative voltage regime after RESET, while  $R_{ON}$  is calculated as the mean of all quasi-static measurements in each sweep, where the current compliance is reached. Fig. 4.25 shows no dependence of  $R_{OFF}$  and  $R_{ON}$  on the bending radius exceeding the statistical variation of the resistive switching.  $R_{OFF}$  has an arithmetic average of  $(2.7 \pm 1.9) \cdot 10^7 \Omega$  over all bending radii, while  $R_{ON}$  attributes to  $(4.8 \pm 1.8) \cdot 10^4 \Omega$ . The variation is attributed to the stochastic nature of the switching with a certain amount of randomness caused by a system which contains only a limited number of atoms [19]. The influence of bending on the resistance of the electrodes is negligible compared to these stochastic variations caused by the switching process.

The memory cell on the  $125 \mu\text{m}$  thick substrate can be bent to a minimum bending radius of 2 mm for both compressive and tensile deformation without showing a degradation of the switching characteristics. 2 mm is the minimum bending radius which can be achieved with the rotate-to-bend apparatus with a distance between the clamps of  $L = 8 \text{ mm}$  and a bending angle of  $\beta = 108^\circ$ . A lower bending radius could be achieved by decreasing  $L$  or increasing  $\beta$ . A smaller  $L$  is not possible, since the memory cell with the contact wires has to fit between the clamps and the clamps come in contact with each other for larger  $\beta$ . However, a 2 mm bending radius on a  $125 \mu\text{m}$  thick foil substrate exerts a strain of 3.1 %. A thinner foil with  $25 \mu\text{m}$  thickness can be bent to a radius of 0.4 mm until it reaches a strain of 3.1 %. Thus, it is very likely that the printed memory cells can be bent well below 1 mm on thin substrates, although it is not yet possible to demonstrate this by our in situ measurements.

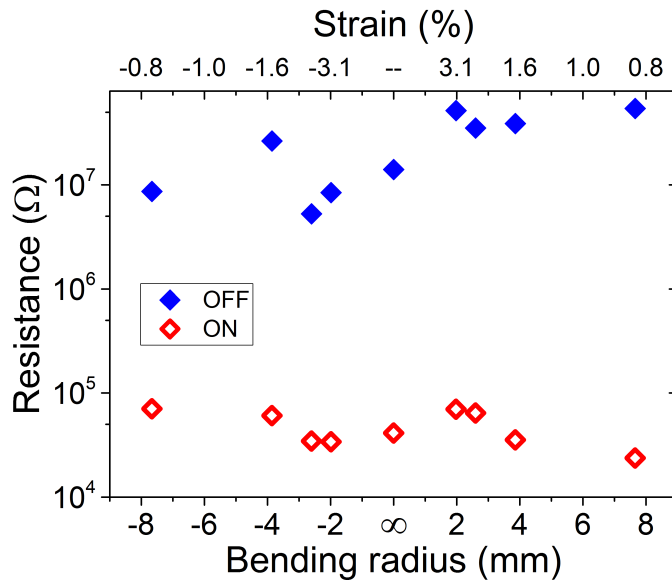


Figure 4.25: Static bending of an Ag nanoparticle/SOG/PEDOT:PSS cell printed on a  $125 \mu\text{m}$  PEN foil in both direction using the rotate-to-bend setup. Negative bending radii stand for compressive strain, while an infinite bending radius correlates to unbent conditions. The sample withstands a bending radius of  $\pm 2 \text{ mm}$  exerting a strain of  $\pm 3.1 \%$  for both tensile and compressive distortion.

#### 4.4.2 Cyclic Bending

Static bending induces reversible changes in the printed structures, where the change in resistance for printed structures in a bent state returns to the initial state after relaxation. A minor offset can occur due to irreversible changes in the material caused by plastic deformations upon cycling. Cyclic bending on the other hand directly tracks those irreversible changes caused by repetitive bending cycles. To that end, the tracked device parameter, for example its resistance, is always measured in the unbent state between consecutive bending cycles of a specific bending radius.

Similar to the static bending tests, cyclic fatigue of printed lines of the electrode materials alone is evaluated before testing complete memory cells. Therefore, 1 cm long lines of the electrode materials are printed on PEN foils with varying thickness and contacted with soldered copper wires at the two ends of the lines. Again, the ability of the rotate-to-flex apparatus to bend in both direction offers a great advantage. This enables the direct implementation of possible bending scenarios for device applications such as smart textiles being randomly bent in various directions during a washing process. Although the IPC-6013 industrial standard for flexible electronics recommends full bending cycles (tensile as well as compressive bending), it still uses a roller-flex apparatus, where printed structures can be damaged during compressive bending [57].

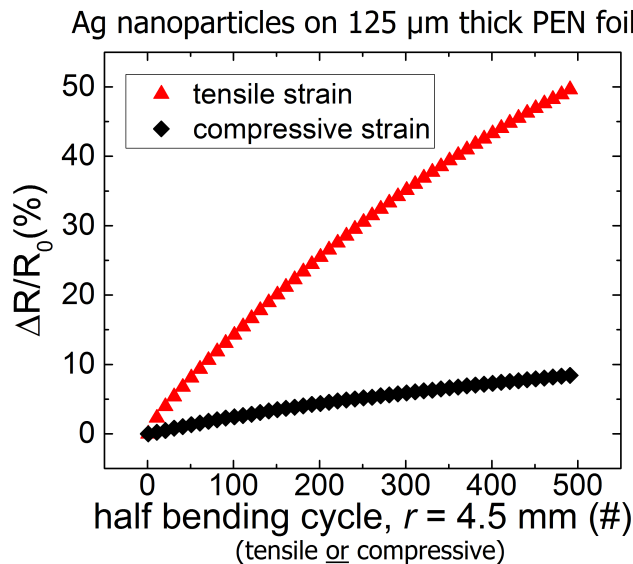


Figure 4.26: Normalized change in resistance for either tensile or compressive cyclic deformation of a printed line of Ag nanoparticles on a 125  $\mu\text{m}$  PEN foil. The resistance is measured in the unbent, neutral position.[52]

Fig. 4.26 shows the individual effects of either tensile or compressive cycling on printed lines of Ag nanoparticles (fabrication protocol F of electrodes). The maximum bending angle for the 500 half bending cycles is  $\pm 90^\circ$  with  $L = 15$  mm, resulting in a bending radius of 4.5 mm and a strain of  $\pm 1.4\%$ . Here, the sample undergoes only a half bending cycle in one direction and its resistance is measured after every three half bending cycles in the unbent position. The gradual

increase in resistance most likely originates from microcracks in the Ag line, which develop further after each bending deformation [95]. Clearly, the tensile bending leads to a stronger increase in the resistance after each bending cycle by a factor of 6 compared to compressive cycling. This is caused by the fact that microcracks are preferentially generated during tensile stress. This behavior plays an important role for flexible devices, whose applications involve bending in a preferential direction. Their whole design could be adjusted to match the preferential bending direction to be compressive, thus enhancing their fatigue lifetime.[52] Fig. 4.27 shows the impact of cyclic bending fatigue on the three electrode materials Ag nanoparticles (a), Ag nanowires (b), and PEDOT:PSS (c) for full bending cycles (fabrication protocol F of electrodes). The minimum bending radius for the 900 full bending cycles with  $L = 15$  mm and  $\beta = \pm 90^\circ$  is 4.5 mm. This causes a maximum strain of  $\pm 1.4\%$  for the 125  $\mu\text{m}$  thick substrate.

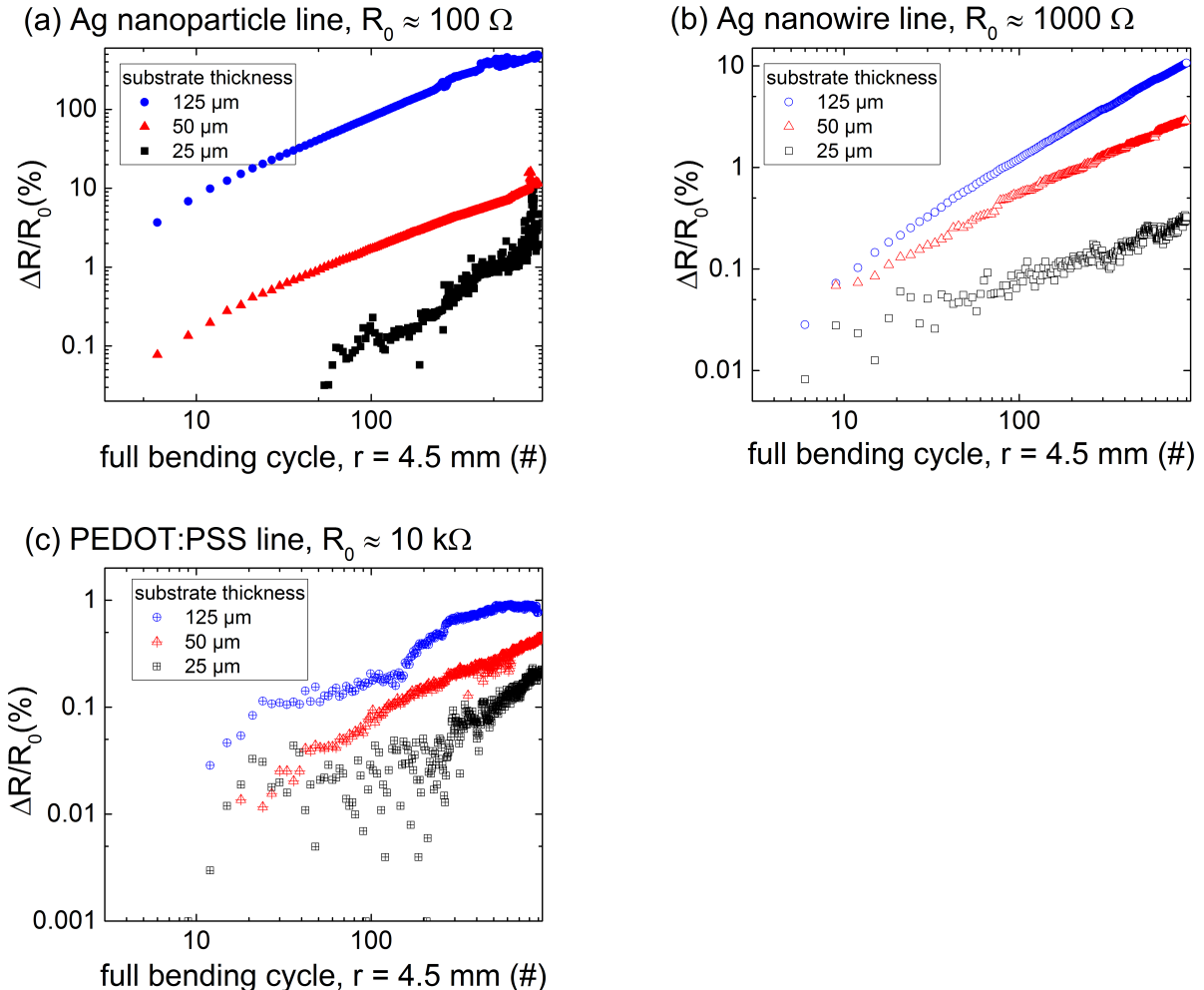


Figure 4.27: Cycling fatigue behavior of printed lines (double-log plots) composed of (a) Ag nanoparticles, (b) Ag nanowires, and (c) PEDOT:PSS on a PEN substrate with a thickness of 25, 50 and 125  $\mu\text{m}$ . The minimum bending radius at  $\beta = \pm 90^\circ$  is 4.5 mm.[52]

Two main findings can be extracted from fig. 4.27: Firstly, for each ink, the substrate thickness greatly influences the increase in resistance after cyclic bending. The direct proportionality between the strain acting on the electrode line and the substrate thickness clearly impacts the formation of microcracks or other functional changes during bending [47]. Secondly, the relative increase in resistance highly depends on the electrode material. The maximum change in resistance for the 125  $\mu\text{m}$  thick substrate and 900 full bending cycles is highest for the Ag nanoparticle line (a) with 481 %, followed by the Ag nanowire line (b) with 11 %, and the PEDOT:PSS line (c) with 1 %. This behavior can be explained by looking at the morphology of the different structures. During sintering, the individual Ag nanoparticles fuse and form a porous, but continuous film [45][17]. This almost bulk-like structure is more prone to develop microcracks (see fig. 4.28) than the mesh-like printed nanowires and the intrinsically flexible PEDOT:PSS. The nanowire network is more resilient against bending and the formation of cracks due to its mesh-like structure. If the sintered connection between two nanowires breaks up, they may slide reversibly on top of each other when strain is applied and still sustain an electrical connection [139]. The strain-induced fatigue mechanism for PEDOT:PSS has not been fully understood. The increase in resistance shown in fig. 4.27(c) could be caused by gradual decohesion of the individual PEDOT:PSS grains during bending [34]. The increase in resistance is almost linear, i.e. the double-logarithmic curves show a slope of 1 with slight fluctuations, for all nine curves of fig. 4.27. This indicates that the formation of microcracks, breaking of nanowire connections, or decohesion of conjugated polymers happens gradually without major degradation events.[52] Fig. 4.28 shows printed Ag lines after 1000 bending cycles. While no visible changes can be detected on the lines, SEM images reveal microscopic cracks in the nanoparticle lines. Microcracks perpendicular to the bending direction can be seen on the nanoparticle lines, whereas the Ag nanowire network does not show any morphological change. It is worth noticing that due to charging effects of the PEN substrate during SEM measurements, a 2 nm thick layer of Pt has to be sputtered on the samples prior to SEM imaging. Since the Pt layer could influence the bending behavior, images before and after bending cannot be taken from the same sample but representative images from one sample before and another sample after bending show the morphological change.[52]

As fig. 4.27 displays the relative change in resistance, the absolute resistance value of the electrodes determines their concrete contribution on an actual memory device. A 1 cm long electrode line with width and height comparable to those of a printed cell shows a typical resistance in the range of 100  $\Omega$  for an Ag nanoparticle line, 1000  $\Omega$  for an Ag nanowire line, and 10 k $\Omega$  for a PEDOT:PSS line. The thickest substrate, the 125  $\mu\text{m}$  thick PEN foil, leads to the maximum change in resistance for 900 bending cycles. The resistance of the Ag nanoparticle line is enlarged by 481 % or 760  $\Omega$ , the resistance of the Ag nanowire line increases by 11 % or 143  $\Omega$ , while the PEDOT:PSS features a resistance growth of 1 % or 92  $\Omega$ . The Ag nanoparticle line with the lowest initial resistance is subjected to the highest resistance increase due to irreversible formation of microcracks. Thus, the measurements of the individual electrodes suggest that the combination of Ag nanowires and PEDOT:PSS is favorable for flexible memory devices.

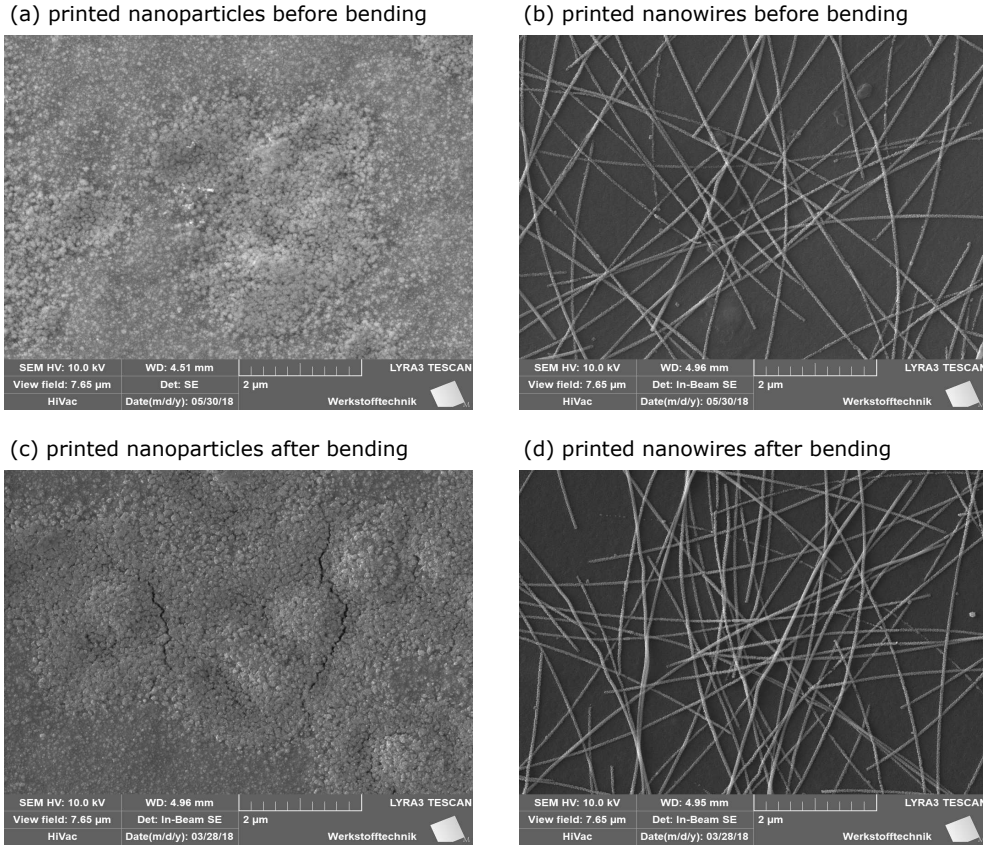


Figure 4.28: SEM images of printed (a) Ag nanoparticle and (b) Ag nanowire line prior to bending. (c) Microcracks in the Ag nanoparticle line after 1000 full bending cycles with a radius of 4.5 mm. (d) Printed Ag nanowires subjected to the same cycle procedure showing no degradation. All lines are printed on 125  $\mu\text{m}$  thick PEN foil.[52]

For cyclic bending tests with complete ECM cells, Ag/SOG/PEDOT:PSS cells with both Ag nanoparticle and nanowire bottom electrode are fabricated in order to investigate their influence on the bending fatigue (fabrication protocol F). Furthermore, PEN substrates of different thickness provide the influence of the substrate thickness. Unlike to all previous bending measurements, in situ measurements with soldered contact wires cannot be used, but the cells are measured outside the rotate-to-bend setup in a two-point probe station. This is due to the fact that the soldered connections cannot withstand such a high amount of bending cycles. Similar to the static bending of memory cells, bending takes place only along the Ag bottom electrodes in the cyclic bending experiments.

In order to simulate high operational demands, bending cycles are performed with a minimum bending radius of 3 mm for both compressive and tensile deformation. Therefore,  $L$  is set to 10 mm and  $\beta = \pm 90^\circ$ . PEN foil substrates with thicknesses of 25  $\mu\text{m}$ , 50  $\mu\text{m}$ , and 125  $\mu\text{m}$  are used, which exerts a maximum strain for  $r = 3$  mm of 0.4 %, 0.8 %, and 2.1 %, respectively.

Fig. 4.29 shows the results of the cyclic bending tests on complete memory cells.  $R_{\text{OFF}}$  and  $R_{\text{ON}}$  are obtained from quasi-static voltage sweeps from 0 V to 4 V, down to -0.3 V, and back to 0 V with a step size of 0.01 V and a current compliance of 2  $\mu\text{A}$ .

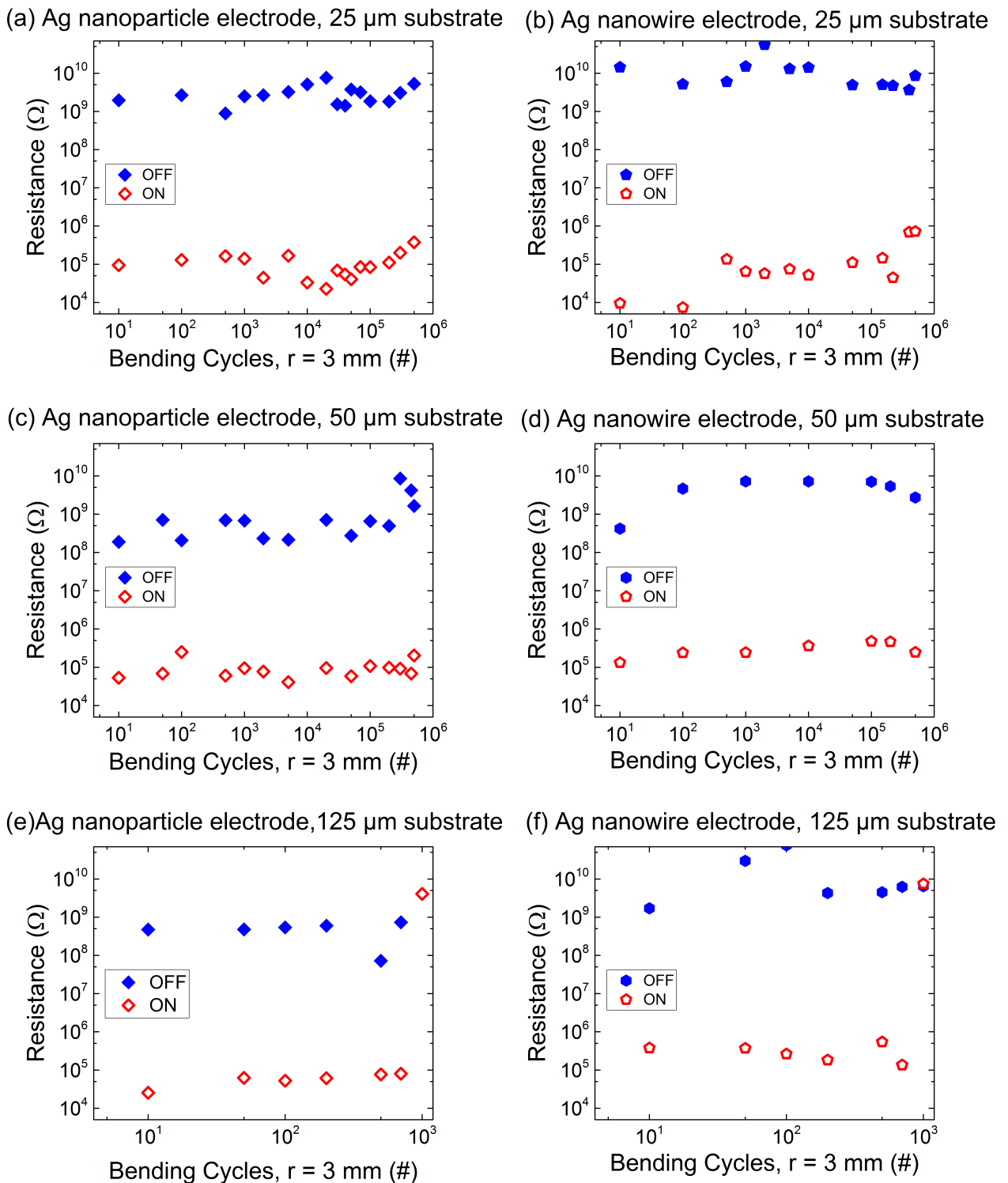


Figure 4.29: Cyclic bending of Ag/SOG/PEDOT:PSS cells with Ag nanoparticle (a, c, e) and nanowire (b, d, f) bottom electrodes for different substrate thickness and a bending radius of 3 mm (double-log plots). Both cell structures achieve more than 500,000 bending cycles for substrate thicknesses of 25  $\mu\text{m}$  and 50  $\mu\text{m}$ , whereas both structures fail after 700 bending cycles for 125  $\mu\text{m}$  substrates.

The upper four subfigures (a-d) of fig. 4.29 display similar results: Both cell structures with Ag nanoparticle and Ag nanowire bottom electrode achieve more than 500,000 full bending cycles without failure for a substrate thickness of 25  $\mu\text{m}$  and 50  $\mu\text{m}$ . The experiment stopped after 500,000 cycles, since a fatigue endurance of this value proves sufficient for most applications. Possible failure modes could again either be a fatigue degradation of the electrodes (increasing  $R_{\text{ON}}$ ) or crack formation in the SOG (decreasing  $R_{\text{OFF}}$ ). Both  $R_{\text{ON}}$  and  $R_{\text{OFF}}$  show no change with increasing number of bending cycles that stands out from the statistical variations. The resistance of the Ag bottom electrode is tracked during the bending experiment by measuring the line resistance of the 6 mm long Ag lines. For the 50  $\mu\text{m}$  thick substrate (subfigures (c, d)), the Ag nanoparticle electrode resistance increases from 133  $\Omega$  by a factor of 11 to 1438  $\Omega$ . The Ag nanowire electrode resistance rises from 520  $\Omega$  by a factor of 5 to 2620  $\Omega$ . The lower relative increase of the Ag nanowire line fits to the results of the electrode bending tests (see fig. 4.27). Although both bottom electrodes show a distinct increase of resistance, it is not noticeable compared to the statistical fluctuations.

Fig. 4.29(e) and (f) show a different result for the 125  $\mu\text{m}$  thick foil: Both cells with Ag nanoparticle and nanowire electrode are still functioning after 700 bending cycles, but fail at the next quasi-static electrical characterization after 1000 cycles. Both cells display a resistance above 1 G $\Omega$  without switching to the LRS due to an open circuit of the bottom electrode. Although the Ag nanowires are in principle more resilient against bending fatigue, both cell structures fail after the same amount of bending cycles. This is due to the fact that for repetitive bending with such a high strain of 2.1 %, the PEN foil starts to develop cracks. These cracks protrude into the printed structures on the foil and lead to open circuits for the Ag nanoparticles as well as the nanowires. Fig. 4.30 depicts the memory cell from fig. 4.29(e) after 1000 bending cycles with cracks leading to a failure of the Ag nanoparticle bottom electrode. It is worth noticing that the cracks originate in the PEN foil and cause cracks in the Ag line as well.

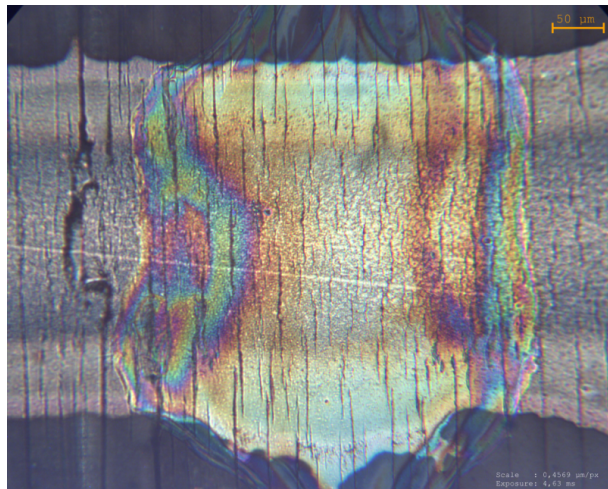


Figure 4.30: Ag nanoparticle/SOG/PEDOT:PSS cell on 125  $\mu\text{m}$  thick PEN foil after 1000 bending cycles with  $r = 3$  mm. One vertical, semi-transparent PEDOT:PSS top electrode crosses the Ag bottom electrode. The cracks in the PEN foil lead to cracks and failure of the Ag line.

#### 4.4.3 Summary and Discussion

As a conclusion of the static bending tests, the cells are fully functional at a minimum bending radius of 2 mm. This radius is the limit of the rotate-to-bend setup, indicating that lower bending radii are feasible for the memory cells.  $r = 2$  mm combined with a 125  $\mu\text{m}$  thick foil substrate exerts a strain of 3.1 %. If strain is the limiting factor, thinner substrates could enable even lower bending radii.

Cyclic bending tests give information on the bending fatigue of the materials as well as the complete cells. The Ag bottom electrode is found to be the critical component concerning fatigue degradation. Here, Ag nanowires show a higher resilience against bending compared to sintered Ag nanoparticles. Therefore, the bending fatigue behavior of printed cells with nanowires and nanoparticles as bottom electrodes are compared. Although tests on the electrodes alone suggest a better performance of the nanowires, measurements on full cells provide similar results. For thin substrates (25  $\mu\text{m}$  and 50  $\mu\text{m}$ ) the cells can undergo more than 500,000 full bending cycles with  $r = 3$  mm without any degradation in switching behavior. A thicker substrate of 125  $\mu\text{m}$  leads to a failure of both cell geometries after 700 bending cycles due to broken bottom electrodes.

While the bending tests still belong to a functional characterization of the memory cells, the next section covers a field for possible applications, which is especially suited for ReRAM: neuromorphic computing.

### 4.5 Synaptic Plasticity in Electrochemical Metallization Memory for Neuromorphic Computing

The growing field of neuromorphic computing depends on artificial synapses, i.e. synaptic plasticity of memory cells. Until now, standard ANNs rely on binary memory architecture, which is extremely inefficient in this framework. Therefore, the ECM cells are investigated concerning their potential to serve as artificial synapses.

The first subsection addresses the continuous diffusion process of the Ag filament as a possibility to implement a gradual forgetting process. The second subsection explores STDP as quantitative analysis of synaptic plasticity and examines how important factors influence the STDP function.

#### 4.5.1 Implementation of Long- and Short-Term Memory

The gradual diffusion of the Ag filament entails disadvantages when it comes to applications as non-volatile memory, since the data storage over a long time period may not be secured. However, the diffusion of the filament, i.e. the continuous transition from LRS to HRS, directly represents the forgetting process of the human brain, an aspect which is difficult to emulate with standard memory technology. This enables a further application: the implementation of long- and short-term memory.

The detailed mechanism how memory is created and processed in the human brain is still not fully understood. Nevertheless, the basic structural features of the memory system proposed

in 1968 are still valid [7]. According to this model, external input is first stored in a sensory register and a short-time store. From there, the information can be transferred to a long-term store through repeated rehearsal. While information in the sensory register and the short-time store eventually disappears, the long-term store is relatively permanent. Repeated rehearsal, i.e. external stimuli, are crucial for the transition from short- to long-term storage. The self-diffusing memory cells can model this phenomenon. To that end, the change in resistance of the cells represents the stored information, where low resistance stands for memorized information. External stimulus, which would be visual or auditory for the human brain, is represented by voltage pulses in the model.

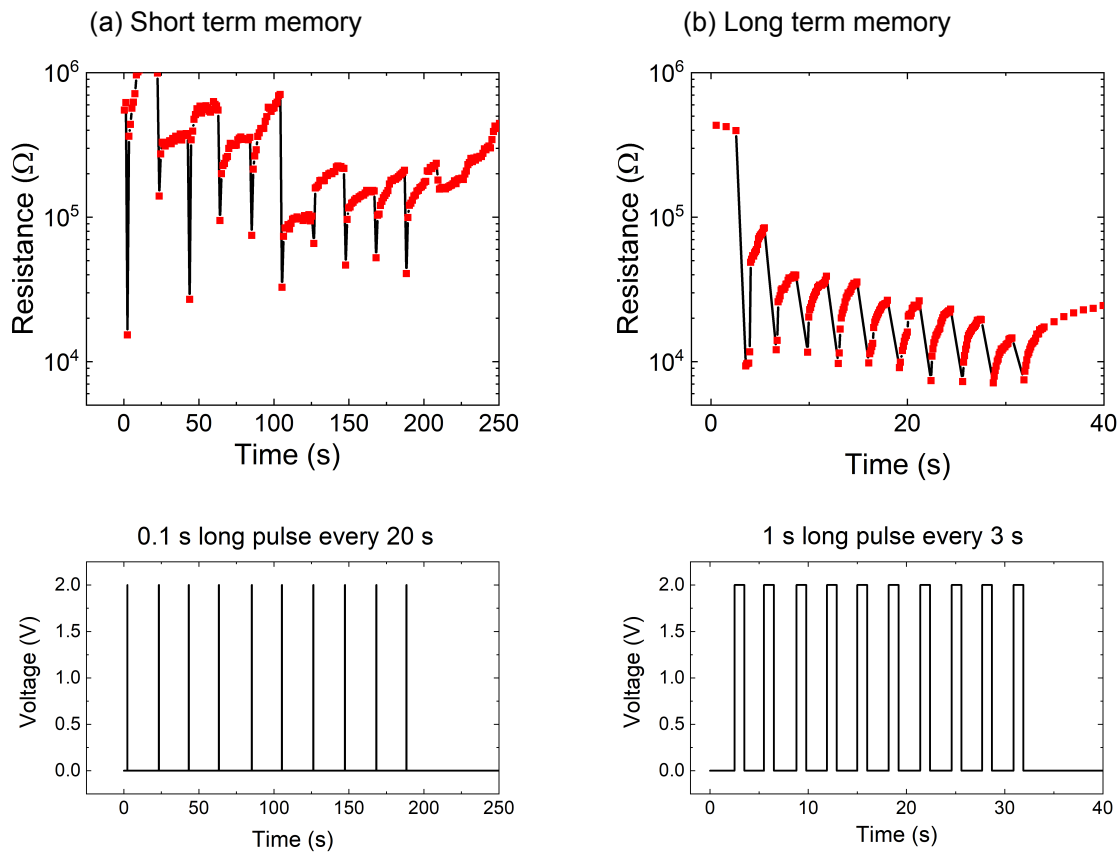


Figure 4.31: Repetitive voltage pulses of 2 V gradually switch a printed Ag/WO<sub>3</sub>/PEDOT:PSS memory cell. (a) Short voltage pulses of 0.1 s every 20 s only lead to short period of LRS until the filament diffuses again. (b) Pulses of 1 s every 3 s lead to a more stable Ag filament. The gradual increase in resistance between the pulses gets minimized and results in a stable LRS after the 10 pulses. The black connection line between the red data points in the resistance versus time plots acts as a guide to the eye.

Low voltage pulses of 2 V are applied on printed Ag/WO<sub>3</sub>/PEDOT:PSS memory cell (fabrication protocol E) to create an unstable LRS prone to fast diffusion of the Ag filament. When

the repetition rate of these external stimuli is too low, it never suffices to initiate the transition from short- to long-term memory. Fig. 4.31(a) shows this behavior for 0.1 s long voltage pulses with a delay time of 20 s between the individual pulses. The resistance is monitored by consecutive read pulses of 0.1 V, low enough not to trigger a SET operation of the cells. After each pulse, the resistance substantially decreases, but rises to approximately the initial level before the subsequent pulse. Hence, the resistance after 10 pulses remains the same value as at the beginning: the information always stayed in short-time memory and disappears again due to too long intervals between the rehearsal stimuli. The transition to long-term memory can be seen in fig. 4.31(b), where the pulses are longer with 1 s and at a higher repetition rate with only 3 s time between the pulses. This means that stronger stimuli (longer pulses) act on the cell at a higher rate of rehearsal. Similar to the behavior shown in fig. 4.31(a), the resistance drops after each voltage pulse and increases after the pulse caused by filament diffusion. However, due to the faster pulse rate, the resistance never reaches its initial value of the HRS and therefore further decreases with each voltage pulse as the filament gets gradually strengthened. After the completion of the 10 pulses the resistance remains relatively stable at approximately 40 k $\Omega$ , where diffusion takes a longer time period to consume the thicker filament. Thus, the stronger stimulus connected with a faster repetition rate enables the transition from a volatile short-term to a relatively stable long-term memory state.[102]

#### 4.5.2 Spike-Timing-Dependent Plasticity

The implementation of long and short term memory can be interesting for the realization of ANNs with a brain-inspired, gradual forgetting process. STDP is the basic working principle behind synaptic learning in the computationally more powerful subgroup of SNNs. Therefore, this subsection investigates in detail the influence of shape and amplitude of the action potential as well as the initial resistance  $R_{\text{init}}$  on the STDP function  $\frac{\Delta R}{R_0}(\Delta t)$ . The goal is to understand how the learning behavior depends on these parameters, which can either be controlled directly (action potential) or indirectly ( $R_{\text{init}}$ ). This understanding enables tailoring of the learning behavior of a single synapse or a whole SNN to fit the needs of a specific application. Thus, for example how strong a synapse has to react to one incoming stimulus may be different for various applications. The strength of the synaptic learning process thrives in a complete neural network. However, since the STDP experiments investigate on the basic working principle of the individual synapses' plasticity, only single ECM cells are used. The results of the single cells can be directly applied on integrated neural networks.

The mechanism of STDP is explained in subsection 2.3.4 : the STDP function  $\frac{\Delta R}{R_0}(\Delta t)$  depends on the time difference  $\Delta t$  between pre- and post-synaptic voltage spike. In practice, it is calculated by:

$$\frac{\Delta R}{R_0}(\Delta t) = \frac{R_{\text{after}}(\Delta t) - R_{\text{before}}(\Delta t)}{\min(R_{\text{before}}(\Delta t), R_{\text{after}}(\Delta t))} \quad (4.2)$$

, where  $R_{\text{before}}$  and  $R_{\text{after}}$  are the cell resistances read out before and after one overlap of pre- and post-synaptic voltage spike is applied to the cell. As a scaling factor in the denominator

$R_{before}$  and  $R_{after}$  are compared and the smaller value ( $\min(R_{before}(\Delta t), R_{after}(\Delta t))$ ) is used. In literature, often  $R_{before}$  is used as scaling factor [109], although it skews the STDP function and causes an underrepresentation of the exponential branch for positive  $\Delta t$ . A more detailed analysis of the influence of the normalization parameter can be found in appendix C. For the defined polarization, a positive  $\Delta t$  leads to a gradual SET and therefore a negative  $\frac{\Delta R}{R_0}$ . A gradual RESET for negative  $\Delta t$  then leads to a positive  $\frac{\Delta R}{R_0}$ .

The measurement starts at  $\Delta t = 0$ , then single STDP measurements (read, overlapping spikes for a specific  $\Delta t$ , read) are performed for one positive time step, one negative time step, then two positive time steps, two negative time steps and so on. Thus, the cell is always alternating between a gradual SET for positive  $\Delta t$  and gradual RESET for negative  $\Delta t$  and therefore its resistance is not subjected to a significant overall change throughout the measurement of one STDP function.

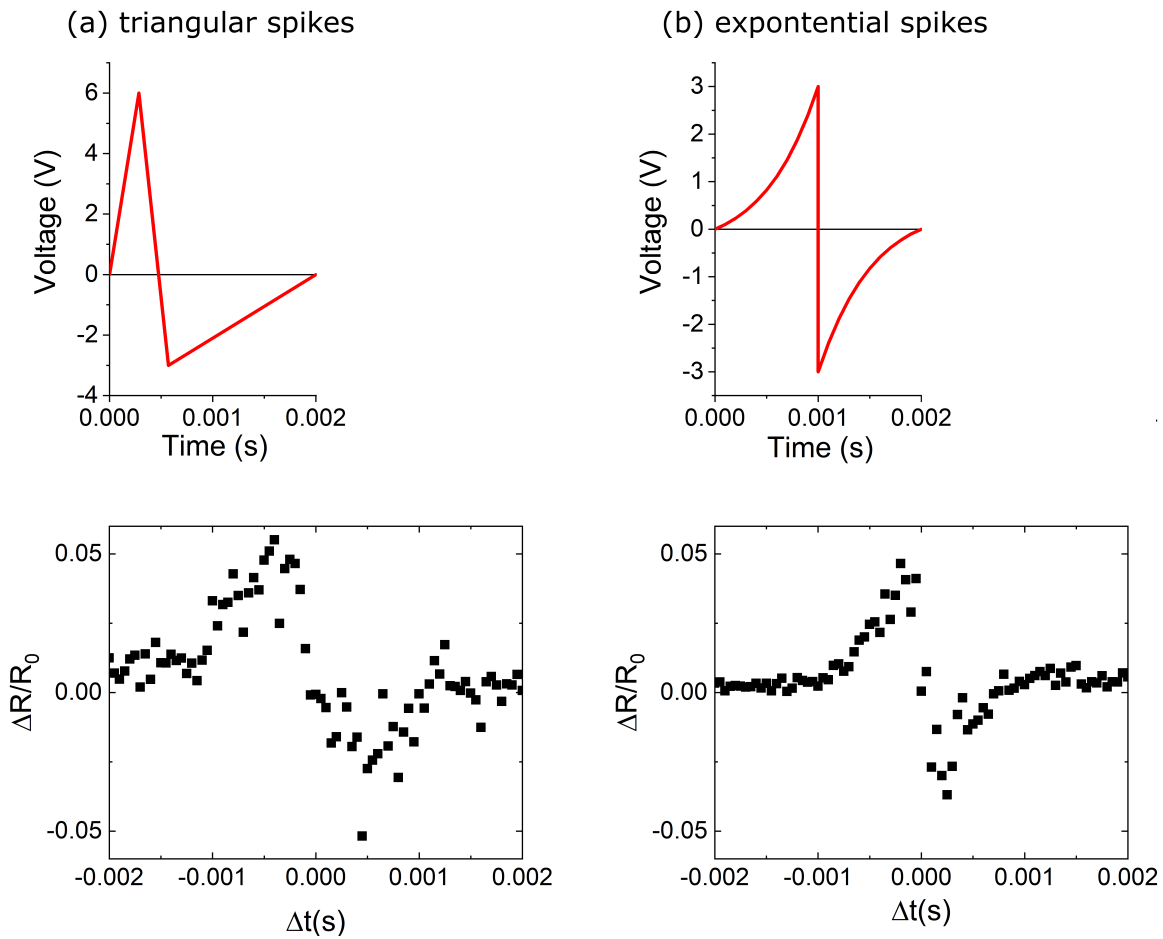


Figure 4.32: (a) Triangular and (b) exponential voltage spike: action potential as red curve and corresponding STDP function  $\frac{\Delta R}{R_0}(\Delta t)$  over  $\Delta t$  as black squares.

Fig. 4.32 compares the effect of triangular and exponential action potentials on the STDP function (see fig. 2.6 for more detailed explanation). The 2 ms long triangular spike has a 333  $\mu$ s long positive pulse with a maximum amplitude of 6 V and a 1667  $\mu$ s long negative tail with a

maximum amplitude of -3 V (see fig. 4.32(a)). The exponential pulse has a maximum voltage amplitude of  $\pm 3$  V and an exponential coefficient of  $\pm 0.38$  ms, i.e. the two exponential functions making up the exponential spike in fig. 4.32(b) follow the formula  $V(t) = \pm 3 \text{ V} \cdot e^{\mp \frac{t}{0.38 \text{ ms}}}$  with the time-dependent voltage  $V(t)$  and time  $t$  (see fig. 4.32(b)). In principle, it is difficult to define the length of an exponentially decaying pulse. With the given parameters, the exponential spike has a total length of approximately 2 ms and shows negligible voltages for time values outside the 2 ms intervall. The time step for  $\Delta t$  is set to  $50 \mu\text{s}$  for both triangular and exponential spikes and covers data points for the overall range of  $\Delta t$  of 4 ms, i.e. twice the length of the spikes. Both STDP measurements of fig. 4.32(a) and (b) are performed on the same Ag/SOG/PEDOT:PSS memory cell with an initial resistance  $R_0$  set to approximately  $4 \text{ k}\Omega$  (fabrication protocol B). Both triangular and exponential action potential cause a maximum change in resistance  $\frac{\Delta R}{R_0}$  of circa 5 %, but show a different shape of the STDP function.  $R_{\text{before}}$  and  $R_{\text{after}}$  are determined at a read voltage of 0.2 V.

Since biological synapses can feature action potentials of various shapes [10], both triangular and exponential action potentials are biologically plausible. However, a triangular action potential causes a Gaussian shaped STDP function, whereas an exponential action potential also results in an exponential STDP function (see fig. 4.32 and fig. 2.6). An exponential function only uses two fitting parameters, an exponential parameter and a linear scaling factor, and thus can be directly used for a quantitative analysis of the STDP function.

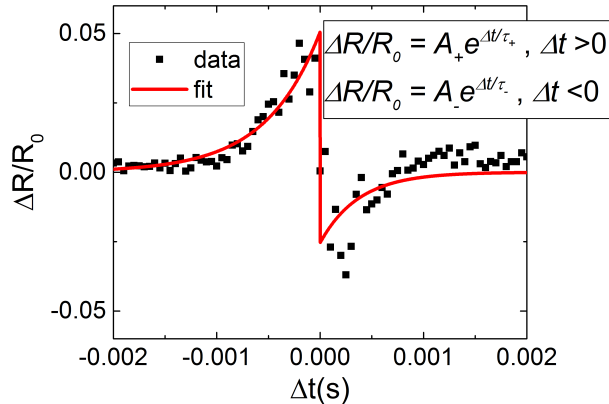


Figure 4.33: A STDP function resulting from exponential voltage spikes can be fitted with two exponential functions for  $\Delta t < 0$  and  $\Delta t > 0$ . The fit provides the two scaling parameters  $A_+$ ,  $A_-$ , and the two exponential parameters  $\tau_+$ ,  $\tau_-$ .

Fig. 4.33 shows a fit of the data of fig. 4.32(b) with the following formula [122]:

$$\frac{\Delta R}{R_0}(\Delta t) = A_+ e^{\frac{\Delta t}{\tau_+}} \quad \text{for } \Delta t > 0 \quad (4.3)$$

$$\frac{\Delta R}{R_0}(\Delta t) = A_- e^{\frac{\Delta t}{\tau_-}} \quad \text{for } \Delta t < 0$$

, with the two linear scaling factors  $A_+$ ,  $A_-$ , and the two exponential parameters  $\tau_+$ ,  $\tau_-$ . These parameters can be used for a quantitative analysis of STDP functions.  $A_+$  and  $A_-$  describe the amount of maximum resistance change and therefore correlate to how fast learning behavior takes place, i.e. how large is the change in resistance for one external stimulus.  $A_+$  corresponds to a gradual SET process and a strengthening of the synaptic connection, whereas  $A_-$  amounts for a gradual RESET and weakening of the synapse.  $\tau_+$  and  $\tau_-$  indicate how strongly the change in resistance of an individual STDP measurement depends on the time difference  $\Delta t$ . Fig. 4.34 depicts the influence of the initial cell resistance  $R_{\text{init}}$  on the cell's learning behavior. For this purpose,  $R_{\text{init}}$  is measured directly before the beginning of each measurement procedure of a STDP function (fabrication protocol B).  $R_{\text{init}}$  can be varied from 2 k $\Omega$  to 120 k $\Omega$  by gradually switching the cells with appropriate voltage pulses. The measurement of each STDP function uses the same pre- and post-synaptic voltage spikes, which are adapted from the exponential spikes used in fig. 4.32 with a total length of 4 ms and a maximum voltage of 2 V. The influence of  $R_{\text{init}}$  on the scaling parameters  $A_+$  and  $A_-$  shown in fig. 4.34(a) gives a clear trend. A higher  $R_{\text{init}}$  leads to larger absolute values of  $A_+$  and  $A_-$  and causes a higher relative change in resistance for a given external stimulus. This can be explained by the fact that the thin filament of a high  $R_{\text{init}}$  is subjected to a higher relative resistance change compared to a thicker filament for a similar voltage pulse. The high variation of the scaling parameters for higher  $R_{\text{init}}$  is most probably caused by statistical randomness of a system with limited number of atoms [19]. For thin filaments with a diameter in the nanometer range, this effect increases. Fig. 4.34(b) shows that the exponential parameters  $\tau_+$  and  $\tau_-$  are independent of  $R_{\text{init}}$ , since they probably mostly depend on the length of the applied voltage spikes.

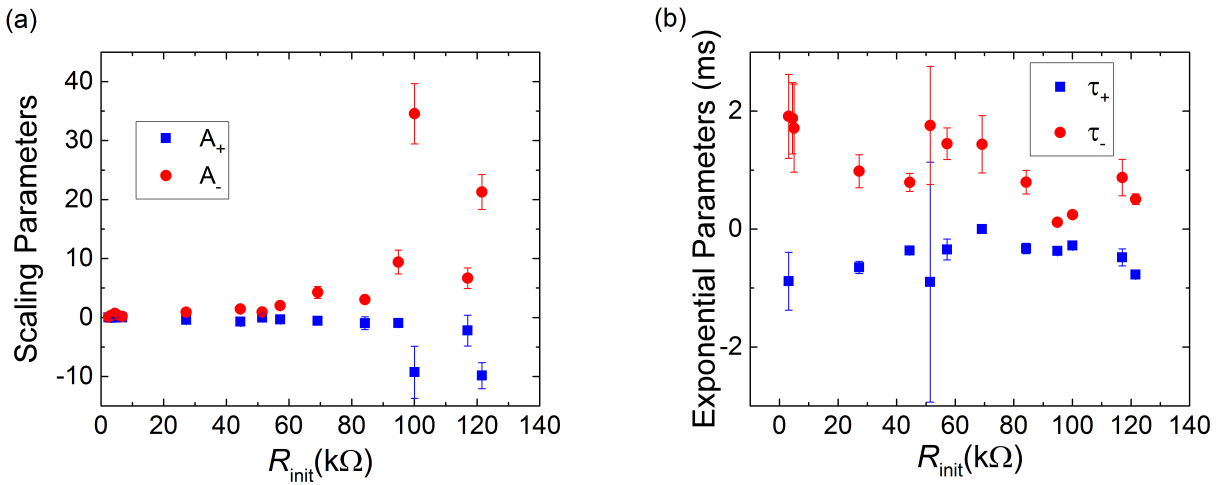


Figure 4.34: (a) Linear scaling factors  $A_+$ ,  $A_-$ , and (b) exponential parameters  $\tau_+$ ,  $\tau_-$  versus  $R_{\text{init}}$ , the initial cell resistance before the STDP measurement. Each pair of data points for  $A_+$ ,  $A_-$  and  $\tau_+$ ,  $\tau_-$  corresponds to one STDP function. The error bars depict the error of the fit and correspond to measurement noise in the STDP function.

Fig. 4.35 shows the influence of the voltage amplitude of the exponential pre- and post-synaptic action potentials on the fitting parameters of the STDP function of a printed Ag/SOG/ PE-DOT:PSS cell (fabrication protocol B). The exponential voltage spikes are similar to those used for the STDP shown in fig. 4.32 with a total length of 4 ms and varying maximum voltage. The linear scaling parameters  $A_+$  and  $A_-$  in dependence of the maximum voltage of the spikes is shown in fig. 4.35(a). Between 1 V and 2 V,  $A_+$  and  $A_-$  and therefore also the relative change in resistance for the corresponding STDP function is negligible, because the accumulative voltage of pre- and post-synaptic voltage spike do not exceed the voltage switching threshold of the memory cell. Between 2 V and 3.2 V an increase in voltage also leads to increasing absolute values of  $A_+$  and  $A_-$ . Here, the accumulative voltage of the overlap of pre- and post-synaptic spike, which is almost twice the value of the maximum individual spike amplitude for small  $\Delta t$ , is sufficient to trigger a considerable change in resistance. The change in resistance depends on the maximum voltage of the accumulated voltage spike (see also fig. 4.9(a)) and therefore  $A_+$  and  $A_-$  scale with the maximum voltage. A spike voltage above 3.2 V is too high to generate evaluable STDP functions, since it often leaves the memory cell at a low resistance state with a barely reversible ON state. The exponential parameters  $\tau_+$  and  $\tau_-$  shown in fig. 4.35(b) are subjected to measurement noise and do not exhibit a dependence on the spike voltage.

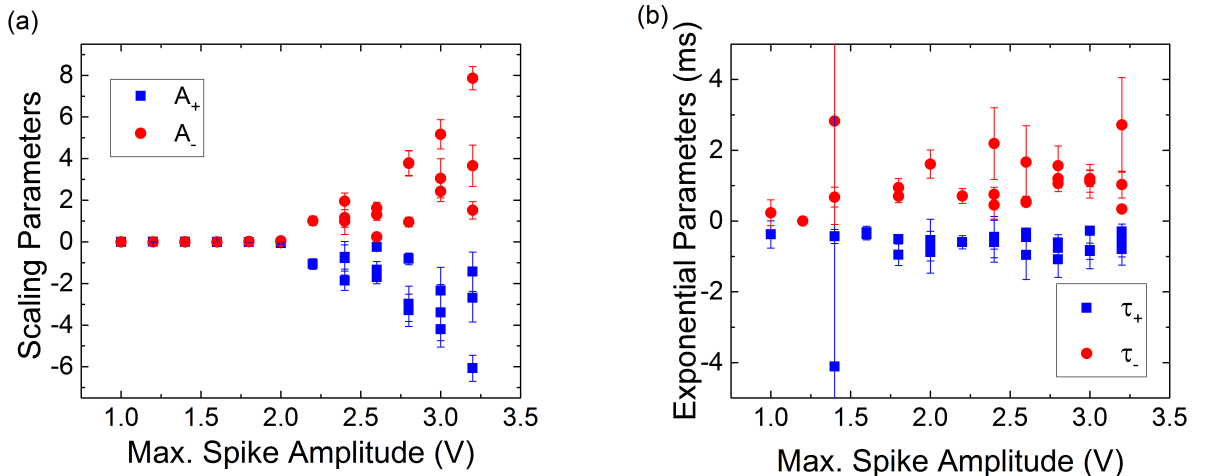


Figure 4.35: (a) Linear scaling factors  $A_+$ ,  $A_-$ , and (b) exponential parameters  $\tau_+$ ,  $\tau_-$  plotted against the maximum voltage of the exponential pre- and post-synaptic voltage spikes. Each pair of data points for  $A_+$ ,  $A_-$  and  $\tau_+$ ,  $\tau_-$  corresponds to one STDP function. The error bars are the errors of the fit. (a) Voltages below a threshold of 2 V are too small to trigger a significant change in resistance and lead to negligible  $A_+$  and  $A_-$ . Above this voltage threshold,  $A_+$  and  $A_-$  increase with the voltage. (b)  $\tau_+$  and  $\tau_-$  are voltage-independent.

As a conclusion, the quantitative analysis of the STDP functions with the parameters  $A_+$ ,  $A_-$ , and  $\tau_+$ ,  $\tau_-$  gives important information on how internal ( $R_{\text{init}}$  of the cell) and external parameters (maximum voltage of spikes) influence the synaptic plasticity. Especially the linear scaling factors  $A_+$  and  $A_-$  show a strong dependence on  $R_{\text{init}}$  and the spike voltage.  $A_+$  and  $A_-$  correlate to the relative change in the cell's resistance for one external stimulus and thus determine

the learning speed, i.e. how many voltage spikes are needed to sufficiently program a synapse to a specific resistance value.

If one wants to work with a specific ANN, it is beneficial to know this "learning speed" of the individual synapses, since it determines how fast the ANN reacts to inputs of training data sets and how stable it is in the trained configuration. Hence, it is possible to tailor the applied voltage spikes to control the weight adjustment of the ANN. Thus, during the training process, the synapse weight adjustment caused by the cost function minimization can be optimized.

#### 4.5.3 Summary and Discussion

For a better interpretation of the results on the neuromorphic applications, it is advantageous to bear in mind the relation between ReRAM technology and the field of neuromorphic computing. Similar to almost all emerging technologies, ReRAM undergo a so-called hype cycle with a hype of overestimation at the beginning (the "peak of inflated expectations") followed by the "trough of disillusionment", during which the first hype is reversed as it is found out that the new technology cannot meet the first exalted expectations. As the technology matures, a stable "plateau of productivity" is reached. [103]

For ReRAM technology the inflated expectations have been possible application as universal memory with its non-volatility combined with fast read and write times. However, the high variation of the ReRAM cells lead into the "trough of disillusionment", when it became clear that large ReRAM crossbar arrays feature a challenging cell-to-cell and cycle-to-cycle variation for the usage as conventional memory. Variation is not similarly detrimental in the framework of neuromorphic computing, since it occurs frequently in biological computing systems [56]. Therefore, neuromorphic applications are widely seen as suitable applications for ReRAM technology and it is hardly predictable if this path will lead to a new "peak of inflated expectations" or a stable "plateau of productivity". [110]

The experimental results confirm that printed cells show synaptic plasticity and could therefore be used for neuromorphic computing despite a considerable variation in switching (see for example fig. 4.34). However, since the main disadvantage of the printing process lies within its large feature sizes, the fields of application for printed ReRAM will favor small systems. Printed ReRAM devices will most probably focus on applications which do not require large memory arrays. Thus, ReRAM as hardware for large ANN for Big Data analysis would most possibly still be fabricated by thin film technology combined with lithography. Printed ReRAM could be interesting for small neuromorphic devices for example in the field of edge computing.

## Chapter 5

# Summary and Outlook

This thesis presents the first reported fully inkjet-printed, bipolar ECM cells. As flexible electronics still lack appropriate printed memory for numerous applications in the framework of the "Internet of Things", the fully printed memory has the potential to close this gap. Device parameters such as a yield of 80 %, endurance of more than 1100 switching cycles, and retention of  $8.65 \cdot 10^5$  s could already meet the demands for applications in the field of printed electronics. Driven by this motivation to establish memory cells for different application scenarios, different cell structures are established to fit specific demands for possible applications:

- Ag nanoparticles/SOG/PEDOT:PSS cells show the highest endurance and retention as well as excellent flexibility
- PEDOT:PSS/Ag nanoparticle seed layer/SOG/PEDOT:PSS cells feature a high degree of transparency for applications in the field of transparent electronics. However, this design has the drawback of a lower endurance
- Another approach for transparent devices are Ag nanowires/SOG/PEDOT:PSS cells, which show a potential for even enhanced flexibility
- Ag nanoparticles/WO<sub>3</sub>/PEDOT:PSS cells use sinter-free WO<sub>3</sub> nanoparticles as insulating layer and therefore can serve as potential candidates for completely sinter-free memory cells

Local switching with CAFM as well as subsequent FIBSEM measurements prove the filamentary type of switching and confirm the theoretical switching mechanism. A diffusion model based on Fick diffusion is established to model the radial diffusion of the Ag filament, the underlying mechanism which determines the retention of the ON state. The model is able to quantitatively describe the diffusion process and can be used for a predictive retention analysis.

Investigations on the mechanical flexibility of the memory cells are performed with the in-house built rotate-to-bend bending setup. Static as well as repeated, cyclic bending are applied on the individual electrode materials and complete ECM cells. The bending experiments show the cells' excellent flexibility with stable switching down to at least 2 mm bending radius for static bending and 500,000 bending cycles with 3 mm radius for cyclic bending.

STDP measurements show that the printed memory cells can be used as artificial synapses for a direct implementation of ANNs. The cells' reaction on the external action potentials, i.e. their learning behavior, is quantified. It is crucial to understand this learning behavior, since it directly influences the speed of the learning process. These findings can be transferred to the training of printed ANNs.

This work establishes the printing process for various application-specific ECM cell structures, but still leaves room for further optimization and open questions.

- The standard Ag nanoparticles/SOG/PEDOT:PSS cell design shows the most promising characteristics. The still improvable retention as Achilles heel of the non-volatile ECM could be enhanced by reducing the diffusion constant of Ag in the insulating material. For SOG, this could probably be achieved with different sintering protocols or changing the type of SOG. Possibly, a silicate-based SOG combined with higher sintering temperatures could enable higher retention times.
- For both transparent cell structures a tradeoff has to be found between degree of transparency and endurance depending on the requirements of the application. A transparent ReRAM device requiring a high endurance may have to suffice with a lower transparency and vice versa.
- The sinter-free  $\text{WO}_3$  nanoparticles as insulating layer could be combined with a sinter-free active bottom electrode for a direct demonstration of completely sinter-free memory cells.

Concerning specific applications, the next step would be the transfer from individual memory cells to a crossbar array. Thus, the sneak path issue can be evaluated and, if necessary, selector devices could be added. A change from the bipolar cell design to a unipolar Ag/SOG/Ag structure would only require diodes as selectors and would therefore simplify the design of larger crossbar arrays. Including printed batteries as a power source together with a printed sensor would be the next required step towards a self-sustaining device. Furthermore, fully printed ECM crossbars could then for the first time directly implement ANNs and put the findings on the adjustment of the learning process into action.

## Appendix A

# Fabrication Parameters

All the inks are diluted with solvents as described in subsection 2.3.2 and printed at room temperature. Only the PEDOT:PSS ink *Clevios<sup>TM</sup> P Jet N V2* has to be filtered with a *FIL-001* filter from *Fujifilm Dimatix* with a pore size of 0.2  $\mu\text{m}$  in order to prevent clogging of the nozzles. For the sintering process a *PEO 601* furnace from *ATV Technologie GmbH* is used, which can heat at ambient atmosphere or purged with nitrogen.

Fabrication Protocols:

A A Si Wafer with 100 nm SiO<sub>2</sub> serves as substrate. The Ag bottom electrode is printed as a 1 cm long line with 1 jet and a drop spacing of 20  $\mu\text{m}$  at room temperature. Sintering takes place at 200°C for 1 hour under ambient atmosphere. The *Honeywell Accuglass<sup>TM</sup> T-11 111* SOG is printed as a 8 mm long line on top of the Ag with 1 jet and a drop spacing of 5  $\mu\text{m}$  at room temperature. Sintering takes place at 200°C to 400°C for 1 hour under nitrogen atmosphere. 5 layers of the polymer top electrode are printed as 2 mm long lines perpendicularly on top of the Ag/SOG line with 1 jet and a drop spacing of 25  $\mu\text{m}$  at a substrate temperature of 60°C. No sintering step is applied.

B A 125  $\mu\text{m}$  thick PEN foil *Teonex<sup>®</sup> Q65HA* from *Dupont Teijin Film* is used as substrate. The Ag bottom electrode is printed as a 1 cm long line with 1 jet and a drop spacing of 5  $\mu\text{m}$  at room temperature. Sintering takes place at 200°C for 10 min under nitrogen atmosphere. The *Honeywell Accuglass<sup>TM</sup> T-11 111* SOG is printed as a 8 mm long line on top of the Ag with 1 jet and a drop spacing of 5  $\mu\text{m}$  at room temperature. Sintering takes place at 200°C for 1 hour under nitrogen atmosphere. The polymer top electrode is printed as 2 mm long lines perpendicularly and 5 layers on top of the Ag/SOG line with 1 jet and a drop spacing of 25  $\mu\text{m}$  at a substrate temperature of 60°C. No sintering step is applied.

C A Si Wafer with 100 nm SiO<sub>2</sub> is used as substrate. The bottom electrode consists of one layer of PEDOT:PSS to ensure conductivity and a submonolayer of sparse Ag nanoparticles. The PEDOT:PSS is printed as a 1 cm long line with 2 jets and a drop spacing of 10  $\mu\text{m}$  at a substrate temperature of 60°C and sintered at 150°C for 30 min under ambient atmosphere. The Ag nanoparticle ink is fabricated by Julian Kund at the Chemistry Business Unit

at the University of Applied Sciences Munich by microwave-assisted synthesis from Ag acetate in ethylene glycol. 10.47 mg Ag acetate from *Alfa Aesar* are dispersed in 5.04 g ethylene glycol, which serves as solvent and reducing agent during the synthesis. 11.03 mg polyvinylpyrrolidone from *Ambresco* is added as stabilizer. The synthesis takes place in a *CEM Discover SP 909155* microwave system for 10 min with 300 W power at 100°C under nitrogen atmosphere. Dynamic light scattering measurements show an average particle diameter of 53 nm. The Ag nanoparticle ink is printed as a 1 cm long line on top of the PEDOT:PSS with 1 jets and a drop spacing of 20  $\mu\text{m}$  at a substrate temperature of 40°C. During printing, the cartridge is heated up to 55°C to reduce the high viscosity of the ethylene glycol and optimize the printability. The Accuglass<sup>TM</sup>P-5S SOG is printed as a 8 mm long line on top of the Ag with 1 jet and a drop spacing of 5  $\mu\text{m}$  at room temperature. Sintering takes place at 150°C for 1 hour under nitrogen atmosphere. The polymer top electrode is printed as 2 mm long lines perpendicularly and 4 layers on top of the Ag/SOG line with 2 jets and a drop spacing of 10  $\mu\text{m}$  at a substrate temperature of 60°C. No sintering step is applied.

D A Si Wafer with 100 nm  $\text{SiO}_2$  serves as substrate. The Ag nanowire bottom electrode (diluted *ClearOhm<sup>®</sup> ink-Y* from *Cambrios*) is printed as a 1 cm long line with 1 jet, 10 layers, and a drop spacing of 10  $\mu\text{m}$  at room temperature. Sintering takes place at 140°C for 1 hour under nitrogen atmosphere. The *Honeywell Accuglass<sup>TM</sup>T-11 111* SOG is printed as a 8 mm long line on top of the Ag with 1 jet and a drop spacing of 5  $\mu\text{m}$  at room temperature. Sintering takes place at 140°C for 1 hour under nitrogen atmosphere, since the Ag nanowires melt at higher temperatures. Five layers of the polymer top electrode are printed as 2 mm long lines perpendicularly on top of the Ag/SOG line with 1 jet and a drop spacing of 25  $\mu\text{m}$  at a substrate temperature of 60°C. No sintering step is applied.

E A 125  $\mu\text{m}$  thick PEN foil *Teonex<sup>®</sup> Q65HA* from *Dupont Teijin Film* serves as substrate. The Ag bottom electrode (*UTDots AGIJ*) is printed as a 1 cm long line with 1 jet and a drop spacing of 20  $\mu\text{m}$  at room temperature. Sintering takes place at 200°C for 1 hour under ambient atmosphere. The *Avantama P-10*  $\text{WO}_3$  nanoparticle ink is printed as a 8 mm long line on top of the Ag with 4 jets, 5 layers, and a drop spacing of 5  $\mu\text{m}$  at room temperature. A drying step takes place at 80°C for 1 hour under nitrogen atmosphere. The polymer top electrode is printed as 2 mm long lines perpendicularly and 5 layers on top of the Ag/ $\text{WO}_3$  line with 2 jets and a drop spacing of 25  $\mu\text{m}$  at a substrate temperature of 60°C. No sintering step is applied.

F A PEN foil *Teonex<sup>®</sup> Q83* from *Dupont Teijin Film* with the thicknesses of either 25  $\mu\text{m}$ , 50  $\mu\text{m}$ , or 125  $\mu\text{m}$  is used as substrate. The 6 mm long Ag bottom electrode consists of either diluted *UTDots AGIJ* nanoparticle or *ClearOhm<sup>®</sup> ink-Y* nanowire ink. The Ag nanoparticle ink is printed with 1 jet and a drop spacing of 5  $\mu\text{m}$ . The substrate temperature is set to 60°C to reduce excessive spreading. Sintering takes place at 200°C for 10 min under ambient atmosphere. The An nanowire ink consists of 5 layers printed

at room temperature with 1 jet at a drop spacing of  $10 \mu\text{m}$  and is sintered for 1 hour at  $140^\circ\text{C}$  for 1 hour under nitrogen atmosphere. Due to the different wetting on the *Teonex® Q83*, the 4 mm lines of *Honeywell Accuglass™ T-11 111* SOG have to be printed with 5 jets and a drop spacing of  $5 \mu\text{m}$  in print direction and  $50 \mu\text{m}$  perpendicular to the print direction. The SOG is sintered for 1 hour at  $140^\circ\text{C}$  under nitrogen atmosphere. Five layers of the polymer top electrode are printed as 2 mm long lines perpendicularly on top of the Ag/SOG line with 1 jet and a drop spacing of  $25 \mu\text{m}$  at a substrate temperature of  $60^\circ\text{C}$ . No sintering step is applied.



## Appendix B

### Waveforms for Inkjet Inks

This appendix describes the waveforms used for printing of the individual materials. All materials are printed with the *DMC-11610* cartridge of the *Dimatix DMP2832* printer with a nozzle diameter of  $L_N = 21 \mu\text{m}$ .

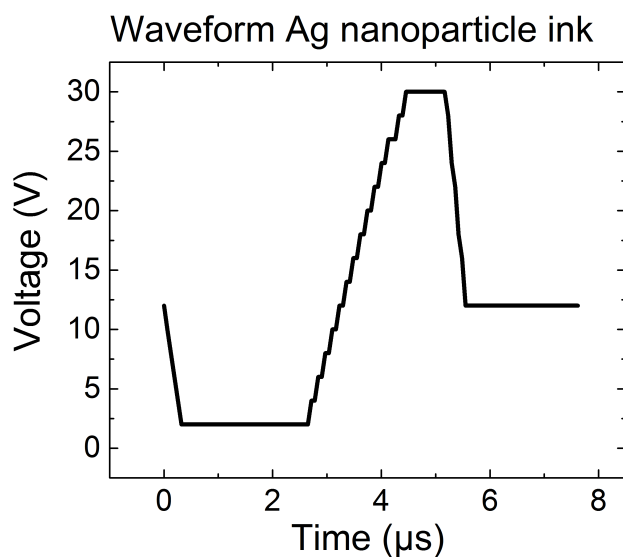


Figure B.1: Waveform for *UTDots AGIJ* Ag nanoparticle ink with a maximum voltage of 30 V and a jetting frequency of 5 kHz.

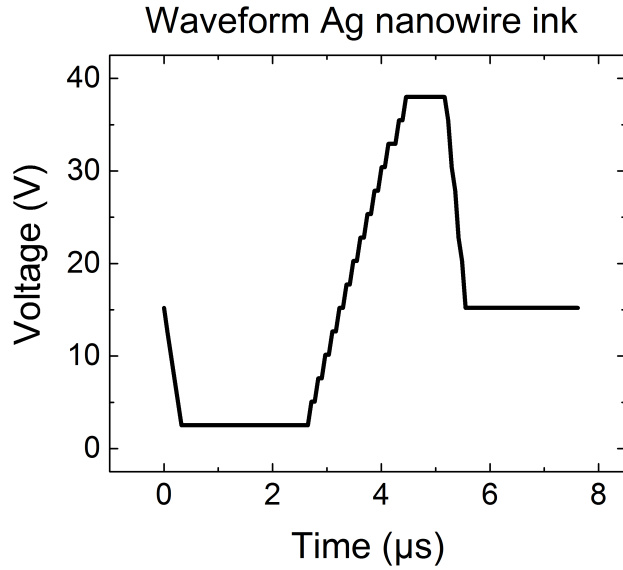


Figure B.2: Waveform for *Clear Ohm® ink-Y* Ag nanowire ink with a maximum voltage of 38 V and a jetting frequency of 5 kHz.

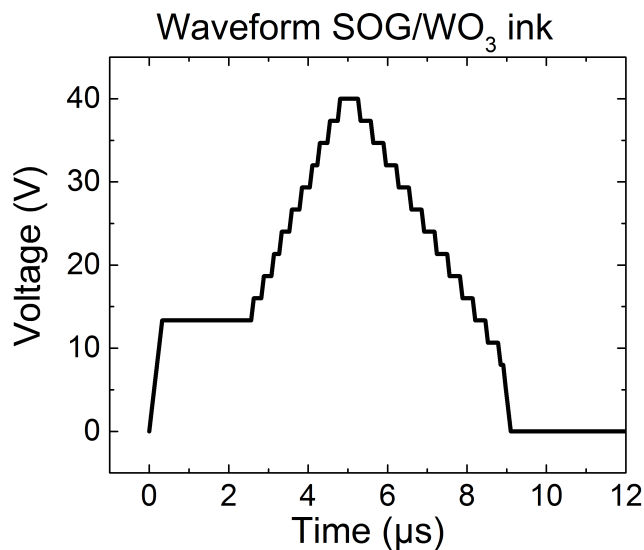


Figure B.3: Waveform for *Honeywell Accuglass™SOG* and *Avantama P-10 WO<sub>3</sub>* nanoparticle ink with a maximum voltage of 40 V and a jetting frequency of 2.3 kHz. Since both inks show a low viscosity and a similar Z number, the same waveform can be used for printing both materials.

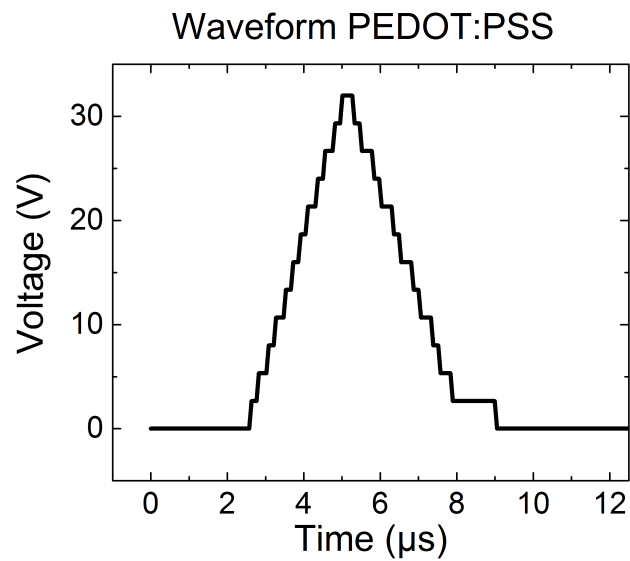


Figure B.4: Waveform for *Clevios<sup>T</sup> M P Jet N V2* PEDOT:PSS ink with a maximum voltage of 32 V and a jetting frequency of 5 kHz.



## Appendix C

# Normalization of Spike-Timing-Dependent Plasticity Function

A STDP function plots the normalized change in resistance  $\frac{\Delta R}{R_0}$  versus the time difference  $\Delta t$  between the pre- and post-synaptic voltage spike. For the data analysis the definition of the normalization parameter  $R_0$  is crucial. For each data point in a STDP plot  $R_{before}$  and  $R_{after}$  are compared and the smaller value is set as  $R_0$  (see equation 4.2). In literature, many different approaches for this scaling of the STDP function can be found. Matveyev et al. do not use a scaling factor at all [90], Campbell et al. use the minimum resistance measured for the device over all  $\Delta t$  values [20], and Prezioso et al. choose  $R_{before}$  as normalization parameter [109]. It is worth noticing that in literature a STDP plot often shows a normalized change in conductance versus  $\Delta t$  [12][88], which, however, leads to the same considerations.

For  $\Delta R$  small compared to  $R_0$ , the choice of  $R_0$  does not play a decisive role. However, for  $\Delta R$  in the same range as  $R_0$ , the choice of the normalization parameter significantly influences the shape of the STDP function. Fig. C.1 shows the STDP function for the identical data set for (a) $\min(R_{before}(\Delta t), R_{after}(\Delta t))$  and (b) $R_{before}(\Delta t)$  as normalization parameter in equation 4.2. The data set is one STDP measurement shown in fig. 4.35 for a maximum spike amplitude of 3.2 V. While (a) shows a symmetric STDP function,  $R_{before}(\Delta t)$  as scaling parameter in (b) causes a distortion and underrepresentation of the exponential branch for positive  $\Delta t$ , i.e. a gradual SET process. For negative  $\Delta t$ , the cell undergoes a gradual RESET process ( $R_{before} < R_{after}$ ). Therefore,  $R_{before}$  is equal to  $\min(R_{before}, R_{after})$ . The gradual SET process for positive  $\Delta t$  leads to  $R_{before} > R_{after}$  and thus,  $R_{before}$  is larger than  $\min(R_{before}, R_{after})$ . This causes a skewing of the exponential branch for positive  $\Delta t$ , where the absolute value of  $\frac{\Delta R}{R_0}$  cannot exceed the value 1.

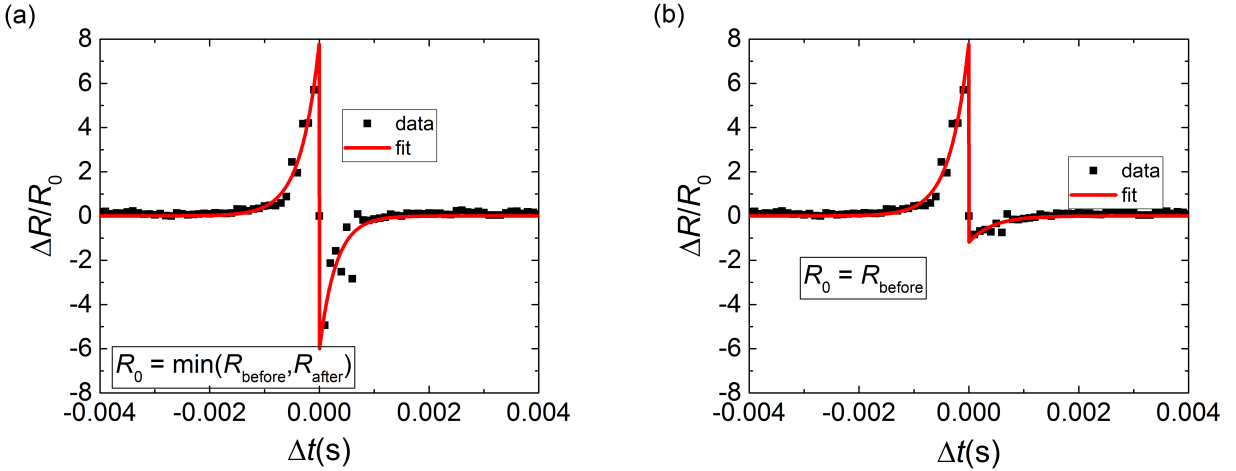


Figure C.1: STDP function for (a)  $\min(R_{\text{before}}(\Delta t), R_{\text{after}}(\Delta t))$  and (b)  $R_{\text{before}}(\Delta t)$  as normalization parameter in equation 4.2. (b)  $R_{\text{before}}(\Delta t)$  as scaling parameter causes a distortion and underrepresentation of the exponential branch for positive  $\Delta t$ , i.e. a gradual SET process.

Fig. C.2 shows the influence of the normalization on the quantitative analysis of the fitting parameters  $A_+$  and  $A_-$  with the same data set also used in fig. 4.35. Fig. C.2(a) depicts a data plot symmetric to  $y = 0$  due to symmetric STDP functions with  $R_0 = \min(R_{\text{before}}(\Delta t), R_{\text{after}}(\Delta t))$ . In fig. C.2(b), the data points of  $A_-$  are identical, but the values of  $A_+$  are skewed due to the underrepresentation of the SET process caused by  $R_0 = R_{\text{before}}$ . As a conclusion, the different normalization schemes found in literature are not flawed. However, the normalization with  $R_0 = \min(R_{\text{before}}(\Delta t), R_{\text{after}}(\Delta t))$  in equation 4.2 allows a more balanced quantitative analysis of STDP measurements.

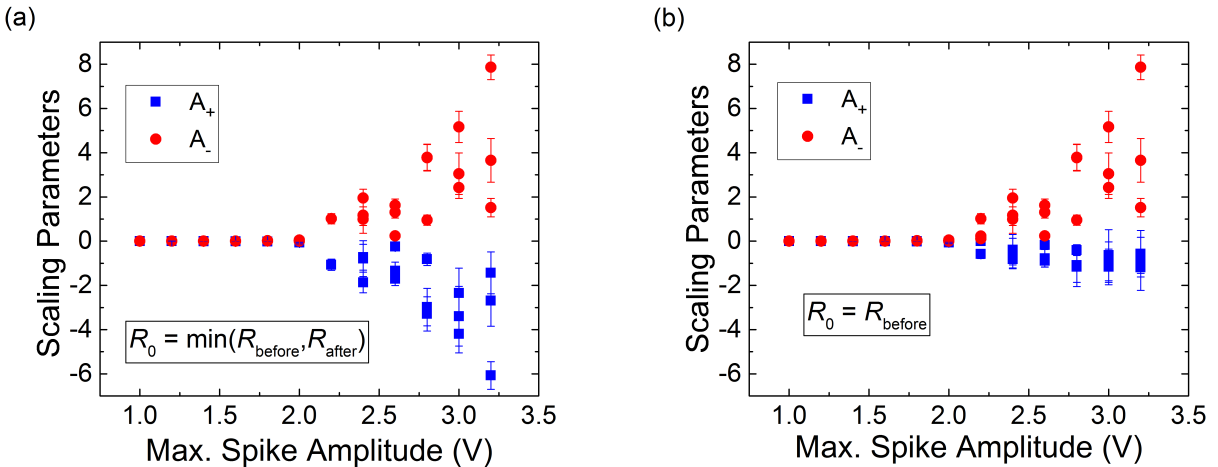


Figure C.2: Data set of fig. 4.35 with (a)  $\min(R_{\text{before}}(\Delta t), R_{\text{after}}(\Delta t))$  and (b)  $R_{\text{before}}(\Delta t)$  as normalization parameter. The fitting parameters  $A_+$  are skewed in (b) due to the underrepresentation in the data analysis.

## Appendix D

# Publications and Conference Contributions

Substantial parts of this thesis have already been published as journal papers or presented at conferences. Therefore, published papers and conference contributions are listed below.

## Publications

- G. Kolhatkar, B. Mittermeier, Y. L. Gonzalez Hernandez, F. Ambriz-Vargas, M. Weismueller, A. Sarkissian, C. Gomez-Yanez, R. Thomas, C. Schindler, A. Ruediger,  $\text{BiFe}_{1-x}\text{Cr}_x\text{O}_3$  ferroelectric tunnel junctions for neuromorphic systems. submitted 2019
- B. Mittermeier, A. Bednar, M. Kaiser, A. Ruediger, C. Schindler, Comparison of Spin-on-glass and  $\text{WO}_3$  as insulating layer for printed resistive memory devices. *Materials Technology*, 20, 1, 2019
- M. Kracklauer, F. Ambriz-Vargas, G. Kolhatkar, B. Huber, C. Schindler, A. Ruediger, Oxygen-filament-based resistive switching in  $\text{Hf}_{0.5}\text{Zr}_{0.5}\text{O}_2$  thin films for non volatile memory, *Advanced Materials Letters*, accepted 2018
- B. Huber, J. Schober, M. Kaiser, A. Ruediger, C. Schindler, Rotate-to-bend setup for fatigue bending tests on inkjet-printed silver lines. *Flexible and Printed Electronics (IoP)*, 3, Nr. 3, 035005, 2018
- B. Huber, J. Schober, A. Kreuzer, M. Kaiser, A. Ruediger, C. Schindler, Inkjet-printed resistive memory cells for transparent electronics. *Microelectronic Engineering*, 194, 85, 2018
- G. Kolhatkar, F. Ambriz-Vargas, B. Huber, R. Thomas, A. Ruediger, Thermionic emission based resistive memory with ultrathin ferroelectric  $\text{BiFe}_{1-x}\text{Cr}_x\text{O}_3$  films deposited by mineralizer-free microwave-assisted hydrothermal synthesis. *Cryst. Growth Des.*, 18 (3), 1864, 2018

- B. Huber, P. B. Popp, M. Kaiser, A. Ruediger, C. Schindler, Fully inkjet printed flexible resistive memory. *Applied Physics Letters*, 110(14), 143503, 2017

## Conference Contributions

- Poster: B. Huber, J. Schober, M. Kaiser, A. Kreuzer, A. Ruediger, C. Schindler, Flexibility and retention analysis of fully inkjet-printed resistive memory, *MEMRISYS Conference*, Beijing, 2018
- Talk: B. Huber, S. Pschierer, M. Kaiser, A. Ruediger, C. Schindler, Inkjet-printed flexible Conductive Bridge RAM, *ENVM Conference*, Aix-en-Provence, 2017
- Talk: B. Huber, J. Schober, M. Hange, S. Pschierer, M. Kaiser, A. Ruediger, C. Schindler, Inkjet-printed resistive memory cells for transparent electronics, *MEMRISYS Conference*, Athens, 2017
- Talk: B. Huber, M. Kaiser, P. Popp, A. Ruediger, C. Schindler, Inkjet-printed Resistively Switching Memory Devices, *FORUM BE-FLEXIBLE*, Munich, 2016
- Talk: B. Huber, M. Kaiser, T. Kuehlewind, V. Juhart, A. Vass, C. Schindler, Inkjet Printing of Redox-based Resistive Switching Memory, *9th Nanocongress for next Generations*, Manchester, 2016  
Best Young Researcher Presentation Award

# Bibliography

- [1] IEEE international roadmap for devices and systems: Beyond CMOS. 2017, retrieved on 2018/12/12 from [https://irds.ieee.org/images/files/pdf/2017/2017IRDS\\_BC.pdf](https://irds.ieee.org/images/files/pdf/2017/2017IRDS_BC.pdf).
- [2] N. Ahner, S. E. Schulz, F. Blaschta, and M. Rennau. Optical, electrical and structural properties of spin-on MSQ low-k dielectrics over a wide temperature range. *Microelectronic Engineering*, 85(10):2111–2113, 2008.
- [3] L. C. Aiello and P. Wheeler. The expensive-tissue hypothesis: The brain and the digestive system in human and primate evolution. *Current Anthropology*, 36(2):199–221, 1995.
- [4] A. Albrecht, A. Rivadeneyra, A. Abdellah, P. Lugli, and J. F. Salmerón. Inkjet printing and photonic sintering of silver and copper oxide nanoparticles for ultra-low-cost conductive patterns. *Journal of Materials Chemistry C*, 4(16):3546–3554, 2016.
- [5] S. Ali, J. Bae, C. H. Lee, K. H. Choi, and Y. H. Doh. All-printed and highly stable organic resistive switching device based on graphene quantum dots and polyvinylpyrrolidone composite. *Organic Electronics*, 25:225–231, 2015.
- [6] M. L. Allen, M. Aronniemi, T. Mattila, A. Alastalo, K. Ojanpera, M. Suhonen, and H. Seppä. Electrical sintering of nanoparticle structures. *Nanotechnology*, 19(17):175201, 2008.
- [7] R. C. Atkinson and R. M. Shiffrin. Human memory: A proposed system and its control processes. *Psychology of learning and motivation*, (Vol. 2):89–195, 1968.
- [8] K. Bädeker. Über die elektrische Leitfähigkeit und die thermoelektrische Kraft einiger Schwermetallverbindungen. *Annalen der Physik*, 327(4):749–766, 1907.
- [9] K.-J. Baeg, D. Khim, J. Kim, B.-D. Yang, M. Kang, S.-W. Jung, I.-K. You, D.-Y. Kim, and Y.-Y. Noh. High-performance top-gated organic field-effect transistor memory using electrets for monolithic printed flexible nand flash memory. *Advanced Functional Materials*, 22(14):2915–2926, 2012.
- [10] B. P. Bean. The action potential in mammalian central neurons. *Nature reviews. Neuroscience*, 8(6):451–465, 2007.

- [11] J. D. Berry, M. J. Neeson, R. R. Dagastine, D. Y. Chan, and R. F. Tabor. Measurement of surface and interfacial tension using pendant drop tensiometry. *Journal of Colloid and Interface Science*, 454:226–237, 2015.
- [12] G.-Q. Bi and M.-M. Poo. Synaptic modifications in cultured hippocampal neurons: Dependence on spike timing, synaptic strength, and postsynaptic cell type. *The Journal of Neuroscience*, 18(24):10464–10472, 1998.
- [13] C. M. Bishop. *Pattern recognition and machine learning*. Information science and statistics. Springer, New York, NY, corrected at 8th printing 2009 edition, 2009.
- [14] R. H. Bishop, editor. *The mechatronics handbook*. The electrical engineering handbook series. CRC Press, Boca Raton, Fla, 2002.
- [15] K. Black, J. Singh, D. Mehta, S. Sung, C. J. Sutcliffe, and P. R. Chalker. Silver ink formulations for sinter-free printing of conductive films. *Scientific reports*, 6:20814, 2016.
- [16] S. G. Bratsch. Standard electrode potentials and temperature coefficients in water at 298.15 K. *Journal of Physical and Chemical Reference Data*, 18(1):1–21, 1989.
- [17] P. Buffat and J.-P. Borel. Size effect on the melting temperature of gold particles. *Physical Review A*, 13(6):2287–2298, 1976.
- [18] D. R. Cairns and G. P. Crawford. Electromechanical properties of transparent conducting substrates for flexible electronic displays. *Proceedings of the IEEE*, 93(8):1451–1458, 2005.
- [19] A. Calderoni, S. Sills, and N. Ramaswamy. Performance comparison of O-based and Cu-based ReRAM for high-density applications. In *2014 IEEE 6th International Memory Workshop (IMW)*, pages 1–4.
- [20] K. A. Campbell, K. T. Drake, and E. H. Barney Smith. Pulse shape and timing dependence on the spike-timing dependent plasticity response of ion-conducting memristors as synapses. *Frontiers in bioengineering and biotechnology*, 4:97, 2016.
- [21] M. J. Catenacci, P. F. Flowers, C. Cao, J. B. Andrews, A. D. Franklin, and B. J. Wiley. Fully printed memristors from Cu–SiO<sub>2</sub> core–shell nanowire composites. *Journal of Electronic Materials*, 20:343, 2017.
- [22] J. S. Chang, A. F. Facchetti, and R. Reuss. A circuits and systems perspective of organic/printed electronics: Review, challenges, and contemporary and emerging design approaches. *IEEE Journal on Emerging and Selected Topics in Circuits and Systems*, 7(1):7–26, 2017.
- [23] M. W. Chase. *NIST-JANAF thermochemical tables*. American Institute of Physics, Woodbury, NY, 4. ed. edition, 1998.

- [24] C. Chiang and D. B. Fraser. Understanding of spin-on-glass (SOG) properties from their molecular structure: VLSI multilevel interconnection conference. *Proceedings., Sixth International IEEE*, pages 397–403, 1989.
- [25] F.-C. Chiu. A review on conduction mechanisms in dielectric films. *Advances in Materials Science and Engineering*, 2014(7):1–18, 2014.
- [26] K. H. Choi, M. Mustafa, K. Rahman, B. K. Jeong, and Y. H. Doh. Cost-effective fabrication of memristive devices with ZnO thin film using printed electronics technologies. *Applied Physics A*, 106(1):165–170, 2012.
- [27] W. K. Choi and S. Y. Baek. Study on platinum coating depth in focused ion beam diamond cutting tool milling and methods for removing platinum layer. *Materials (Basel, Switzerland)*, 8(9):6498–6507, 2015.
- [28] J. Crank. *The mathematics of diffusion*. Clarendon Press, Oxford, 2. ed., reprint edition, 1976.
- [29] T. B. T. Dao, K. N. Pham, Y.-L. Cheng, S. S. Kim, and B. T. Phan. Correlation between crystallinity and resistive switching behavior of sputtered  $\text{WO}_3$  thin films. *Current Applied Physics*, 14(12):1707–1712, 2014.
- [30] H. T. Davis and W. J. Kirkham. A new table of the zeros of the bessel functions  $J_0(x)$  and  $J_1(x)$  with corresponding values of  $J_1(x)$  and  $J_0(x)$ . *Bulletin of the American Mathematical Society*, 33(6):760–773, 1927.
- [31] M. P. de Jong, L. J. van IJzendoorn, and M. J. A. de Voigt. Stability of the interface between indium-tin-oxide and poly(3,4-ethylenedioxythiophene)/poly(styrenesulfonate) in polymer light-emitting diodes. *Applied Physics Letters*, 77(14):2255–2257, 2000.
- [32] Deegan, R. D., Bakajin, O., Dupont, T. F., Huber, G., Nagel, S. R., & Witten, T. A. Capillary flow as the cause of ring stains from dried liquid drops. *Nature*, (389(6653)):827–829, 1997.
- [33] C. Y. Dong, D. S. Shang, L. Shi, J. R. Sun, B. G. Shen, F. Zhuge, R. W. Li, and W. Chen. Roles of silver oxide in the bipolar resistance switching devices with silver electrode. *Applied Physics Letters*, 98(7):072107, 2011.
- [34] S. R. Dupont, F. Novoa, E. Voroshazi, and R. H. Dauskardt. Decohesion kinetics of PEDOT: PSS conducting polymer films. *Advanced Functional Materials*, 24(9):1325–1332, 2014.
- [35] A. Fick. Ueber Diffusion. *Annalen der Physik und Chemie*, 170(1):59–86, 1855.
- [36] D. J. Finn, M. Lotya, and J. N. Coleman. Inkjet printing of silver nanowire networks. *ACS applied materials & interfaces*, 7(17):9254–9261, 2015.

- [37] J. E. Fromm. Numerical calculation of the fluid dynamics of drop-on-demand jets. *IBM Journal of Research and Development*, 28(3):322–333, 1984.
- [38] K. Fuchs and N. F. Mott. The conductivity of thin metallic films according to the electron theory of metals. *Mathematical Proceedings of the Cambridge Philosophical Society*, 34(01):100, 1938.
- [39] S. B. Fuller, E. J. Wilhelm, and J. M. Jacobson. Ink-jet printed nanoparticle microelectromechanical systems. *Journal of Microelectromechanical Systems*, 11(1):54–60, 2002.
- [40] A. M. Gaikwad, D. A. Steingart, T. Nga Ng, D. E. Schwartz, and G. L. Whiting. A flexible high potential printed battery for powering printed electronics. *Applied Physics Letters*, 102(23):233302, 2013.
- [41] F. Garnier, R. Hajlaoui, A. Yassar, and P. Srivastava. All-polymer field-effect transistor realized by printing techniques. *Science (New York, N.Y.)*, 265(5179):1684–1686, 1994.
- [42] S. Ghosh-Dastidar and H. Adeli. *Advances in Computational Intelligence: Third Generation Neural Networks: Spiking Neural Networks*, volume 61 of *Advances in intelligent and soft computing*. Springer-Verlag, 1. edition, 2009.
- [43] O. Glushko, M. J. Cordill, A. Klug, and E. List-Kratochvil. The effect of bending loading conditions on the reliability of inkjet printed and evaporated silver metallization on polymer substrates. *Microelectronics Reliability*, 56:109–113, 2016.
- [44] O. Glushko, A. Klug, E. J. List-Kratochvil, and M. J. Cordill. Monotonic and cyclic mechanical reliability of metallization lines on polymer substrates. *Journal of Materials Research*, 32(09):1760–1769, 2017.
- [45] J. R. Greer and R. A. Street. Thermal cure effects on electrical performance of nanoparticle silver inks. *Acta Materialia*, 55(18):6345–6349, 2007.
- [46] X. Guo, C. Schindler, S. Menzel, and R. Waser. Understanding the switching-off mechanism in Ag<sup>+</sup> migration based resistively switching model systems. *Applied Physics Letters*, 91(13):133513, 2007.
- [47] T. Happonen, J. Hakkinen, and T. Fabritius. Cyclic bending reliability of silk screen printed silver traces on plastic and paper substrates. *IEEE Transactions on Device and Materials Reliability*, 15(3):394–401, 2015.
- [48] K. D. Harris, A. L. Elias, and H.-J. Chung. Flexible electronics under strain: A review of mechanical characterization and durability enhancement strategies. *Journal of Materials Science*, 51(6):2771–2805, 2016.
- [49] G. Horowitz. Organic field-effect transistors. *Advanced Materials*, 10(5):365–377, 1998.

- [50] C. W. Hsu, B. Zhen, W. Qiu, O. Shapira, B. G. DeLacy, J. D. Joannopoulos, and M. Soljačić. Transparent displays enabled by resonant nanoparticle scattering. *Nature communications*, 5:3152, 2014.
- [51] B. Huber, P. B. Popp, M. Kaiser, A. Ruediger, and C. Schindler. Fully inkjet printed flexible resistive memory. *Applied Physics Letters*, 110(14):143503, 2017.
- [52] B. Huber, J. Schober, M. Kaiser, A. Ruediger, and C. Schindler. Rotate-to-bend setup for fatigue bending tests on inkjet-printed silver lines. *Flexible and Printed Electronics*, 3(3):035005, 2018.
- [53] B. Huber, J. Schober, A. Kreuzer, M. Kaiser, A. Ruediger, and C. Schindler. Inkjet-printed resistive memory cells for transparent electronics. *Microelectronic Engineering*, 194:85–88, 2018.
- [54] T. Iakymchuk, A. Rosado-Muñoz, J. F. Guerrero-Martínez, M. Bataller-Mompeán, and J. V. Francés-Villora. Simplified spiking neural network architecture and STDP learning algorithm applied to image classification. *EURASIP Journal on Image and Video Processing*, 2015(1):609, 2015.
- [55] D. Ielmini and R. Waser, editors. *Resistive switching: From fundamentals of nanoionic redox processes to memristive device applications*. Wiley-VCH, Weinheim, 2016.
- [56] G. Indiveri, B. Linares-Barranco, R. Legenstein, G. Deligeorgis, and T. Prodromakis. Integration of nanoscale memristor synapses in neuromorphic computing architectures. *Nanotechnology*, 24(38):384010, 2013.
- [57] Institute for Printed Circuits. IPC-6013 standard: Qualification and performance specification for flexible/rigid-flexible printed boards, 9/1/2017.
- [58] Y. Ji, Y. Yang, S.-K. Lee, G. Ruan, T.-W. Kim, H. Fei, S.-H. Lee, D.-Y. Kim, J. Yoon, and J. M. Tour. Flexible nanoporous  $\text{WO}_{3-x}$  nonvolatile memory device. *ACS nano*, 10(8):7598–7603, 2016.
- [59] W.-J. Joo, T.-L. Choi, K.-H. Lee, and Y. Chung. Study on threshold behavior of operation voltage in metal filament-based polymer memory. *The journal of physical chemistry. B*, 111(27):7756–7760, 2007.
- [60] M. Jung, J. Kim, J. Noh, N. Lim, C. Lim, G. Lee, J. Kim, H. Kang, K. Jung, A. D. Leonard, J. M. Tour, and G. Cho. All-printed and roll-to-roll-printable 13.56-MHz-operated 1-bit RF tag on plastic foils. *IEEE Transactions on Electron Devices*, 57(3):571–580, 2010.
- [61] B. J. Kang, C. K. Lee, and J. H. Oh. All-inkjet-printed electrical components and circuit fabrication on a plastic substrate. *Microelectronic Engineering*, 97:251–254, 2012.

- [62] M. Kang, D. Khim, W.-T. Park, J. Kim, J. Kim, Y.-Y. Noh, K.-J. Baeg, and D.-Y. Kim. Synergistic high charge-storage capacity for multi-level flexible organic flash memory. *Scientific reports*, 5:12299, 2015.
- [63] T. Kawahara, K. Ito, R. Takemura, and H. Ohno. Spin-transfer torque RAM technology: Review and prospect. *Microelectronics Reliability*, 52(4):613–627, 2012.
- [64] S. Khan, L. Lorenzelli, and R. S. Dahiya. Technologies for printing sensors and electronics over large flexible substrates: A review. *IEEE Sensors Journal*, 15(6):3164–3185, 2015.
- [65] C. Koch. *Biophysics of computation: Information processing in single neurons*. Computational neuroscience. Oxford Univ. Press, New York, 1. issue as an oxford univ. press paperback edition, 2004.
- [66] J. G. Korvink, P. J. Smith, D.-Y. Shin, O. Brand, G. K. Fedder, C. Hierold, and O. Tabata. *Inkjet-based Micromanufacturing*. Advanced Micro and Nanosystems. Wiley, Hoboken, 2012.
- [67] A. Kosmala, R. Wright, Q. Zhang, and P. Kirby. Synthesis of silver nano particles and fabrication of aqueous Ag inks for inkjet printing. *Materials Chemistry and Physics*, 129(3):1075–1080, 2011.
- [68] M. N. Kozicki, M. Park, and M. Mitkova. Nanoscale memory elements based on solid-state electrolytes. *IEEE Transactions On Nanotechnology*, 4(3):331–338, 2005.
- [69] D. Kuzum, S. Yu, and H.-S. P. Wong. Synaptic electronics: materials, devices and applications. *Nanotechnology*, 24(38):382001, 2013.
- [70] N. A. Lange and J. G. Speight. *Lange's handbook of chemistry*. McGraw-Hill's AccessEngineering. McGraw-Hill Education, New York, 16th ed. edition, 2013.
- [71] H. Lee, D. Lee, J. Hwang, D. Nam, C. Byeon, S. H. Ko, and S. Lee. Silver nanoparticle piezoresistive sensors fabricated by roll-to-roll slot-die coating and laser direct writing. *Optics express*, 22(8):8919–8927, 2014.
- [72] M.-J. Lee, C. B. Lee, D. Lee, S. R. Lee, M. Chang, J. H. Hur, Y.-B. Kim, C.-J. Kim, D. H. Seo, S. Seo, U.-I. Chung, I.-K. Yoo, and K. Kim. A fast, high-endurance and scalable non-volatile memory device made from asymmetric  $Ta_2O_{5-x}/TaO_{2-x}$  bilayer structures. *Nature materials*, 10(8):625, 2011.
- [73] M.-J. Lee, Y. Park, B.-S. Kang, S.-E. Ahn, C. Lee, K. Kim, W. Xianyu, G. Stefanovich, J.-H. Lee, S.-J. Chung, Y.-H. Kim, C.-S. Lee, J.-B. Park, I.-G. Baek, and I.-K. Yoo. 2-stack 1D-1R cross-point structure with oxide diodes as switch elements for high density resistance RAM applications. In *2007 IEEE International Electron Devices Meeting*, pages 771–774.

- [74] M. A. M. Leenen, V. Arning, H. Thiem, J. Steiger, and R. Anselmann. Printable electronics: Flexibility for the future. *physica status solidi (a)*, 206(4):588–597, 2009.
- [75] A. Lenz, H. Kariis, A. Pohl, P. Persson, and L. Ojamäe. The electronic structure and reflectivity of PEDOT:PSS from density functional theory. *Chemical Physics*, 384(1-3):44–51, 2011.
- [76] J. Lewis. Material challenge for flexible organic devices. *Materials Today*, 9(4):38–45, 2006.
- [77] C. Li, M. Hu, Y. Li, H. Jiang, N. Ge, E. Montgomery, J. Zhang, W. Song, N. Dávila, C. E. Graves, Z. Li, J. P. Strachan, P. Lin, Z. Wang, M. Barnell, Q. Wu, R. S. Williams, J. J. Yang, and Q. Xia. Analogue signal and image processing with large memristor crossbars. *Nature Electronics*, 1(1):52–59, 2018.
- [78] H. U. Li and T. N. Jackson. Flexibility testing strategies and apparatus for flexible electronics. *IEEE Transactions on Electron Devices*, 63(5):1934–1939, 2016.
- [79] Y.-T. Li, S.-B. Long, H.-B. Lü, Q. Liu, Q. Wang, Y. Wang, S. Zhang, W.-T. Lian, S. Liu, and M. Liu. Investigation of resistive switching behaviours in  $\text{WO}_3$ -based RRAM devices. *Chinese Physics B*, 20(1):017305, 2011.
- [80] E. Linn, R. Rosezin, C. Kügeler, and R. Waser. Complementary resistive switches for passive nanocrossbar memories. *Nature materials*, 9(5):403–406, 2010.
- [81] D. J. Lipomi, J. A. Lee, M. Vosgueritchian, B. C.-K. Tee, J. A. Bolander, and Z. Bao. Electronic properties of transparent conductive films of PEDOT:PSS on stretchable substrates. *Chemistry of Materials*, 24(2):373–382, 2011.
- [82] Z. Lü, T. Pu, Y. Huang, X. Meng, and H. Xu. Flexible ferroelectric polymer devices based on inkjet-printed electrodes from nanosilver ink. *Nanotechnology*, 26(5):055202, 2015.
- [83] R. R. Lunt and V. Bulovic. Transparent, near-infrared organic photovoltaic solar cells for window and energy-scavenging applications. *Applied Physics Letters*, 98(11):113305, 2011.
- [84] W. Maass. Networks of spiking neurons: The third generation of neural network models. *Neural Networks*, 10(9):1659–1671, 1997.
- [85] T. M. Maffitt, J. K. DeBrosse, J. A. Gabric, E. T. Gow, M. C. Lamorey, J. S. Parenteau, D. R. Willmott, M. A. Wood, and W. J. Gallagher. Design considerations for MRAM. *IBM Journal of Research and Development*, 50(1):25–39, 2006.
- [86] P. Maisch, K. C. Tam, L. Lucera, H.-J. Egelhaaf, H. Scheiber, E. Maier, and C. J. Brabec. Inkjet printed silver nanowire percolation networks as electrodes for highly efficient semi-transparent organic solar cells. *Organic Electronics*, 38:139–143, 2016.
- [87] S. Majumdar, B. Chen, Q. H. Qin, H. S. Majumdar, and S. van Dijken. Electrode dependence of tunneling electroresistance and switching stability in organic ferroelectric P(VDF-TrFE)-based tunnel junctions. *Advanced Functional Materials*, 28(15):1703273, 2018.

- [88] T. Masquelier, R. Guyonneau, and S. J. Thorpe. Spike timing dependent plasticity finds the start of repeating patterns in continuous spike trains. *PLoS one*, 3(1):e1377, 2008.
- [89] S. Masuda, K. Kitamura, Y. Okumura, S. Miyatake, H. Tabata, and T. Kawai. Transparent thin film transistors using ZnO as an active channel layer and their electrical properties. *Journal of Applied Physics*, 93(3):1624–1630, 2003.
- [90] Y. Matveyev, R. Kirtaev, A. Fetisova, S. Zakharchenko, D. Negrov, and A. Zenkevich. Crossbar nanoscale HfO<sub>2</sub>-based electronic synapses. *Nanoscale research letters*, 11(1):147, 2016.
- [91] J. D. McBrayer. Diffusion of metals in silicon dioxide. *Journal of The Electrochemical Society*, 133(6):1242, 1986.
- [92] W. S. McCulloch and W. Pitts. A logical calculus of the ideas immanent in nervous activity. *The Bulletin of Mathematical Biophysics*, 5(4):115–133, 1943.
- [93] R. McKennell. Cone-plate viscometer. *Analytical Chemistry*, 28(11):1710–1714, 1956.
- [94] M. Meier, S. Gilles, R. Rosezin, C. Schindler, S. Trelenkamp, A. Rüdiger, D. Mayer, C. Kügeler, and R. Waser. Resistively switching Pt/spin-on glass/Ag nanocells for non-volatile memories fabricated with UV nanoimprint lithography. *Microelectronic Engineering*, 86(4-6):1060–1062, 2009.
- [95] S. Merilampi, T. Laine-Ma, and P. Ruuskanen. The characterization of electrically conductive silver ink patterns on flexible substrates. *Microelectronics Reliability*, 49(7):782–790, 2009.
- [96] B. Mittermeier, A. Bednar, M. Kaiser, A. Ruediger, and C. Schindler. Comparison of spin-on-glass and WO<sub>3</sub> as an insulating layer for printed resistive memory devices. *Materials Technology*, 20:1–6, 2019.
- [97] M. Morales-Masis, van der Molen, S J, W. T. Fu, M. B. Hesselberth, and J. M. van Ruitenbeek. Conductance switching in Ag<sub>2</sub>S devices fabricated by in situ sulfurization. *Nanotechnology*, 20(9):095710, 2009.
- [98] M. P. Murrell, M. E. Welland, S. J. O’Shea, T. M. H. Wong, J. R. Barnes, A. W. McKinnon, M. Heyns, and S. Verhaverbeke. Spatially resolved electrical measurements of SiO<sub>2</sub> gate oxides using atomic force microscopy. *Applied Physics Letters*, 62(7):786–788, 1993.
- [99] A. M. Nardes, M. Kemerink, R. A. J. Janssen, J. A. M. Bastiaansen, N. M. M. Kiggen, B. M. W. Langeveld, van Breemen, A. J. J. M., and M. M. de Kok. Microscopic understanding of the anisotropic conductivity of PEDOT:PSS thin films. *Advanced Materials*, 19(9):1196–1200, 2007.

- [100] S. Nau, C. Wolf, K. Popovic, A. Blümel, F. Santoni, A. Gagliardi, A. Di Carlo, S. Sax, and E. J. W. List-Kratochvil. Inkjet-printed resistive switching memory based on organic dielectric materials: From single elements to array technology. *Advanced Electronic Materials*, 1(1-2):1400003, 2015.
- [101] J. Niittynen, E. Sowade, H. Kang, R. R. Baumann, and M. Mäntysalo. Comparison of laser and intense pulsed light sintering (ipl) for inkjet-printed copper nanoparticle layers. *Scientific reports*, 5:8832, 2015.
- [102] T. Ohno, T. Hasegawa, T. Tsuruoka, K. Terabe, J. K. Gimzewski, and M. Aono. Short-term plasticity and long-term potentiation mimicked in single inorganic synapses. *Nature materials*, 10(8):591–595, 2011.
- [103] D. E. O’Leary. Gartner’s hype cycle and information system research issues. *International Journal of Accounting Information Systems*, 9(4):240–252, 2008.
- [104] C. M. Osburn and D. W. Ormond. Dielectric breakdown in silicon dioxide films on silicon. *Journal of The Electrochemical Society*, 119(5):597, 1972.
- [105] F. Pan, S. Gao, C. Chen, C. Song, and F. Zeng. Recent progress in resistive random access memories: Materials, switching mechanisms, and performance. *Materials Science and Engineering: R: Reports*, 83:1–59, 2014.
- [106] S.-I. Park, J.-H. Ahn, X. Feng, S. Wang, Y. Huang, and J. A. Rogers. Theoretical and experimental studies of bending of inorganic electronic materials on plastic substrates. *Advanced Functional Materials*, 18(18):2673–2684, 2008.
- [107] J. Perelaer, B.-J. de Gans, and U. S. Schubert. Ink-jet printing and microwave sintering of conductive silver tracks. *Advanced Materials*, 18(16):2101–2104, 2006.
- [108] P. Peumans and S. R. Forrest. Very-high-efficiency double-heterostructure copper phthalocyanine/C<sub>60</sub> photovoltaic cells. *Applied Physics Letters*, 79(1):126–128, 2001.
- [109] M. Prezioso, F. Merrikh Bayat, B. Hoskins, K. Likharev, and D. Strukov. Self-adaptive spike-time-dependent plasticity of metal-oxide memristors. *Scientific reports*, 6:21331, 2016.
- [110] T. Prodromakis. Practical applications of memristive technologies - beyond memory, 2018/07/04 Memrisys Conference invited talk, Beijing, China.
- [111] K. Rahman, M. Mustafa, N. M. Muhammad, and K. H. Choi. Electrohydrodynamic printed TiO<sub>2</sub> flexible memory device – fabrication and characterisation. *Electronics Letters*, 48(20):1261, 2012.
- [112] N. Reis, C. Ainsley, and B. Derby. Ink-jet delivery of particle suspensions by piezoelectric droplet ejectors. *Journal of Applied Physics*, 97(9):094903, 2005.

- [113] J. A. Rogers, T. Someya, and Y. Huang. Materials and mechanics for stretchable electronics. *Science (New York, N.Y.)*, 327(5973):1603–1607, 2010.
- [114] U. Russo, D. Ielmini, A. Redaelli, and A. L. Lacaita. Modeling of programming and read performance in phase-change memories—part ii: Program disturb and mixed-scaling approach. *IEEE Transactions on Electron Devices*, 55(2):515–522, 2008.
- [115] N. Sani, M. Robertsson, P. Cooper, X. Wang, M. Svensson, P. Andersson Ersman, P. Norberg, M. Nilsson, D. Nilsson, X. Liu, H. Hesselbom, L. Akesso, M. Fahlman, X. Crispin, I. Engquist, M. Berggren, and G. Gustafsson. All-printed diode operating at 1.6 GHz. *Proceedings of the National Academy of Sciences of the United States of America*, 111(33):11943–11948, 2014.
- [116] C. Schindler, S. C. P. Thermadam, R. Waser, and M. N. Kozicki. Bipolar and unipolar resistive switching in Cu-doped SiO<sub>2</sub>. *IEEE Transactions on Electron Devices*, 54(10):2762–2768, 2007.
- [117] C. Schindler, M. Weides, M. N. Kozicki, and R. Waser. Low current resistive switching in Cu–SiO<sub>2</sub> cells. *Applied Physics Letters*, 92(12):122910, 2008.
- [118] A. P. Shpak, A. M. Korduban, M. M. Medvedskij, and V. O. Kandyba. XPS studies of active elements surface of gas sensors based on WO<sub>3-x</sub> nanoparticles. *Journal of Electron Spectroscopy and Related Phenomena*, 156-158:172–175, 2007.
- [119] M. Singh, H. M. Haverinen, P. Dhagat, and G. E. Jabbour. Inkjet printing-process and its applications. *Advanced Materials*, 22(6):673–685, 2010.
- [120] P. J. Smith, D.-Y. Shin, J. E. Stringer, B. Derby, and N. Reis. Direct ink-jet printing and low temperature conversion of conductive silver patterns. *Journal of Materials Science*, 41(13):4153–4158, 2006.
- [121] Smithers Pira. The future of functional and industrial print to 2020. 2015, retrieved on 2019/01/12 from <http://www.oe-a.org/downloads>.
- [122] S. Song, K. D. Miller, and L. F. Abbott. Competitive hebbian learning through spike-timing-dependent synaptic plasticity. *Nature neuroscience*, 3(9):919–926, 2000.
- [123] S. Stathopoulos, A. Khiat, M. Trapatseli, S. Cortese, A. Serb, I. Valov, and T. Prodromakis. Multibit memory operation of metal-oxide bi-layer memristors. *Scientific reports*, 7(1):17532, 2017.
- [124] Y. Sun and Y. Xia. Large-scale synthesis of uniform silver nanowires through a soft, self-seeding, polyol process. *Advanced Materials*, 14(11):833, 2002.
- [125] E. Tekin, B.-J. de Gans, and U. S. Schubert. Ink-jet printing of polymers - from single dots to thin film libraries. *Journal of Materials Chemistry*, 14(17):2627, 2004.

- [126] E. Tekin, P. J. Smith, and U. S. Schubert. Inkjet printing as a deposition and patterning tool for polymers and inorganic particles. *Soft Matter*, 4(4):703, 2008.
- [127] S. P. Thermadam, S. K. Bhagat, T. L. Alford, Y. Sakaguchi, M. N. Kozicki, and M. Mitkova. Influence of Cu diffusion conditions on the switching of Cu–SiO<sub>2</sub>-based resistive memory devices. *Thin Solid Films*, 518(12):3293–3298, 2010.
- [128] I. Valov. Redox-based resistive switching memories (rerams): Electrochemical systems at the atomic scale. *ChemElectroChem*, 1(1):26–36, 2014.
- [129] I. Valov, E. Linn, S. Tappertzhofen, S. Schmelzer, J. van den Hurk, F. Lentz, and R. Waser. Nanobatteries in redox-based resistive switches require extension of memristor theory. *Nature Communications*, 4:1771, 2013.
- [130] I. Valov, R. Waser, J. R. Jameson, and M. N. Kozicki. Electrochemical metallization memories—fundamentals, applications, prospects. *Nanotechnology*, 22(28):289502, 2011.
- [131] D. B. van Dam and C. Le Clerc. Experimental study of the impact of an ink-jet printed droplet on a solid substrate. *Physics of Fluids*, 16(9):3403–3414, 2004.
- [132] G. Vescio, A. Crespo-Yepes, D. Alonso, S. Claramunt, M. Porti, R. Rodriguez, A. Cornet, A. Cirera, M. Nafria, and X. Aymerich. Inkjet printed HfO<sub>2</sub> -based ReRAMs: First demonstration and performance characterization. *IEEE Electron Device Letters*, 38(4):457–460, 2017.
- [133] V. Vijay, A. D. Rao, and K. S. Narayan. In situ studies of strain dependent transport properties of conducting polymers on elastomeric substrates. *Journal of Applied Physics*, 109(8):084525, 2011.
- [134] P. Vilmi, M. Nelo, J.-V. Voutilainen, J. Palosaari, J. Pörhönen, S. Tuukkanen, H. Jantunen, J. Juuti, and T. Fabritius. Fully printed memristors for a self-sustainable recorder of mechanical energy. *Flexible and Printed Electronics*, 1(2):025002, 2016.
- [135] M. Vosgueritchian, D. J. Lipomi, and Z. Bao. Highly conductive and transparent PE-DOT:PSS films with a fluorosurfactant for stretchable and flexible transparent electrodes. *Advanced Functional Materials*, 22(2):421–428, 2012.
- [136] Z. Wang, S. Joshi, S. E. Savel’ev, H. Jiang, R. Midya, P. Lin, M. Hu, N. Ge, J. P. Strachan, Z. Li, Q. Wu, M. Barnell, G.-L. Li, H. L. Xin, R. S. Williams, Q. Xia, and J. J. Yang. Memristors with diffusive dynamics as synaptic emulators for neuromorphic computing. *Nature materials*, 16(1):101–108, 2017.
- [137] R. Waser (Ed.). *Nanoelectronics and information technology: Advanced electronic materials and novel devices*. Wiley-VCH, Weinheim, 3., completely rev. and enl. ed. edition, 2012.

- [138] T. Wong, R. Preissl, P. Datta, M. Flickner, R. Singh, S. Esser, E. McQuinn, R. Appuswamy, W. Risk, H. Simon, and D. Modha. Ten to power 14. In *IBM Research Report RJ10502*, volume ALM1211-004.
- [139] J. Wu, J. Zang, A. R. Rathmell, X. Zhao, and B. J. Wiley. Reversible sliding in networks of nanowires. *Nano letters*, 13(6):2381–2386, 2013.
- [140] Y. C. Yang, F. Pan, Q. Liu, M. Liu, and F. Zeng. Fully room-temperature-fabricated nonvolatile resistive memory for ultrafast and high-density memory application. *Nano letters*, 9(4):1636–1643, 2009.
- [141] M. A. Zidan, J. P. Strachan, and W. D. Lu. The future of electronics based on memristive systems. *Nature Electronics*, 1(1):22–29, 2018.
- [142] S. Zou and C. Michael. Flexible non-volatile Cu/Cu<sub>x</sub>O/Ag ReRAM memory devices fabricated using ink-jet printing technology. In *2014 IEEE 64th Electronic Components and Technology Conference (ECTC)*, pages 441–446.